The Compact Muon Solenoid Experiment
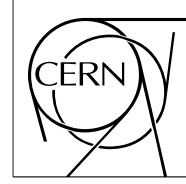
Analysis Note

The content of this note is intended for CMS internal use and distribution only

Search for a SM Higgs or BSM Boson
$H \to ZZ^{(*)} \to (q\bar{q})(\ell^-\ell^+)$

S. Bolognesi$^{\diamond\triangle}$, A. Bonato$^{\triangle\diamond}$, D. Del Re$^{\heartsuit}$, A.V. Gritsan$^{\diamond}$, M. Mannelli$^{\triangle}$,
M. Mozer$^{\triangle}$, F. Pandolfi$^{\heartsuit}$, N.V. Tran$^{\square\diamond}$, A. Whitbeck$^{\diamond}$

$^{\diamond}$ Johns Hopkins University, Baltimore, MD, USA
$^{\triangle}$ CERN, Geneva, Switzerland
$^{\heartsuit}$ 'Sapienza' Università di Roma e Sezione dell'INFN, Rome, Italy
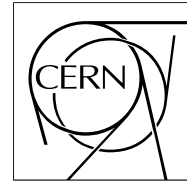$^{\square}$ FNAL, Batavia, IL, USA

Abstract

A search for the standard model Higgs boson decaying to two Z bosons with subsequent decay to a final state with two leptons and two quark-jets, $H \to ZZ^{(*)} \to (q\bar{q})(\ell^-\ell^+)$, is presented. Data corresponding to an integrated luminosity of about 4.6 fb^{-1} of LHC proton-proton collisions were collected and analyzed by the CMS experiment. The selection to discriminate between signal and background events is based on kinematic and topological quantities, which include the angular spin correlations of the decay products. The events are classified according to probability of the jets to originate from quarks of light or heavy flavor or from gluons. No evidence for a Higgs boson is found and upper limits on the Higgs boson production cross section are set in the range of masses between 130 and 164 GeV, and between 200 and 600 GeV. Prospects for a Beyond the Standard Model boson exclusion are discussed.

The Compact Muon Solenoid Experiment

CMS Note

Mailing address: CMS CERN, CH-1211 GENEVA 23, Switzerland

December 9, 2011

Search for a SM Higgs or BSM Boson
$H \rightarrow ZZ^{(*)} \rightarrow (q\bar{q})(\ell^-\ell^+)$

S. Bolognesi$^{\diamond\triangle}$, A. Bonato$^{\triangle\diamond}$, D. Del Re$^{\heartsuit}$, A.V. Gritsan$^{\diamond}$, M. Mannelli$^{\triangle}$,
M. Mozer$^{\triangle}$, F. Pandolfi$^{\heartsuit}$, N.V. Tran$^{\square\diamond}$, A. Whitbeck$^{\diamond}$

$^{\diamond}$ *Johns Hopkins University, Baltimore, MD, USA*

$^{\triangle}$ *CERN, Geneva, Switzerland*

$^{\heartsuit}$ *'Sapienza' Università di Roma e Sezione dell'INFN, Rome, Italy*

$^{\square}$ *FNAL, Batavia, IL, USA*

Abstract

A search for the standard model Higgs boson decaying to two Z bosons with subsequent decay to a final state with two leptons and two quark-jets, $H \rightarrow ZZ^{(*)} \rightarrow (q\bar{q})(\ell^-\ell^+)$, is presented. Data corresponding to an integrated luminosity of about 4.6 fb^{-1} of LHC proton-proton collisions were collected and analyzed by the CMS experiment. The selection to discriminate between signal and background events is based on kinematic and topological quantities, which include the angular spin correlations of the decay products. The events are classified according to probability of the jets to originate from quarks of light or heavy flavor or from gluons. No evidence for a Higgs boson is found and upper limits on the Higgs boson production cross section are set in the range of masses between 130 and 164 GeV, and between 200 and 600 GeV. Prospects for a Beyond the Standard Model boson exclusion are discussed.

Log of Changes in version 7

Updated SM4 results.

Updated exclusion plots.

Log of Changes in version 6

Updated systematics.

Updated primary results.

Log of Changes in version 5

Updated background parameterization description in Section 7.

Include observed limits in Section 9 (high mass range).

Include observed limits and alternative background parameterization in Section 10 (low mass range).

Log of Changes in version 4

Update exclusion plots and m_{ZZ} plots to 4.6/fb

Add description of 2D parameterization in the low mass range (m_{ZZ}, $m_{\ell\ell}$) in Sections 10.6 and 10.7

Minor updates about the fit mass range etc...

Contents

4

1 Introduction

The search for the SM Higgs in a wide range of masses from 120 GeV to 600 GeV is of high priority for LHC experiments. Even though indirect constraints on the SM Higgs mass limit it to the lower values [1], these constraints rely on theoretical assumptions. Therefore the experimental goal is to cover all accessible energies. The decay of a Higgs boson to two light fermions is highly suppressed. The dominant discovery channels on LHC are two gauge bosons: $\gamma\gamma$ and ZZ^* below the W^+W^- threshold, W^+W^- between the W^+W^- and ZZ thresholds, and ZZ above its threshold. Other final states may be investigated as well.

While the "golden" Higgs decay chain chain final states (such as all-lepton final states) have been investigated in detail, the semi-leptonic final states have not received much attention until recently. In this note we present an optimized search for a Standard Model Higgs boson decay to two Z bosons with a subsequent decay to two leptons and two quark jets, $H \to ZZ \to 2\ell2j$. The branching fraction of this decay channel is about 20 times higher than of $H \to ZZ \to (\ell^+\ell^-)(\ell^+\ell^-)$, which includes a factor of 2 due to two different Z channels. The presence of jets in the final state requires considerably more effort in selection and the final reconstruction efficiency is about half of the purely lepton final state at higher masses, resolution in parameters is worse, and background is considerably higher and is dominated by the Z+jets final states. Nonetheless, the much higher branching fraction of the semileptonic final state wins in sensitivity at higher masses, where the Z+jets background is not very high, but this channel is overwhelmed by background at lower masses.

Besides searches for a SM Higgs, the $X \to ZZ \to 2\ell2q$ analysis is interesting in the search for New Physics, such as RS Graviton in the theory with extra spacial dimensions. In Fig. 1, the product of particle X production cross-section (at LHC energy of 7 TeV) and the branching fraction $X \to ZZ$ is shown for a SM Higgs, several scenarios of RS Graviton, and an effective Tevatron limit. The expected RS Graviton $G \to ZZ$ production rate depends on the value of c. The Tevatron limit set by CDF at approximately $m_G > 600$ GeV for $c = 0.1$.

Other previous studies of the $X \to ZZ \to 2\ell2q$ include recent results from CMS and ATLAS with 1.6 and 1.1 fb^{-1} of data, respectively, and the earlier CMS feasibility study in Ref. [2]. The preliminary version of this analysis was presented at the CMS Higgs Review first in December 2010 [3] and then in August 2011 targeting Lepton-Photon conference [4]. In this study we cover both light and heavy flavors of the quarks in the hadronic decay of a Z by separating signal into three flavor categories with 0, 1, and 2 b-tag jets, while details specific to a category of events with positive b-tags are presented in Ref. [5].

The main change with respect to the previous analysis [4] is inclusion of the $X \to ZZ^* \to (q\bar{q})(\ell^-\ell^+)$ analysis in search for the Higgs boson in the range of masses between 130 and 170 GeV. Therefore, a separate Section 10 is devoted to all details of analysis $X \to ZZ^*$, while all the prior sections describe $X \to ZZ$ analysis above the $2m_Z$ threshold.
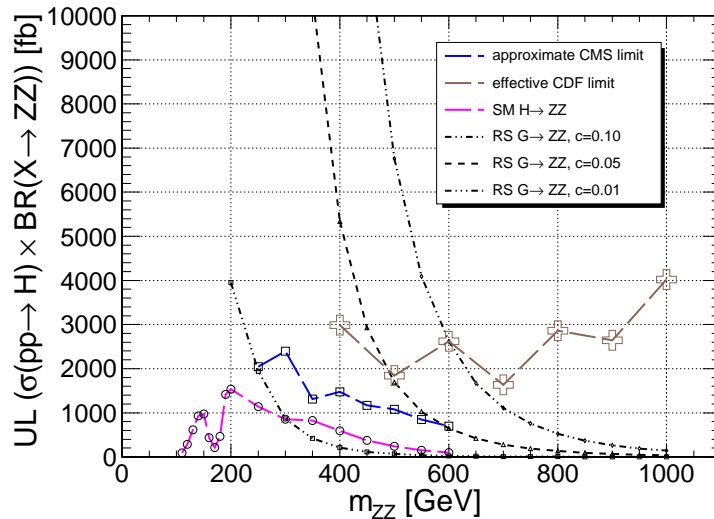

Figure 1: The product of particle X production cross-section (at LHC energy of 7 TeV) and the branching fraction $X \to ZZ$ for four scenarios: SM Higgs and RS graviton with $c = 0.01, 0.50, 0.10$. Effective limit extracted from CDF results is shown with crosses. The CMS limit with 1.6 fb^{-1} of data is shown with squares.

2 Monte Carlo Samples and Data Sets

2.1 Signal MC

A dedicated simulation program has been used to generate signal events [6] listed in Tables 1 and 2. The main purpose of the dedicated program is to generate spin correlations through the $2 \rightarrow 1 \rightarrow 2 \rightarrow 4$ process, such as production and decay of a Higgs or Graviton resonance. Pythia [9] is used for hadronization and further interface to the CMS software (CMSSW) framework. The latest samples correspond to Spring11 production with release CMSSW_3_11_3. We also use signal MC samples generated with POWHEG listed in Table 3 and find consistent kinematic distribution in cases with trivial spin correlations, such as spin-zero particle production above the ZZ mass threshold. However, POWHEG cannot be used to generate more complex cases, including spin-two graviton. Moreover, only the dominant gluon fusion production mechanism of a Higgs is considered. While weak boson fusion (WBF) mechanism has a small contribution, no angular correlations are passed through a spin-zero Higgs and no changes in analysis are expected, unless WBF-specific tagged jet selection is used. Therefore, we use the total Higgs production cross-section which combines all production mechanisms, but use only simulation of gluon fusion for signal parameterization.

Table 1: Signal Monte Carlo samples used in the study. Only muon and electron final states in the leptonic Z decay are considered, with the total branching fraction $\mathcal{B}_{2l2j}(ZZ \rightarrow 2l2j) \simeq 2 \times 0.067 \times 0.699 \simeq 0.0937$.

MC ID	name	mass	Γ (GeV)	$\sigma \times \mathcal{B}_{ZZ} \times \mathcal{B}_{2l2j}$ (fb)
9000426	SMHiggs0PToZZTo2L2Q_M-140_7TeV-jhu-pythia6	140	0.0081	85.4193
9000379	SMHiggsToZZTo2L2Q_M-200_7TeV-jhu-pythia6	200	1.43	141.266
9000384	SMHiggsToZZTo2L2Q_M-250_7TeV-jhu-pythia6	250	4.04	104.039
9000380	SMHiggsToZZTo2L2Q_M-300_7TeV-jhu-pythia6	300	8.43	78.3072
9000381	SMHiggsToZZTo2L2Q_M-350_7TeV-jhu-pythia6	350	15.2	71.833
9000382	SMHiggsToZZTo2L2Q_M-400_7TeV-jhu-pythia6	400	29.2	55.3619
9000383	SMHiggsToZZTo2L2Q_M-450_7TeV-jhu-pythia6	450	46.95	36.4765
9000398	SMHiggsToZZTo2L2Q_M-500_7TeV-jhu-pythia6	500	68	23.1429
9000412	SMHiggsToZZTo2L2Q_M-1000_7TeV-jhu-pythia6	1000	0	–

Table 2: Signal Monte Carlo samples for Graviton study.

MC ID	name	mass	Γ (GeV)	f_{gg}	$\sigma \times \mathcal{B}_{2l2j}$	$\mathcal{B}_{ZZ}$
9000388	Higgs2PM_ToZZTo2L2Q_M-250_7TeV-jhu-pythia6	250	4.04	1.00		
9000402	Higgs2PM_ToZZTo2L2Q_M-500_7TeV-jhu-pythia6	500	68	0.85		
9000416	Higgs2PM_ToZZTo2L2Q_M-1000_7TeV-jhu-pythia6	1000	0	0.75		

2.2 Background MC and cross-sections

The dominant background in the $H \rightarrow ZZ \rightarrow 2l2q$ analysis is the inclusive Z production with jets, that is Z+jets background. For the case of low Higgs mass ($M_H < 2 \times m_Z$) the Z is off-shell (Z^*+jets). The primary samples that we use has been produced with MadGraph with the latest conditions and is listed in Table 4.

We also checked Sherpa simulation of the process, listed in the same Table. Sherpa implements a different "matching" procedure with the Parton Shower with respect to Madgraph. Also the Parton Shower simulation itself, is different between the two generators. The comparison between Sherpa and Madgraph is therefore a reasonable estimate of the uncertainties related with the MC modeling of Z+jets.

Minor background arises from $t\bar{t}$, tW, ZZ, WZ, WW production, and the samples used are shown in Table 5.

In all cases the Summer11 production with releases CMSSW_4_2_X is used. The Z^*+jets Madgraph sample, where the Z is off-shell, is still in production and an old Spring11 sample with low statistics is used.

2.3 Data samples

We use 4.6 fb^{-1} of data collected in 2011 and prompt-reco'ed or re-reco'ed with CMSSW_4_2_X The data samples are listed in Table 6. We use only lumisections that has been declared good for analysis by the central certification

Table 3: Signal Monte Carlo samples generated with POWHEG. Muon, electron, and tau final states in the leptonic Z decay are considered.

MC ID	name	mass	Γ (GeV)	$\sigma \times \mathcal{B}_{ZZ} \times \mathcal{B}_{2l2j}$ (fb)
	GluGluToHToZZTo2L2Q_M-130_7TeV-powheg-pythia6	130		
9000115	GluGluToHToZZTo2L2Q_M-140_7TeV-powheg-pythia6	140	0.0081	128.129
	GluGluToHToZZTo2L2Q_M-150_7TeV-powheg-pythia6	150		
	GluGluToHToZZTo2L2Q_M-160_7TeV-powheg-pythia6	160		
	GluGluToHToZZTo2L2Q_M-180_7TeV-powheg-pythia6	180		
9000121	GluGluToHToZZTo2L2Q_M-200_7TeV-powheg-pythia6	200	1.43	211.9
	GluGluToHToZZTo2L2Q_M-210_7TeV-powheg-pythia6	210		
	GluGluToHToZZTo2L2Q_M-230_7TeV-powheg-pythia6	230		
	GluGluToHToZZTo2L2Q_M-250_7TeV-powheg-pythia6	250		
	GluGluToHToZZTo2L2Q_M-275_7TeV-powheg-pythia6	275		
9000122	GluGluToHToZZTo2L2Q_M-300_7TeV-powheg-pythia6	300	8.43	117.461
	GluGluToHToZZTo2L2Q_M-325_7TeV-powheg-pythia6	325		
	GluGluToHToZZTo2L2Q_M-350_7TeV-powheg-pythia6	350		
	GluGluToHToZZTo2L2Q_M-375_7TeV-powheg-pythia6	375		
9000123	GluGluToHToZZTo2L2Q_M-400_7TeV-powheg-pythia6	400	29.2	83.0428
	GluGluToHToZZTo2L2Q_M-425_7TeV-powheg-pythia6	425		
	GluGluToHToZZTo2L2Q_M-450_7TeV-powheg-pythia6	450		
	GluGluToHToZZTo2L2Q_M-475_7TeV-powheg-pythia6	475		
9000124	GluGluToHToZZTo2L2Q_M-500_7TeV-powheg-pythia6	500	68	34.7144
	GluGluToHToZZTo2L2Q_M-525_7TeV-powheg-pythia6	525		
	GluGluToHToZZTo2L2Q_M-550_7TeV-powheg-pythia6	550		
	GluGluToHToZZTo2L2Q_M-575_7TeV-powheg-pythia6	575		
9000125	GluGluToHToZZTo2L2Q_M-600_7TeV-powheg-pythia6	600	123	14.7312

Table 4: Summer11 Monte Carlo samples with Z+jets final state. A K-factor of 1.33 has been applied to Madgraph.

MC ID	name	σ LO(NLO) [pb]	lumi LO(NLO) [fb^{-1}]
4000003	DYJetsToLL_TuneZ2_M-50_7TeV-madgraph-tauola	2289(3048)	15.3(11.5)
	/DYToLL_M-50_1jEnh2_2jEnh35_3jEnh40_4jEnh50_7TeV-sherpa	2943	10.5
	/DYJetsToLL_M-10To50_7TeV-madgraph-tauola		

151 team.

Table 5: Monte Carlo samples with $t\bar{t}$, tW, ZZ, WZ, WW. The last column shows equivalent luminosity of the available MC sample.

MC ID	name	σ LO(NLO) [pb]	lumi LO(NLO) [fb^{-1}]
1000454	TT_TuneZ2_7TeV-pythia6-tauola	94(157.5)	11.7(6.98)
9000221	TTTo2L2Nu2B_7TeV-powheg-pythia6	15.86(16.7?)	63.05(59.87?)
	/T_TuneZ2_tW-channel-DR_7TeV-powheg-tauola		
	/Tbar_TuneZ2_tW-channel-DR_7TeV-powheg-tauola		
1000032	ZZtoAnything_TuneZ2_7TeV-pythia6-tauola	4.30(5.9)	491.5(358.2)
1000031	WZtoAnything_TuneZ2_7TeV-pythia6-tauola	10.4(18.3)	211.0(119.9)
1000030	WWtoAnything_TuneZ2_7TeV-pythia6-tauola	27.8(42.9)	73.7(47.8)

Table 6: Data samples used in analysis.

/SingleMu/Run2011A-May10ReReco-v1/AOD
/SingleMu/Run2011A-PromptSkim-v4/AOD
/SingleMu/Run2011A-05Aug2011-v1/AOD
/SingleMu/Run2011A-03Oct2011-v1/AOD
/SingleMu/Run2011B-PromptReco-v1/AOD
/DoubleMu/Run2011A-May10ReReco-v1/AOD
/DoubleMu/Run2011A-PromptSkim-v4/AOD
/DoubleMu/Run2011A-05Aug2011-v1/AOD
/DoubleMu/Run2011A-03Oct2011-v1/AOD
/DoubleMu/Run2011B-PromptReco-v1/AOD
/DoubleElectron/Run2011A-May10ReReco-v1/AOD
/DoubleElectron/Run2011A-PromptSkim-v4/AOD
/DoubleElectron/Run2011A-05Aug2011-v1/AOD
/DoubleElectron/Run2011A-03Oct2011-v1/AOD
/DoubleElectron/Run2011B-PromptReco-v1/AOD

3 Event Reconstruction and Selection

Two independent software packages are employed in the analysis of the channel $X \rightarrow ZZ \rightarrow 2l2j$: one makes use of the Physics Analysis Toolkit (PAT) [10], one runs directly on AOD objects. The analysis redundancy ensures an overall robustness, as one workflow may be employed to cross-check the other at any time. High level of agreement of better than 1% is achieved between the two complementary software packages.

Input objects to the analysis are GSF electrons [11], Global Muons [12], and Particle Flow jets [13, 14]. In order to avoid to double count the leptons inside the jets, a $\Delta R > 0.5$ cut is applied between the leptons chosen for the Z reconstruction and the jets.

3.1 Trigger and skim requirements

The results presented in this note are based on the SingleMu, DoubleMu and DoubleElectron datasets. Each of these datasets contain at least one un-prescaled trigger with looser requirements than our offline selections. The lowest threshold un-prescaled trigger is used and this trigger changes as instanteous luminosity rises. These triggers are HLT_IsoMu24 for the SingleMu dataset
HLT_DoubleMu_7
HLT_Mu13_Mu8
HLT_Mu17_Mu8 for the DoubleMu dataset
HLT_Ele17_CaloIdL_CaloIsolVL_Ele8_CaloIdL_CaloIsolV and
HLT_Ele17_CaloIdT_TrkIdVL_CaloIsoVL_TrkIsoVL_Ele8_CaloIdT_TrkIdVL_CaloIsoVL_TrkIsoVL for the DoubleElectron dataset. More details are available in the corresponding analysis note [33].

For the first data-taking period (Run2011A) the HWW skim is exploited. This skim includes the following requirements, all looser than our analysis selections:

- at least one muon with $p_T(\mu) > 10$ GeV, Global and Tracker Muon and relative isolation < 1

- at least one electron with $p_T(e) > 10$ GeV, $\Delta\eta$(supercluster-track) < 0.01, $\sigma_{i\eta i\eta} < 0.011$ in barrel, $\sigma_{i\eta i\eta} < 0.031$ in endcaps

- $m_{ll} > 5$ GeV

This skim is applied to both di-lepton and single-lepton Primary Datasets.

Since the level of precision of the trigger emulation in simulation is not well known, the trigger efficiency is computed from data (as reported in [5]) and the Monte Carlo samples are reweighted accordingly.

3.2 Lepton requirements and dilepton Z

The electron candidates were reconstructed with the GSF algorithm. They were required to satisfy the following conditions to ensure good reconstruction performances [16]:

- transverse impact parameter with respect to the primary vertex $D_0 < 2$ mm;

- combined relative isolation parameter $R = \frac{ECAL_{ISO} + HCAL_{ISO} + TRK_{ISO}}{p_T} < 0.15$;

- VBTF Electron ID selection: ≥ 1 electron must pass the WP80 SimpleCutasedEID selection and ≥ 1 electron passing the WP95 selection.

A fiducial cut is applied to stay inside the ECAL acceptance. Electrons are rejected if $1.4442 < |\eta| < 1.566$ and $|\eta| < 2.5$. There is a conversion rejection applied [16].

Global muons were required to satisfy the following identification criteria:

- normalized χ^2 of the global track < 10.0;

- number of hits of the Tracker track ≥ 11;

- number of pixel hits of the Tracker track ≥ 1;

9

- number of muon hits of the Global track ≥ 2;

- $d_0 < 0.02$ cm;

- $z_0 < 1$ cm;

- $R < 0.15$.

Muons are required to be in the pseudorapidity range $|\eta| < 2.4$.

The leptons are required to have transverse momentum $p_T > 20$ or 40 GeV, for the lower or higher momentum lepton. Some of the kinematic distributions for signal and background are shown in Section 4.1. The di-lepton invariant mass is shown in Fig. 2. In the analysis the invariant mass of the $Z \to l^+l^-$ boson is required to be 70 GeV $< m_{ll} < 110$ GeV.
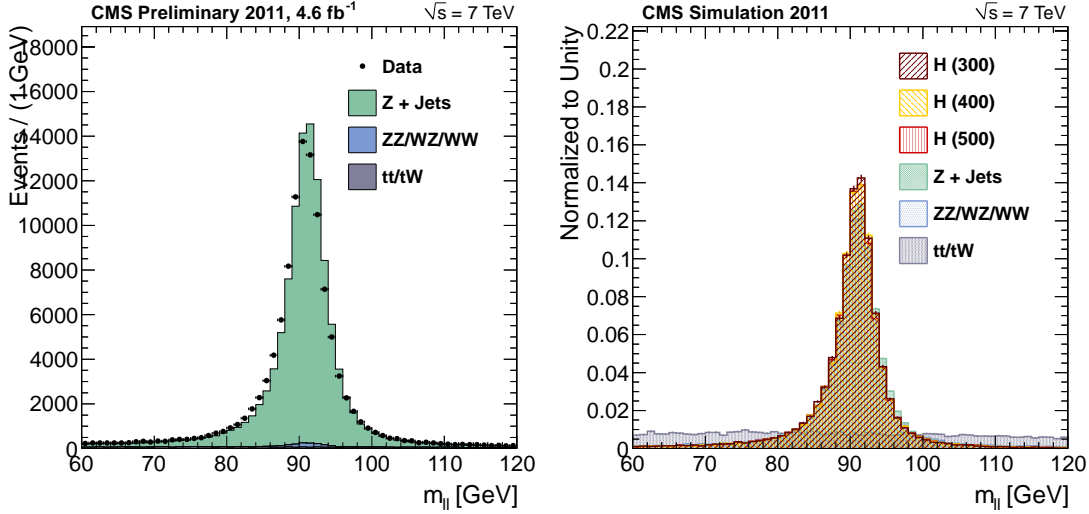

Figure 2: Dilepton invariant mass after loose selection requirements in the analysis. Left: comparison of 2010-2011 data and MC simulation with dominant contributions. Right: comparison of signal MC with three different generated mass values and dominant background contributions. Due to misconfiguration in generation of the Spring11 ALPGEN Z+jets samples, the relative composition of electron and muon final states is different in data and MC.

3.3 Jet requirements and dijet Z

The PF jets are reconstructed with the $\texttt{anti-k}_\texttt{T}$ algorithm [17] with radius parameter set to $R = 0.5$. Jet-energy corrections are applied to data and MC as explained in [18]. The jet corrections applied (excluding those for correcting for pile-up described in Section 3.4) were the the L2 and L3 corrections.

Jets are required to be inside the tracker acceptance ($|\eta| < 2.4$) thus allowing high reconstruction efficiency and precise energy measurements using PF techniques. A very loose jets identification is applied to remove fakes due to calorimeter noise:

- fraction of energy due to neutral hadrons < 0.99;

- fraction of energy due to neutral EM deposits < 0.99;

- number of constituents > 1;

- number of charged hadrons candidates > 0;

- fraction of energy due to charged hadrons candidates > 0;

- fraction of energy due to charged EM deposits < 0.99.

10

A preselection cut $p_T > 30$ GeV is applied to all jets since in signal jets are expected to come from the decay of a highly energetic Z boson. In the analysis a cut $75 < m_{JJ} < 105$ GeV (corresponding to $\sim 2\sigma$) is applied in order to reduce the dominant Z+jets background. The invariant mass of the 2 leading jets is shown in Fig. 3, the Z mass resolution is about 7 GeV.
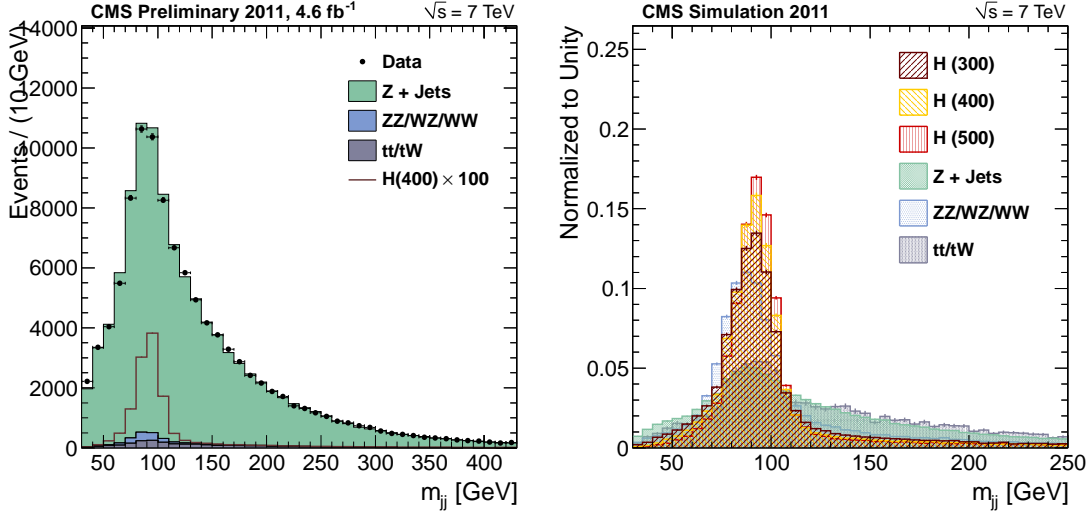

Figure 3: Dijet invariant mass . Left: comparison of 2010-2011 data and MC simulation with dominant contributions. Right: comparison of signal MC with three different generated mass values and dominant background contributions.

3.4 Pile-up correction and removal

The presence of additional interactions with respect to the primary one, known as Pile-up (PU), is expected to affect this analysis in the following ways:

- additional energy from PU get added to the jets from the main interaction

- additional low p_T jets fully composed of PU energy get added to the event

- tracks and calorimetric towers from PU energy deposits get added to the jets from the main interaction thus biasing their angles

The amount of PU interaction per event in data and MC is shown in Fig. 4. In the following this distribution in MC has been re-weighted to match the data. In Fig. 5 we show consistency in the number of reconstructed vertexes between data and MC after MC samples have been re-weighted.

Various algorithms are available to correct for PU effects. The so-called Fastjet and L1-offset corrections remove the additional energy released in the event which is expected to come from PU interactions. The charged particles coming from PU can also be removed before the jet clustering requiring that all the tracks come from the primary vertex. In this case also the PU effect on jet angles is partially corrected. Alternatively, only jets with a sizable amount of tracks coming from primary vertex can be considered.

To study these PU effects, signal events from a MC sample with 400 GeV Higgs mass which pass the preselection cuts listed in Section 3 are considered. The Fastjet algorithm has been applied to correct the PU energy in each jet. In Fig. 6 the transverse momentum resolution and the angular resolution is shown for jets matched ($\Delta R < 0.5$) with particle-level jets (which do not contain PU). As expected, PU affect the angular direction of the jets as well as the transverse momentum but in the second case the Fastjet algorithm corrects for most of the effect (residual effects are further corrected by the kinematic fit described in Section 3.5). In Fig. 7 the number of not-matched jets and their transverse momentum distribution is shown. Additional jets coming from PU are only partially corrected by Fastjet but this effect is only of the order of 1%. In Fig. 8 the transverse momentum of the two leading jets and the dijet invariant mass of the candidate nearest to the nominal Z mass are shown with and without PU and PU

corrections. Clearly the jet from signal are energetic enough to be not sizably affected by the PU but the invariant mass is affected because of the PU bias on the jet direction (as already shown in Fig. 6).

In the rest of the analysis the PU effect is corrected using the Fastjet algorithm. The final systematics due to PU on the signal acceptance is discussed in Section 8.
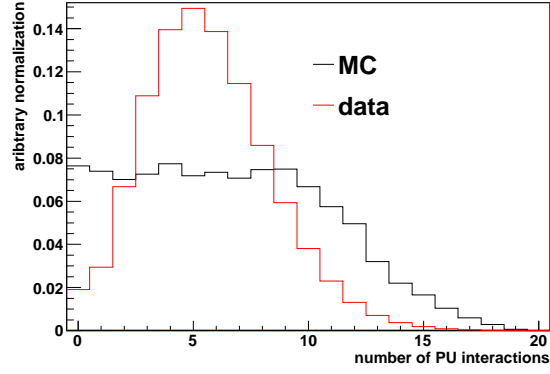

Figure 4: Number of PU interactions in data and MC. In the following the MC sample has been reweighted to match the data.
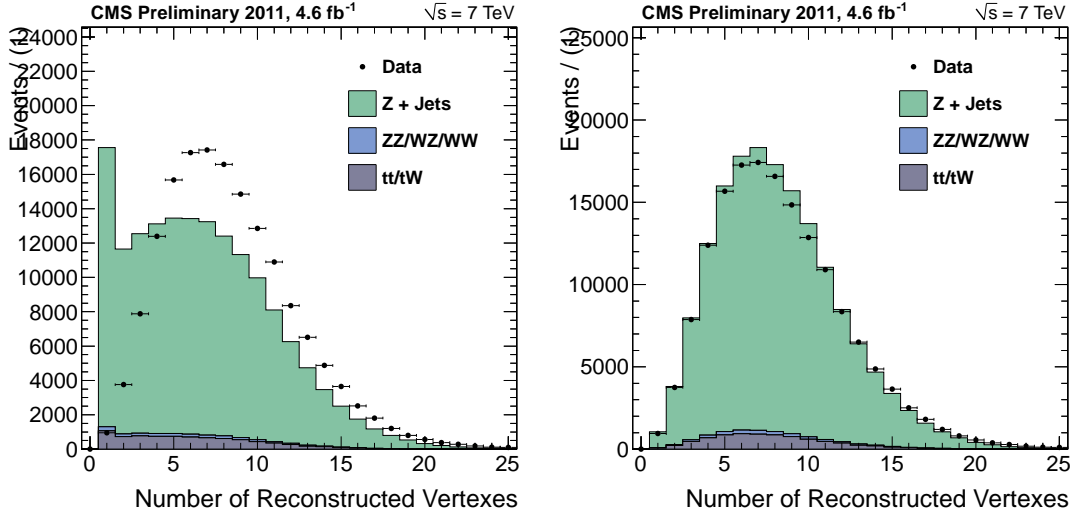

Figure 5: Number of reconstructed vertexes before (left) and after (right) the MC sample has been re-weighted. Pileup correction has been applied. Points with error bars show data after loose pre-selection, histograms show contribution of dominant background channels.
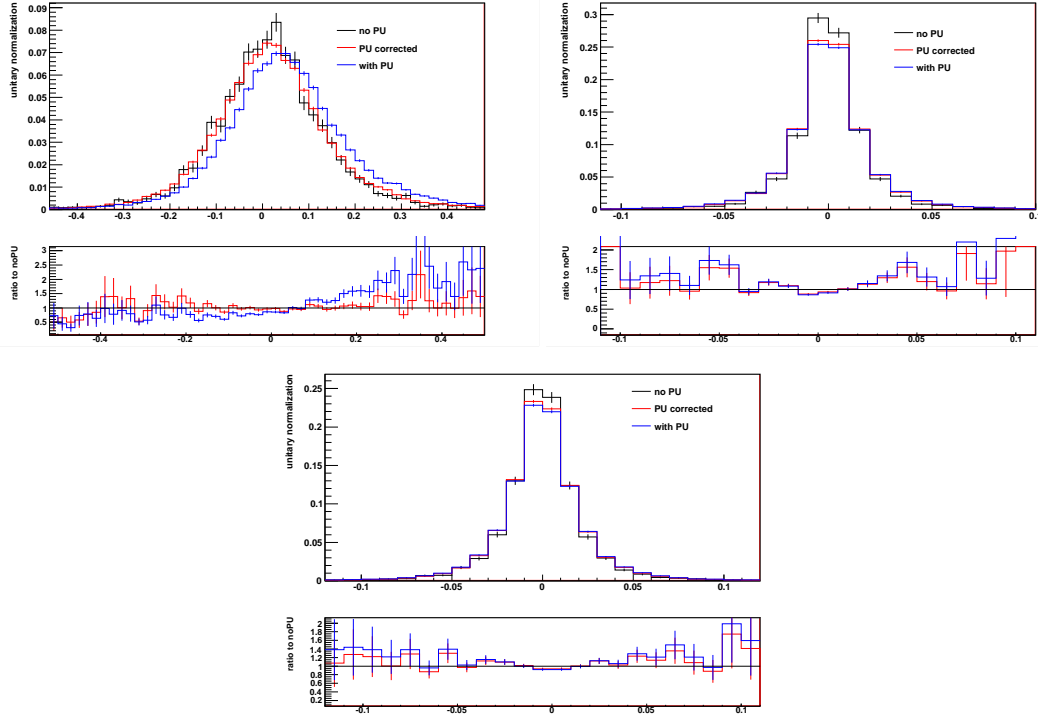
Figure 6: Resolution on transverse momentum (left), pseudorapidity (right) and azimuthal angle (bottom) in signal with Higgs mass 400 GeV with different PU conditions. Reconstructed jets are matched with particle-level jets ($\Delta R < 0.5$).
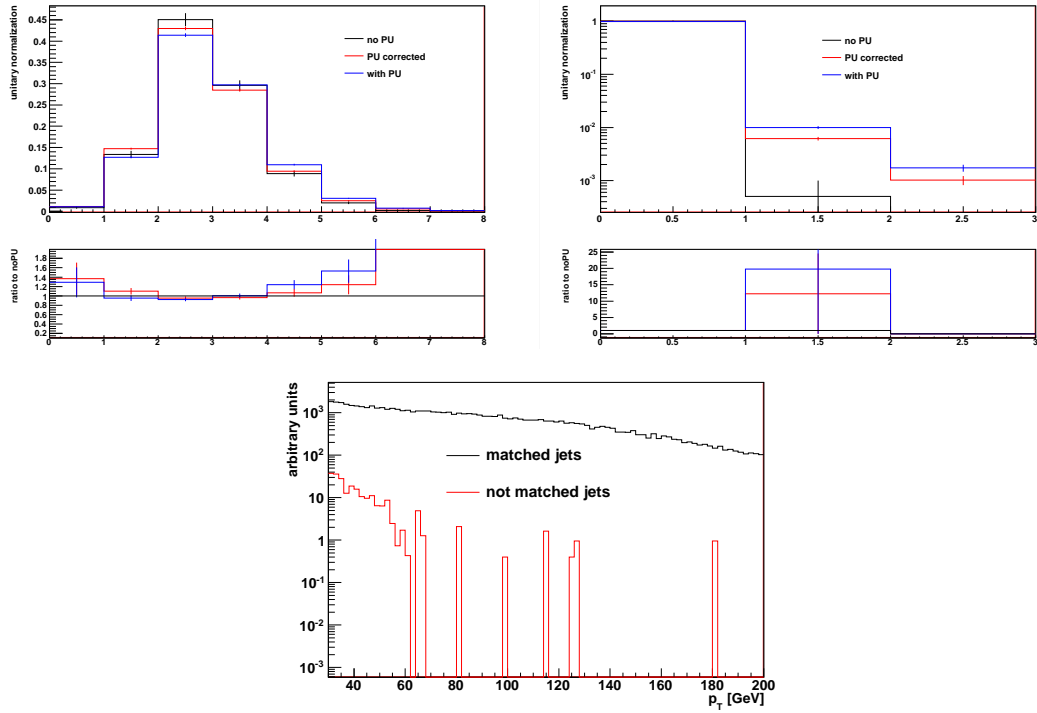
Figure 7: Number of jets in signal with Higgs mass 400 GeV for different PU conditions: all jets (left) and jets not matched with particle-level jets ($\Delta R > 0.5$) (right). Transverse momentum of matched and not matched jets in the sample with PU corrections (bottom)

Figure 8: Transverse momentum distribution of the leading jets (left) and of the second jet (right) and invariant mass of the dijet candidate nearest to the nominal Z mass (bottom) in signal with Higgs mass of 400 GeV with different PU conditions.
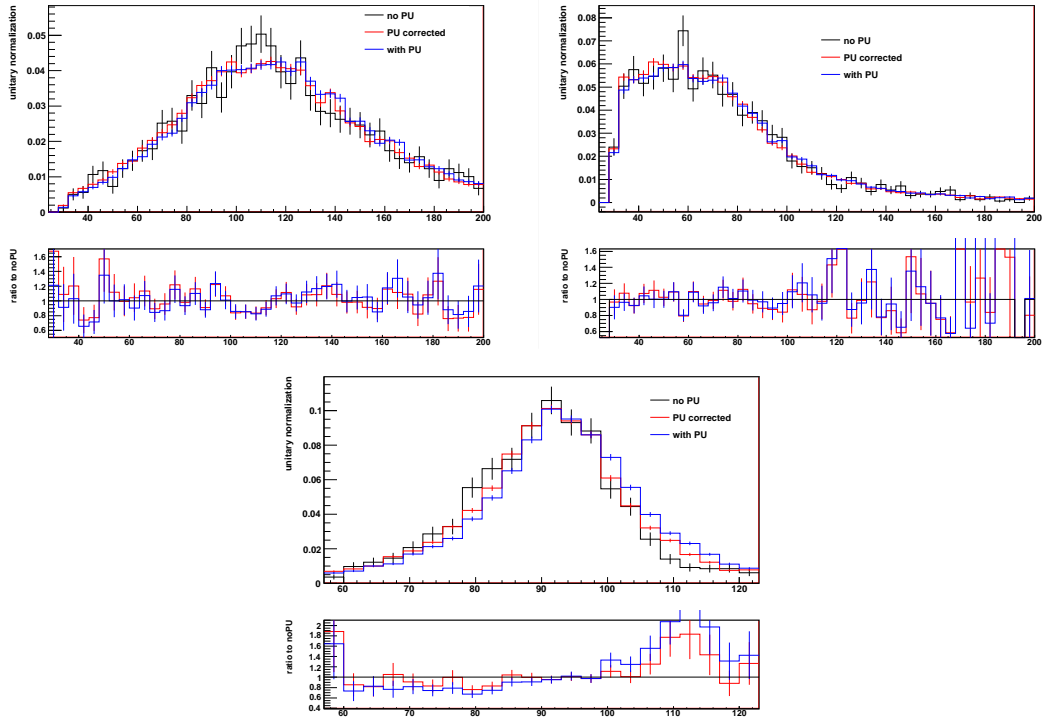
3.5 Kinematic fit of the decay chain

Finite resolution of the jet energy is the dominant source of uncertainty in both di-jet invariant mass m_{jj} and di-boson invariant mass m_{ZZ} for Higgs candidates. Therefore, the two variables become highly correlated, as can be seen in Fig. 9 (left). One could take this into account by introducing a correlated 2D selection algorithm which includes this correlation into account and maximizes the signal-over-background separation. However, it is more attractive to correct the jet energies taking into account a constraint that the di-jet invariant mass should correspond to a Z. This is effectively exploiting an additional information in signal events, and is therefore expected to improve the resolution on the Higgs invariant mass; as for background, the assumption introduces a constraint which is not correlated to the underlying physical process, and therefore has the effect of shuffling randomly the events in the final ZZ invariant mass spectrum.

Constraining the jet to be compatible with a Z boson decay may be done in different ways. The most simple one is to rescale the di-jet quadrimomentum as a whole, by modifying its energy so that its mass is equal the Z boson mass [19]. This approach already improves significantly the resolution on the ZZ invariant mass in signal, as can be seen in Fig. 10 for two different Higgs masses: the blue curve is obtained without applying any correction to the di-jet system, while the red curve is the resulting spectrum after scaling the di-jet quadrimomentum by constraining it to the Z boson mass.

While the described approach is simple and effective, it is suboptimal because it treats both jets 'democratically', i.e. without taking into account the prior knowledge we have on jet resolutions. We know for instance that as the jet energy increases the resolution on the measurement of its transverse momentum is expected to improve, driven by the calorimeter resolutions. Furthermore, different CMS subdetectors are expected to have different resolutions in jet reconstruction.

In order to optimally scale the di-jet quadrimomentum to the Z boson mass, we use a kinematic fit to the two jets. The fit is provided with parametrizations of jet transverse momentum and position resolutions as functions of transverse momentum and pseudorapidity, and therefore constrains the mass of the di-jet system to the value of the Z boson mass by modifying the jet quadrimomenta in accordance to their expected resolutions. This brings a further improvement in the resolution on the signal invariant mass, as is shown by the black curves in Fig. 10.

The kinematic fit to the di-jet system also removes the correlation between the di-jet and di-boson invariant mass in signal, as can be seen in Fig. 9 (right). This allows a straightforward definition of signal and sideband regions, through simple rectangular cuts.

As a final remark, while the constrain in the analysis is done by imposing the exact value of the Z boson mass, we have investigated the possibility of introducing a width in the mass constraint. This has been done in the fit by substituting the Dirac δ-function with a gaussian distribution, centered on the nominal Z boson mass. We have studied gaussian widths of 2 and 5 GeV, but no sensitive difference in signal efficiency has been observed.
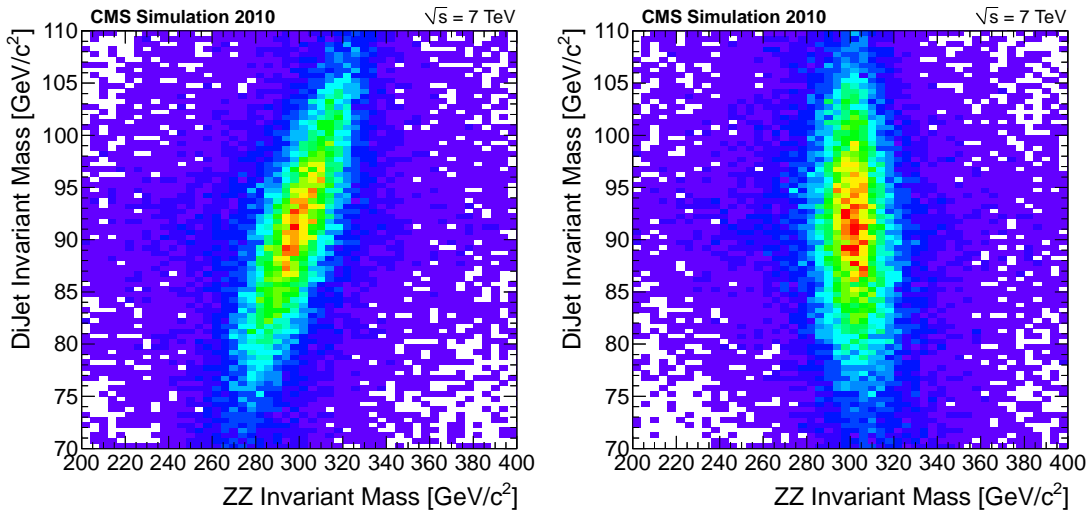

Figure 9: Di-jet invariant mass vs. di-boson invariant mass for Higgs candidates (signal MC) after loose selection requirements. Left: before kinematic fit; right: after kinematic fit.
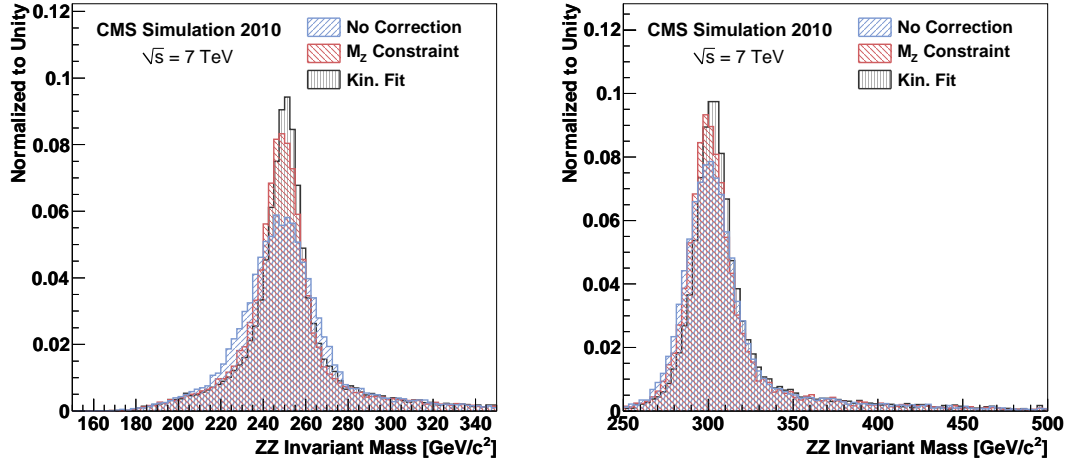
Figure 10: Comparison of signal MC with three different methods, raw invariant mass of two leptons and two jets, invariant mass with a constraint that the di-jet invariant mass is mean expected Z mass value [19], and finally with a kinematic fit and mass constraint. Left: $m_H = 250\,\text{GeV}$; right: $m_H = 300\,\text{GeV}$.

3.6 Higgs candidate and multiple event candidates in an event

From all the possible combinations of $Z \to 2l$ and $Z \to 2q$, resonance candidates are constructed. There is certain fraction of events when more than one candidate is present in an event after all the final selection requirements. The typical multiplicity of candidates per event is 1.2 and is predominantly due to more than one combination of jets satisfying selection requirements. The number of jets with p_T above the 30 GeV/c threshold in the pre-selected events is shown in Fig. 11. Multiple combinations happened in both signal and background. In analysis we do not necessarily need to pick a certain candidate. In the counting approach, we count the number of unique events after final selection, regardless of the number of combinations per each event. In the fit analysis, it is also possible to assign weight to each event. However, for simplicity of analysis we pick one unique candidate in each event passing all selection requirements. When the data are split in several b-tag categories (as discussed below), priority is given to candidates with the highest number of tagged jets. Among those candidates with the same number of tagged jets we pick the best candidate with the di-jet and the di-lepton invariant masses closest to the mean Z mass value [19].

The primary discrimination power of signal and background comes from the di-boson invariant mass. However, further sophisticated selection requirements are needed to discriminate signal from background, as shown in Fig. 11.

In order to simplify the combination of the analyses for Higgs search in different final states, is useful to have mutually exclusive phase space for the various channels. We checked that the number of events expected from $H \to ZZ \to 4l$ and $2l2\nu$ inside the acceptance of the present 2l2j analysis is negligible. Results for the muon channel are reported in Table 7. In order to have the full yields, we can assume similar acceptance for the electron channel and multiply by 2 the yields reported in Table 7. These numbers should be compared with the 2l2j expected yields listed in Table 13. None of the $2l2\nu$ events selected by this analysis pass the selection of the $2l2\nu$ analysis [21], while only about 20% of the 4l events selected by this analysis pass the selection of the 4l analysis [20].

The full 2l2q analysis selection is applied in this study, excepted the m_{ZZ} cut. In Fig. 12 the m_{ZZ} spectrum reconstructed by the 4l analysis and by the 2l2q analysis in a signal sample of $H \to ZZ \to 4l$ with $m_H = 300\,\text{GeV}$ are shown for those events which pass both the analysis selections. As can be seen, similar masses are reconstructed by the two analyses since the same 4 objects are used to build them, but in one case they are interpreted as leptons and in the other case as jets. In particular in the region of m_{ZZ} relevant for the 2l2q analysis (-6%,+10%) there is a clear linear correlation between the two reconstructed masses, the 4l mass being systematically lower. This is expected since in the 2l2q analysis the two additional leptons coming from the second Z are merged with other soft particles to make jets, finally jet energy corrections are applied to them which probably are overestimated since the transverse momentum of those jets is actually dominated by the well measured high pt lepton.
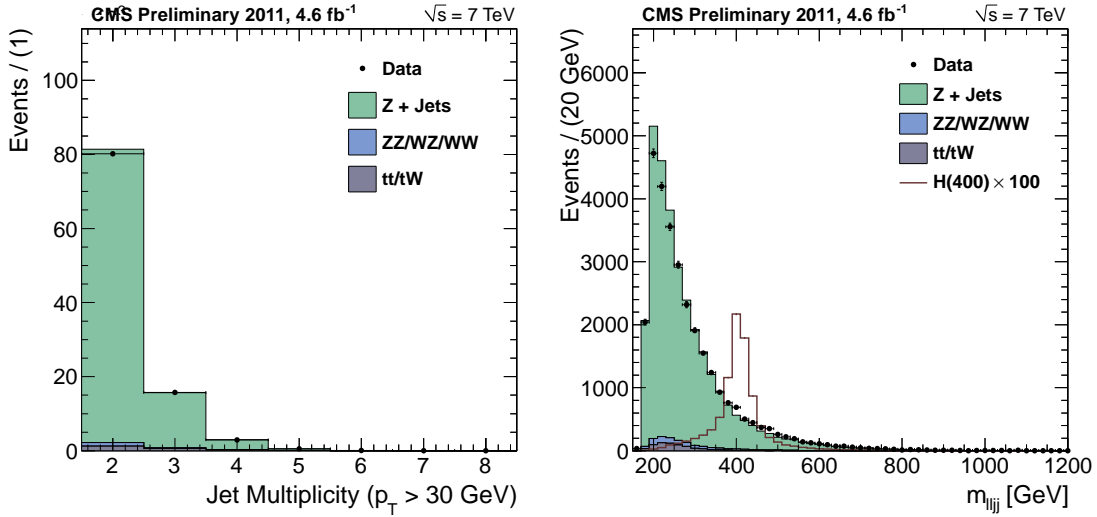
16

Figure 11: Left: number of jets pre-selected. Right: Di-boson invariant mass after loose selection requirements in the analysis. Comparison of 2010-2011 data and MC simulation with dominant contributions is shown.

Table 7: Cross-section, acceptance and yields for $H \to ZZ \to 4l$ and $2l2\nu$ channels inside the phase space of the present $2\mu 2j$ analysis (the full $M(ZZ)$ spectrum is considered).

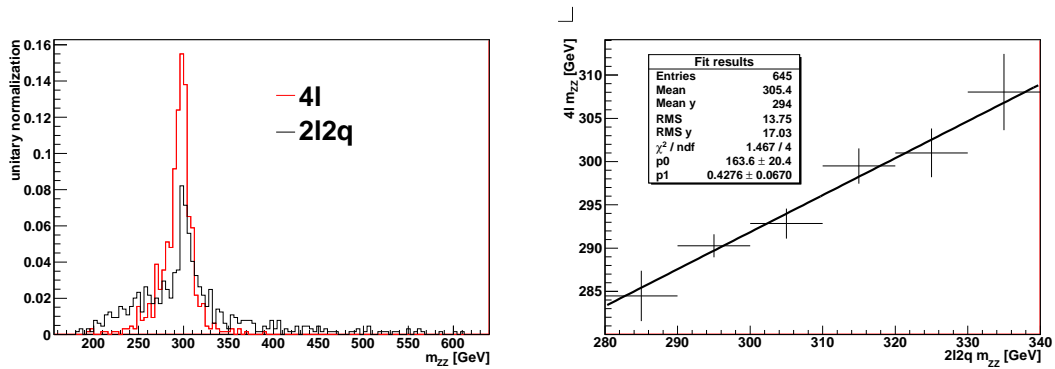| channel (Higgs mass)	$\sigma \times BR$	acceptance	yields in $1fb-1$
4l (200 GeV)	0.013 pb	0.0112 ± 0.0003	0.15
4l (300 GeV)	0.0075 pb	0.0275 ± 0.0005	0.21
4l (400 GeV)	0.0055 pb	0.0343 ± 0.0005	0.19
4l (500 GeV)	0.0022 pb	0.0360 ± 0.0006	0.08
$2l2\nu$ (200 GeV)	0.018 pb	0.0016 ± 0.0001	0.03
$2l2\nu$ (300 GeV)	0.0010 pb	0.0028 ± 0.0002	0.07
$2l2\nu$ (400 GeV)	0.0074 pb	0.0041 ± 0.0002	0.03
$2l2\nu$ (500 GeV)	0.0030 pb	0.0045 ± 0.0002	0.01

Figure 12: Left: Distribution of Higgs mass reconstructed by the 4l analysis and the 2l2q analysis in a sample of $H \to ZZ \to 4l$ MC with 300 GeV generated Higgs mass. Right: Correlation between the two reconstructed masses.

4 Kinematic Distributions and Angular Discriminant

There are several features in the signal $H \to ZZ \to 2l2j$ decay kinematics which discriminate it against background. We can exploit these kinematic differences to optimize selection and maximize signal significance or exclusion power. In the nominal approach we fully explore kinematics in the decay with five angles which characterize the decay and discuss this approach in Section 4.2. These five angles are only weakly correlated with the three invariant masses, shown in Figs. 2, 3, and 11.

4.1 Kinematic distributions and data-MC validation

Before moving to iscussion of the angular approach, let us discuss more "traditional" variables, such as transverse momentum and spacial separation between objects. Such variables are shown for several signal hypotheses and several background types in Fig. 13 for p_T of the Z, Fig. 14 for lepton p_T, Fig. 15 for jet p_T, and Fig. 16 for separation ΔR between the Z boson daughters. Obviously, all variables are highly correlated, for example Z and its daughter p_T values are highly correlated, and they are correlated with all the invariant masses. It is also evident that the lower the mass of the Higgs, the less kinematic separation exists between signal and background.
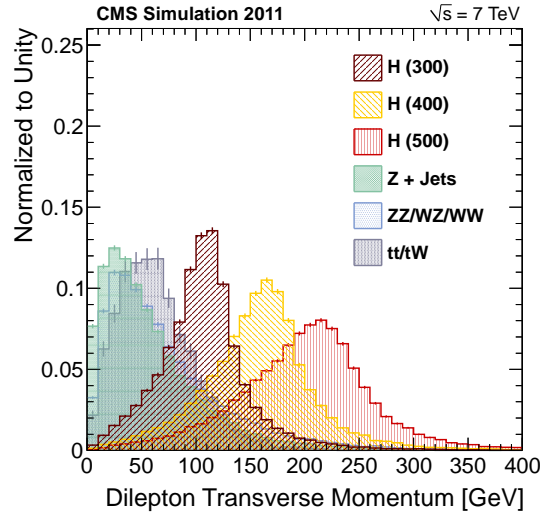
Figure 13: Leptonic $Z \to l^{+}l^{-}$ transverse momentum after loose selection requirements in the analysis.
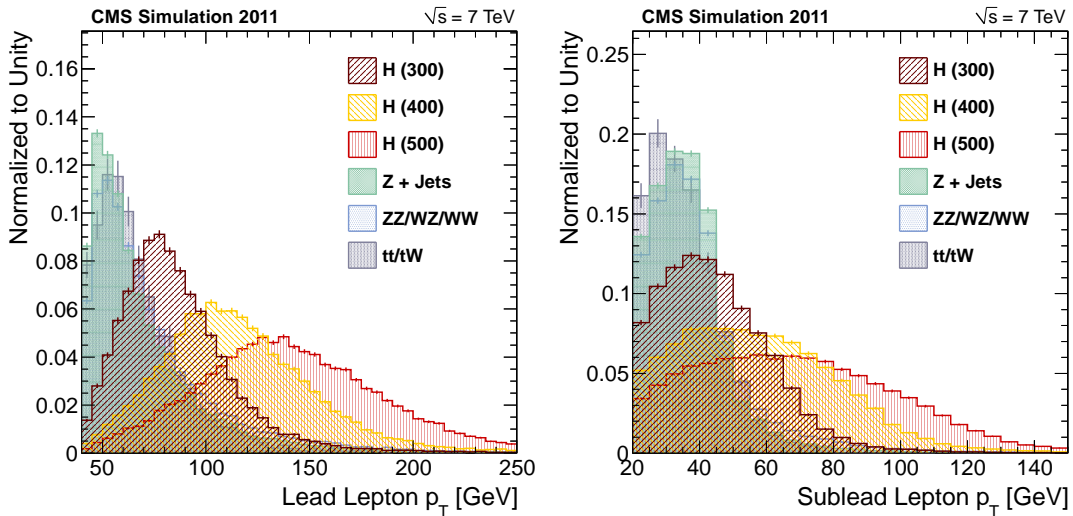
Figure 14: Lepton transverse momentum after loose selection requirements in the analysis, leading lepton on the left, and the sub-leading lepton on the right.
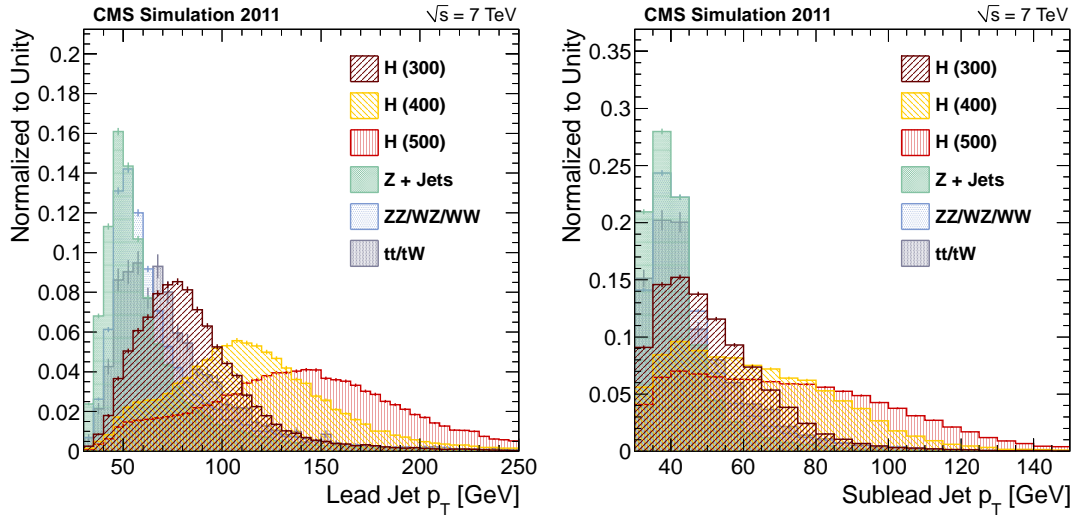
Figure 15: Jet transverse momentum after loose selection requirements in the analysis, leading jet on the left, and the sub-leading jet on the right.
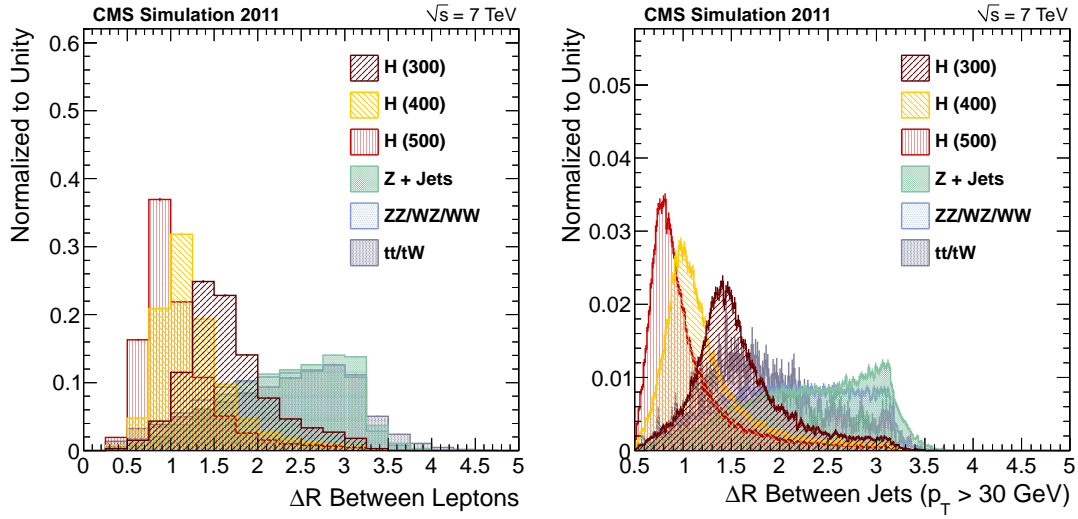
Figure 16: Separation ΔR after loose selection requirements in the analysis, between two leptons on the left, and between two jets on the right.

There is also good agreement between data and MC for the kinematic variables discussed above, as shown in Fig. 17 p_T of the Z and ΔR, and in Figs. 18 and 19 for lepton and jet p_T.
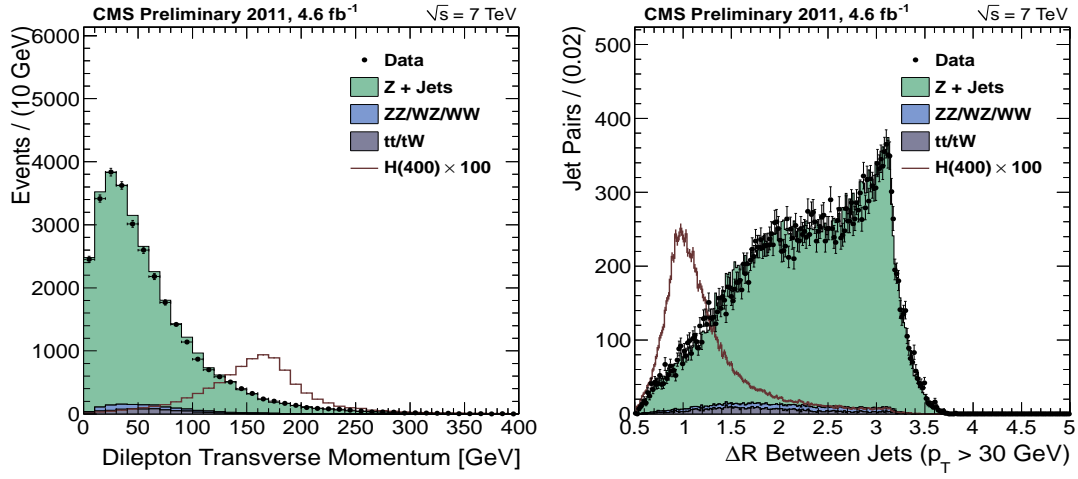
Figure 17: Comparison of 2010-2011 data and MC simulation with dominant contributions for p_T of the Z and ΔR_{jj}.
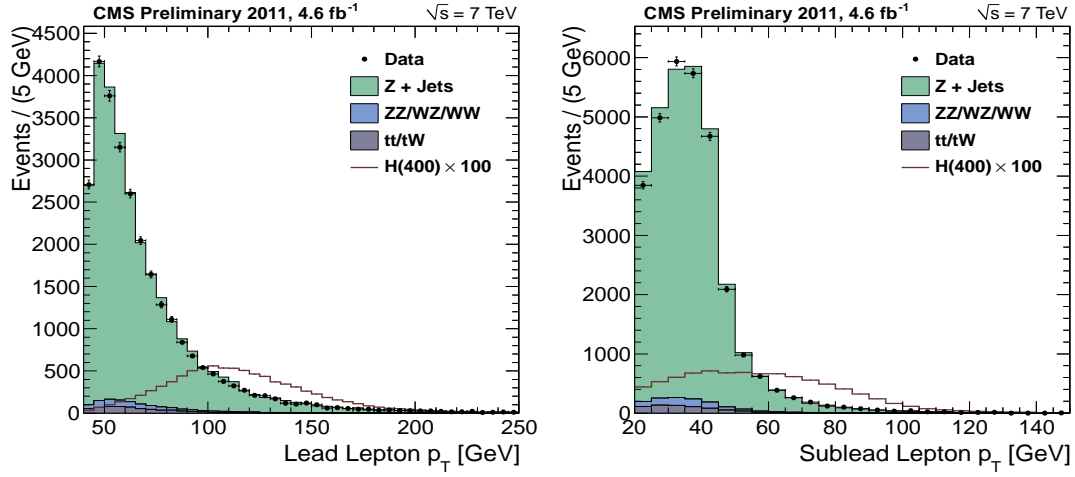
Figure 18: Comparison of 2010-2011 data and MC simulation with dominant contributions for lepton p_T.
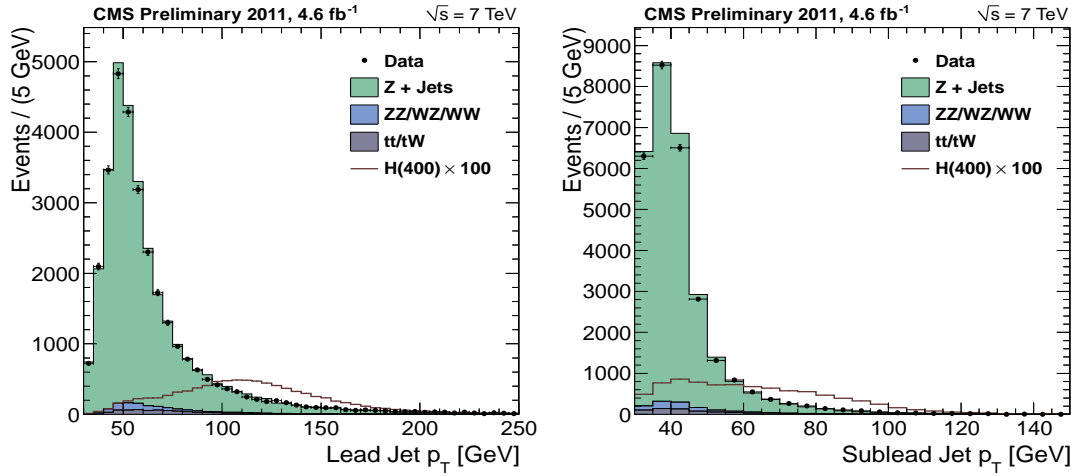
Figure 19: Comparison of 2010-2011 data and MC simulation with dominant contributions for jet p_T.

20

4.2 Angular distributions and data-MC validation

It has been shown in Ref. [7, 8] that five angular observables fully describe kinematics in the decay $2 \rightarrow 1 \rightarrow 2 \rightarrow 4$ as in $ab \rightarrow X \rightarrow ZZ \rightarrow 2l2j$, and they are orthogonal observables to the three invariant masses of the X and the two Z. We should note that longitudinal and transverse momenta of the X are also additional orthogonal observables and could be used in analyses, but they typically have weaker discrimination power and rely on modeling of the PDFs and process dynamics. The above orthogonal observables are largely uncorrelated and are more attractive to be used in event selection rather than raw kinematic observables discussed in Section 4.1.

In Fig. 20 we illustrate the angular distribution in the production and decay chain $ab \rightarrow X \rightarrow P_1 P_2 \rightarrow p_{11} p_{12} p_{21} p_{22}$ with an example of the $ab \rightarrow X \rightarrow ZZ \rightarrow 4l$ or $2l2q$ (where quarks q hadronize to jets, which we refer to as $2l2j$ channel later) chain with two partons a and b, such as gg or $q\bar{q}$. The angular distribution can be expressed as a function of three helicity angles θ_1, θ_2, and Φ, and two production angles θ^* and Φ_1, as shown in Fig. 20. More details can be found in Refs. [2, 7], where parameterization of both signal and background distributions have been derived and implemented.

Here θ_i is the angle between the direction of the l^- or q from the $Z \rightarrow l^+ l^-$ or $q\bar{q}$ (where the quark-antiquark pair produces two jets) and the direction opposite the X in the Z rest frame, and Φ is the angle between the decay planes of the two Z systems. The two Z's are distinguished by their decay type or, in case their daughters are the same type of particles, by an arbitrary convention. The production angle θ^* is defined as the angle between the parton collision axis z and the X decay axis in the X rest frame. The fifth angle can be defined as Φ_1, an angles between the production plane and the first Z decay plane.

A comparison of angular distribution in data and Monte Carlo can be found in Fig. 21, where we find good agreement for background.
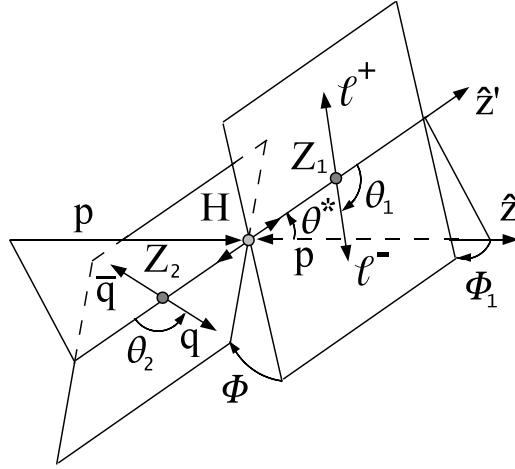
Figure 20: Diagram depicting the decay $X \rightarrow ZZ \rightarrow 2e2\mu$ and the 5 angles which describe such a decay.

4.3 Angular discriminant: method

Previous work in Ref. [2] has concentrated on using angular information with a likelihood method for extracting signal and background yields from fits. Here we have chosen to adapt this information into a cut-and-count approach by, instead, building a likelihood discriminant from the angular distributions. While some statistical power is lost in reducing the MVA likelihood fit to a 1D discriminant, we gain in simplicity. For example, even if some parameterization of either signal or background effect is not perfect in the likelihood parameterization, the analysis is still not biased, it is only slightly less optimal than with the perfect description.

Assuming the probability distributions of the five helicity angles for both signal and background are known, P_{sig} and P_{bkg} respectively, the likelihood discriminant in given by the probability ratio

$$LD = \frac{P_{bkg}}{P_{sig} + P_{bkg}}.$$

This function has the feature that the signal is most likely to have values close to one and the background is most likely to have values close to zero. Events are then selected by requiring LD to be above certain threshold. This

Figure 21: Five angular distributions of $\cos\theta_1$, $\cos\theta_2$, $\cos\theta^*$, Φ, and Φ_1 for 2010-2011 data (points) and Spring11 Monte Carlo samples (histogram).

method of selection has been shown to provide at least similar results to those obtained using a set of optimized kinematic cuts. Furthermore, since the helicity angles are largely decoupled from the ma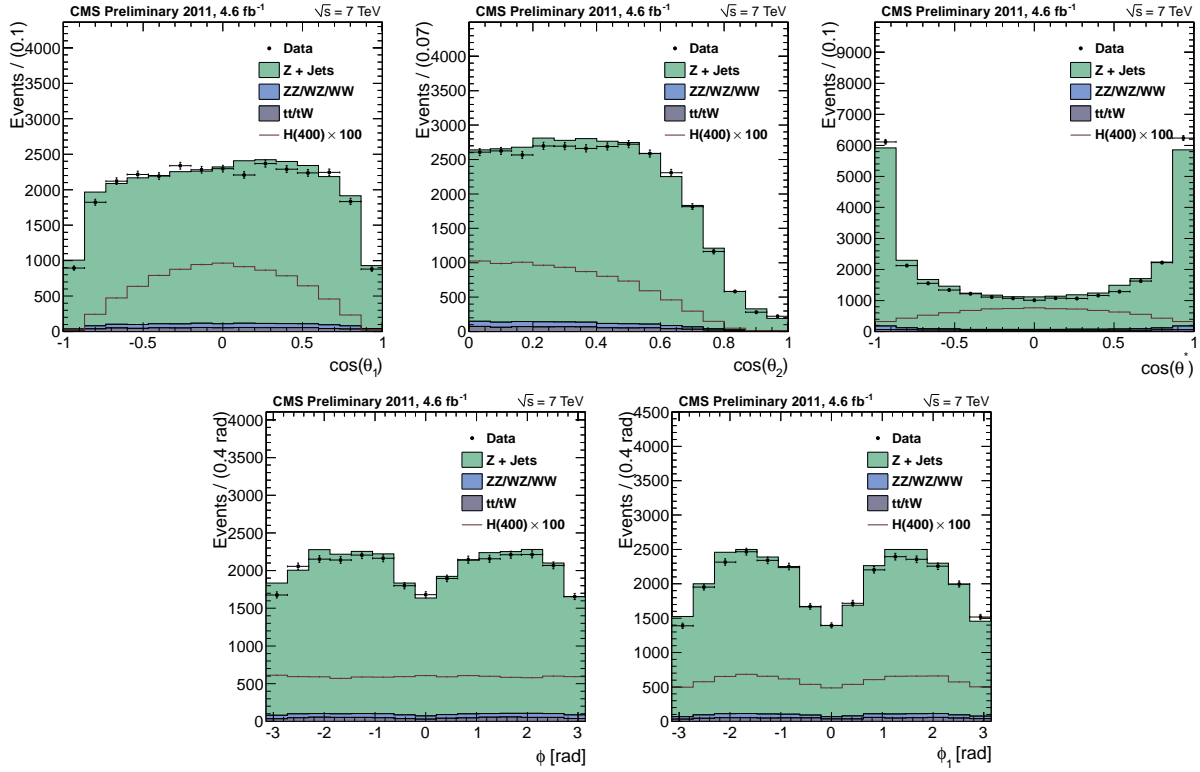ss variables, by making selections based on the helicity likelihood discriminant one can better preserve the shape of the background's ZZ invariant mass distribution than with tight kinematic cuts. The method for obtaining such a likelihood discriminant is described below.

The probability distribution function for signal was taken to be a product of the ideal, fully correlated, distribution which is derived in Ref. [7] and a set of four one-dimensional acceptance functions.

$$\mathcal{P}_{\text{sig}} = \mathcal{P}_{\text{ideal}}(\theta^*, \theta_1, \theta_2, \Phi, \Phi_1; M_{ZZ}) \cdot \mathcal{G}_{\theta^*}(\theta^*; M_{ZZ}) \cdot \mathcal{G}_{\theta_1}(\theta_1; M_{ZZ}) \cdot \mathcal{G}_{\theta_2}(\theta_2; M_{ZZ}) \cdot \mathcal{G}_{\Phi_1}(\Phi_1; M_{ZZ})$$

The four acceptance functions, $\mathcal{G}_{\theta^*}, \mathcal{G}_{\theta_2}, \mathcal{G}_{\theta_2}$, and $\mathcal{G}_{\Phi_1}$, have been obtained empirically from fits to Monte Carlo. Projections of $\mathcal{P}_{\text{sig}}$ can be seen in Fig. 22.

Where as the ideal function, $\mathcal{P}_{\text{ideal}}$, is naturally parameters with the ZZ invariant mass, the parameters of the four acceptance functions have all been re-parameterized in terms of m_{ZZ} only. This was done by fitting eight different Monte Carlo samples each corresponding to a different Higgs mass and then fitting the resulting parameters with either a linear or quadratic function of m_{ZZ}.

The probability distribution function for the background was approximated with a product of five one-dimensional functions.

$$\mathcal{P}_{\text{bkg}}(\theta^*, \theta_1, \theta_2, \Phi, \Phi_1; M_{ZZ}) = \mathcal{P}_{\theta^*}(\theta^*; m_{ZZ}) \cdot \mathcal{P}_{\theta_1}(\theta_1; m_{ZZ}) \cdot \mathcal{P}_{\theta_2}(\theta_2; m_{ZZ}) \cdot \mathcal{P}_{\Phi}(\Phi; m_{ZZ}) \cdot \mathcal{P}_{\Phi_1}(\Phi_1; m_{ZZ})$$

All functions were obtained empirically from fits to Monte Carlo. Projections of $\mathcal{P}_{\text{bkg}}$ can be found in Fig. 23.

Similar to the case of $\mathcal{P}_{\text{sig}}$, the background Monte Carlo was divided into bins of m_{ZZ} and each bin was fit with $\mathcal{P}_{\text{bkg}}$. The parameters from each fit were then fit using either linear or quadratic functions of m_{ZZ}.

Combining $\mathcal{P}_{\text{sig}}$ and $\mathcal{P}_{\text{bkg}}$ into LD, we end up with the discriminant that is a function of the five helicity angles and parameterized by a given event's ZZ invariant mass. An example of the helicity likelihood discriminant is plotted in Fig. 24 for both background and signal Monte Carlo after loose kinematic selections .

22

4.4 Angular discriminant: data-MC validation

There is a good agreement in the likelihood discriminant (LD) distribution between data and background MC shown in Fig. 25, as it is expected based on agreement of variables entering the LD calculation.
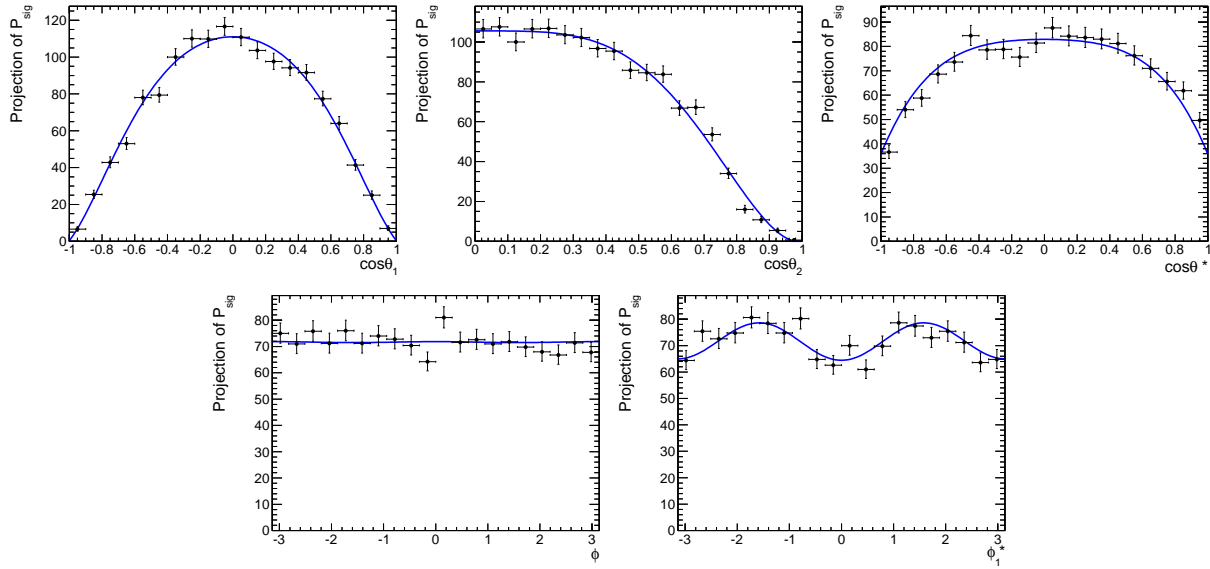
Figure 22: Distributions of $\cos\theta_1, \cos\theta_2, \cos\theta^*, \Phi$, and Φ_1 for a 500 GeV Higgs boson.
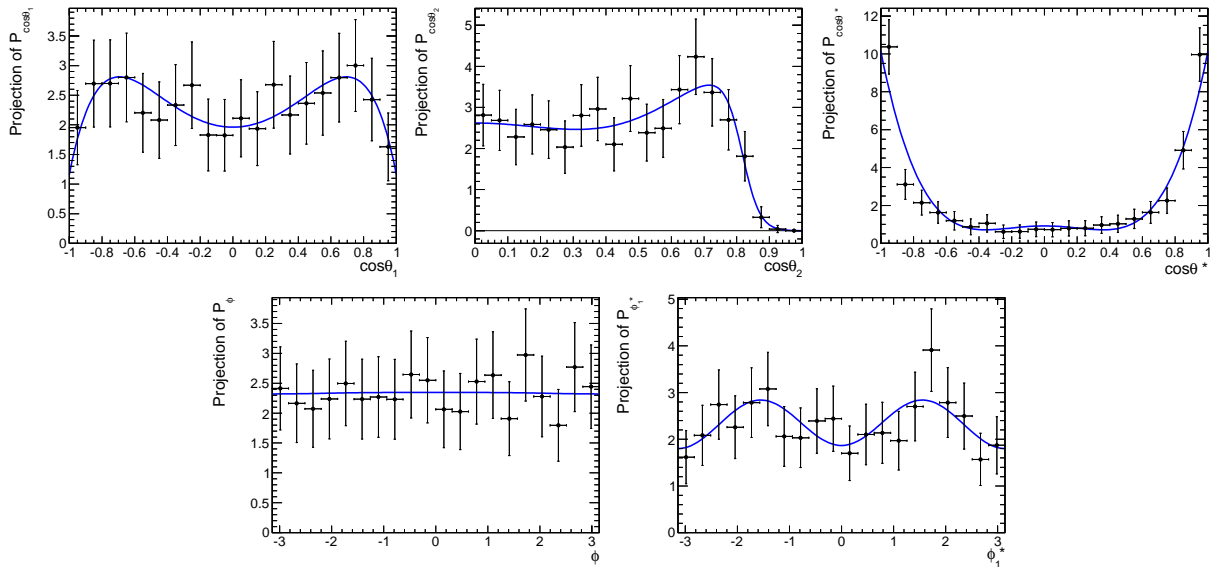
Figure 23: Distributions of $\cos\theta_1, \cos\theta_2, \cos\theta^*, \Phi$, and Φ_1 for background around 500 GeV.

23
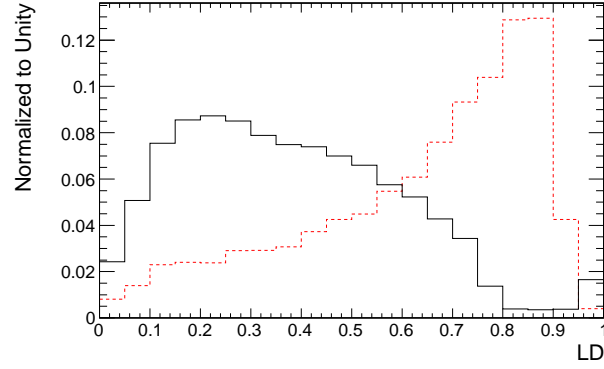
Figure 24: Distribution of the helicity likelihood discriminant plotted for a 500 GeV Higgs signal (dashed lines) and background (solid lines) Monte Carlo.
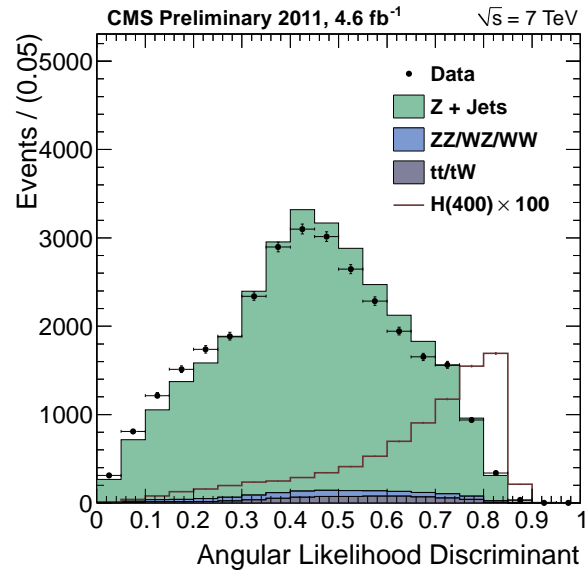
Figure 25: Comparison of helicity likelihood discriminant in 2010-2011 Data (points) and Fall10 Monte Carlo (histogram). Signal sumulation has been enhanced by a factor of 200 for illustration.

5 Jet Structure, Jet Flavor Tagging, and MET

A powerful handle in the signal to background discrimination is offered by the jet parton flavor. Jets in signal events are produced in hadronic decays of a Z boson, and therefore originate from the hadronization of quark partons. The flavor of quarks in Z decays is almost equally distributed among the five types d, u, s, c, b, with some preference given to the down-type quarks due to preferential electroweak couplings of the Z. The dominant background, as we have seen, is represented by a leptonically-decaying Z boson produced in association with hard jets, a process in which gluon radiation is expected to play a major role. After gluons, the u and d quarks from the protons dominate the jet production associated with the Z. Therefore, the main features which discriminate signal from background is the relatively large contribution of heavy flavor quarks (b and c) and absence of gluons. We take advantage of both features in analysis by performing tagging of the b-flavor and introducing a novel discriminant which separates gluon and light quark jets on a statistical basis, as we discuss below.

Our overall analysis strategy is to split events into four categories

- 2 b-tag category: both jets are positively identified as b (low background);

- 1 b-tag category: one jet is positively identified as b (intermediate case);

- 0 b-tag category: none of the above, and not glue-tag either (high background and high signal efficiency);

- glue-tag category: two jets are jointly tagged as glue-like (predominantly background).

Figure 26 illustrates the above statements and shows the PDG [19] identification number (PDG ID) of partons matched to the jets which pass the kinematic selection optimized for $m_\mathrm{H} = 400$ GeV/c^2, both in signal (here Higgs masses of 400 GeV/c^2 and 500 GeV/c^2 are considered) and in background events. The left plot refers to the leading jet, the right one to the subleading jet. The PDG IDs of quarks follow the mapping scheme d, u, s, c, b, t for 1,2,3,4,5,6. Antiquarks have opposite PDG IDs, whereas gluons are assigned a value of 21. As can be seen in the figure, the kinematic selection in signal selects only quarks jets. It is furthermore orthogonal to parton flavor, as the jets which pass the selection are equally shared between all available quark flavors (excluding the top quark which is energetically forbidden). The observed enhancement of down-type quarks (d, s, b) is a direct consequence of the asymmetric coupling of the Z boson.

The jet flavor population for background $Z+$ jets events is radically different. More than 45% (60%) of the selected leading (subleading) jets originate from the hadronization of a gluon. Also the quark population shows some differences: the observed u and d enhancement is mirroring the proton valence quark parton density functions (largest u contribution, and the next largest d). The contribution of heavy flavors, b in particular, is small in background, while it is about 22% is signal. We should note that in Fig. 26 heavy flavor production was not included in $Z+$jets MC simulation, but it is small as evident from cross-sections in Tables **??** and **??**.
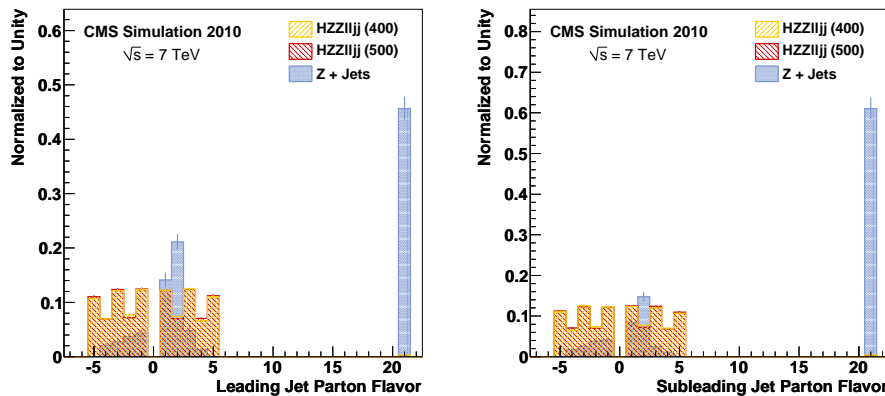
Figure 26: PDG ID of partons matched to jets passing full event selection: d, u, s, c, b, t correspond to 1,2,3,4,5,6, antiquarks are negative, and gluon is 21. Leading jet partons is shown on the left, subleading jet partons is on the right. Signal events for two Higgs boson masses (400 GeV/c^2 in yellow and 500 GeV/c^2 in red) are compared to $Z+$jets background events (blue) generated without direct production of heavy-flavor quarks. Distributions are normalized to unity.
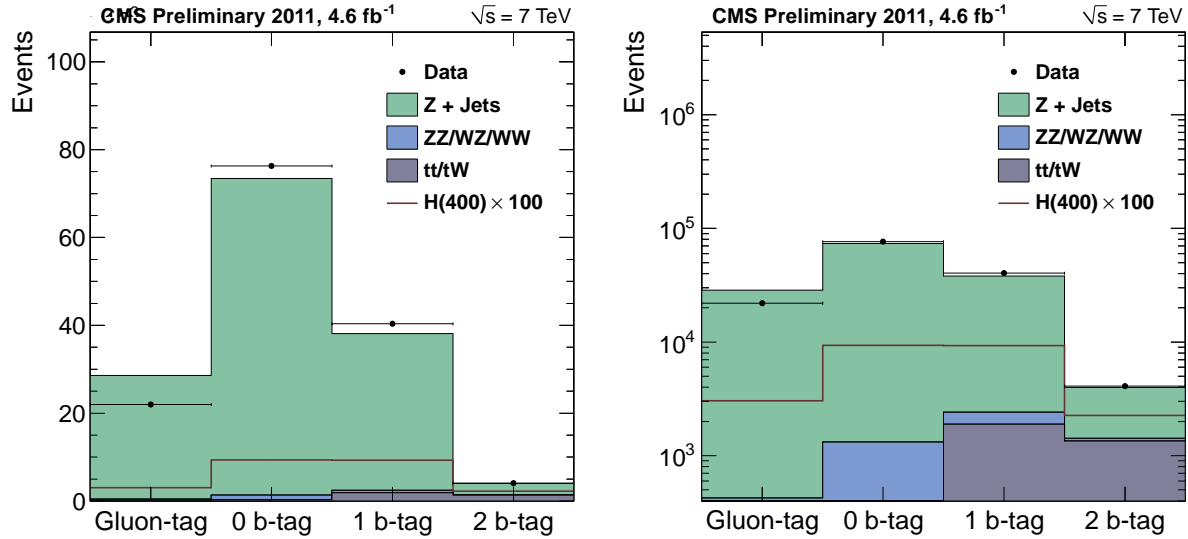
Figure 27: Distribution of events in the four jet flavor categories at pre-selection. Comparison of 2010-2011 data and MC with the dominant background contributions is shown. Signal is enhance by a factor of 200 for illustration. The plots differ by scale on the y-axis.

Figure 27 shows distribution of events in the four jet flavor categories at pre-selection where comparison of 2010-2011 data and MC with the dominant background contributions is shown. Some small disagreement in the glue-tag category is caused by the sub-leading jet quark-glue discriminant which is discussed below. However, background prediction in the relevant category is estimated from sidebands and is not sensitive to this small discrepancy.

5.1 Heavy flavor jet tagging

The default b-tagging algorithm in this analysis is the Track Counting High Efficiency (TCHE) [22]. The data are split in three b-tag categories. The 2 b-tag category is required to have one jet identified with medium (BJetTag>3.3) and the other jet with loose requirements (BJetTag>1.7). The 1 b-tag category is required to have one jet identified with loose requirements, while the other jet should fail medium requirements. The 0 b-tag category contains all events which are not selected in the above two categories.

Other algorithms, such as Track Counting High Purity (TCHP) and Simple Secondary Vertex High Efficiency (SSVHE), and other combinations of loose, medium, and tight thresholds have been investigated. The alternative selection close in performance to the default strategy is with the TCHE algorithm where both requirements require medium thresholds (BJetTag>3.3).

For more details of b-tag performance see Refs. [?, 22]. Further discussion of results of the above selection is provided in Sections 6 and 9.

5.2 Missing transverse energy

Without further selection, in the 2 b-tag category the dominant background originates from $t\bar{t}$ decay chain which contains two true b quark jets. We further reduce this background with a particle flow MET significance requirement of less than 10.

The distribution of PF MET significance for three Higgs mass hypotheses (300, 400, and 500 GeV) and the $t\bar{t}$ background are shown in Fig. 28. We have also considered selection based on mass-dependent requirement on MET directly, as illustrated in the left plot of Fig. 28. However, we find MET significance to be more physically motivated quantity.

Efficiency of the MET significance requirement of less than 10 varies between 99.0% at 250 GeV to 97.4% at 500 GeV for the signal Higgs candidates. This rather loose requirement is expected to be robust even in the presence of PileUp.
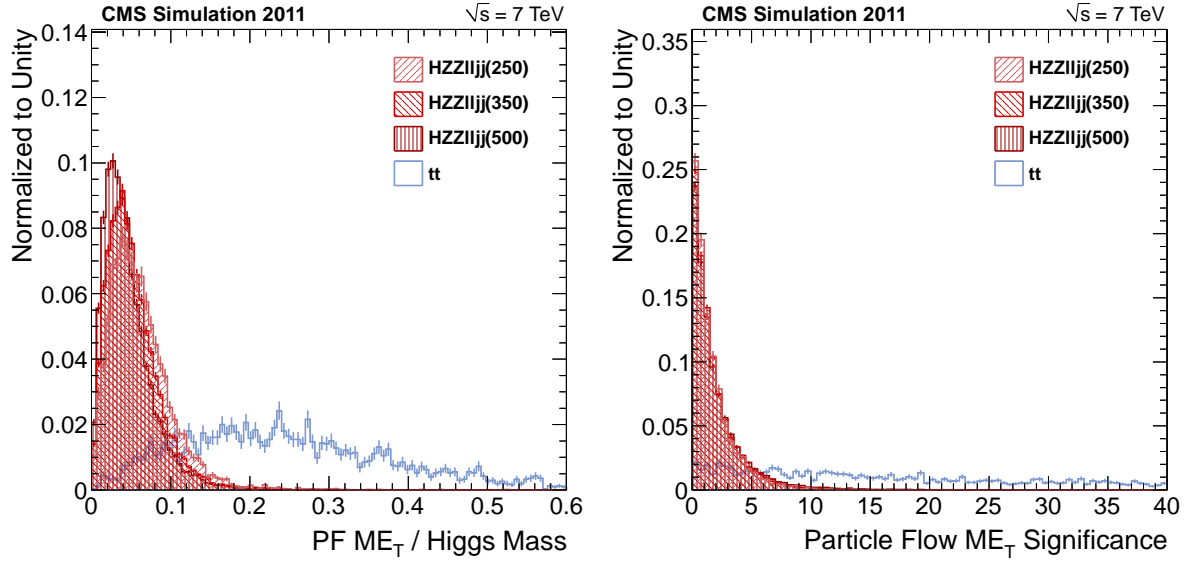
Figure 28: Left: PF MET divided by the Higgs candidate mass m_{ZZ}. Right: PF MET significance. Three Higgs mass hypotheses (300, 400, and 500 GeV) and the $t\bar{t}$ background distributions are show.

5.3 Quark-gluon discriminant

In the 0 b-tag category the dominant background originates from the Z+jets process with substantial contribution of gluon jets, while signal is dominated by hadronic Z decays to light quarks. Therefore identification of gluon jets helps to further reduce background. On the other hand the 1 b-tag category still has large fraction of Z decays to heavy flavor quarks in signal. Topology of the heavy flavor jets and gluon jets is similar, and therefore we do not attempt to achieve quark-glue discrimination in the 1 and 2 b-tag categories.

Gluons have a more intense coupling to the strong field than quarks, therefore their hadronization favors the production of a larger number of stable particles. This translates, in the detector, in the observation of wider, high-multiplicity jets, when compared to those generated by final state quarks. Furthermore, the phenomenon of 'gluon-splitting', if occurring at the beginning of hadronization, may give rise to jets made a number of collimated sub-jets.

These structural differences between gluon and quark hadronization may be exploited to derive a likelihood based discriminant. A more detailed description of this method may be found in [23].

The Particle Flow jet reconstruction method exploits all CMS subdetectors to their maximal granularity. It therefore offers the most detailed information on jet composition at particle level. The following variables are considered:

- **charged multiplicity**: number of charged hadron PFCandidates present in the jet;

- **neutral multiplicity**: number of photon and neutral hadron PFCandidates present in the jet;

- **transverse momentum distribution** among candidates ($P_\mathrm{T}D$), defined as:

$$P_\mathrm{T}D = \sqrt{\frac{\sum p_\mathrm{T}^2}{\left(\sum p_\mathrm{T}\right)^2}}$$

where the sums are extended over all PFCandidates in the jet.

We expect gluon jets to present higher values of charged and neutral multiplicities with respect to quark jets, and lower values of $P_\mathrm{T}D$, as is shown in Figs. 29 for a representative jet transverse momentum bin.

These three variables can be combined into a likelihood, defined as a simple product of the single-variable distributions. The probability density functions are taken from MC QCD events, in which jets are matched to a parton in order to define their flavor. The expected likelihood distribution, for quark and gluon jets in the same jet transverse momentum bin, is shown in Fig. 30.
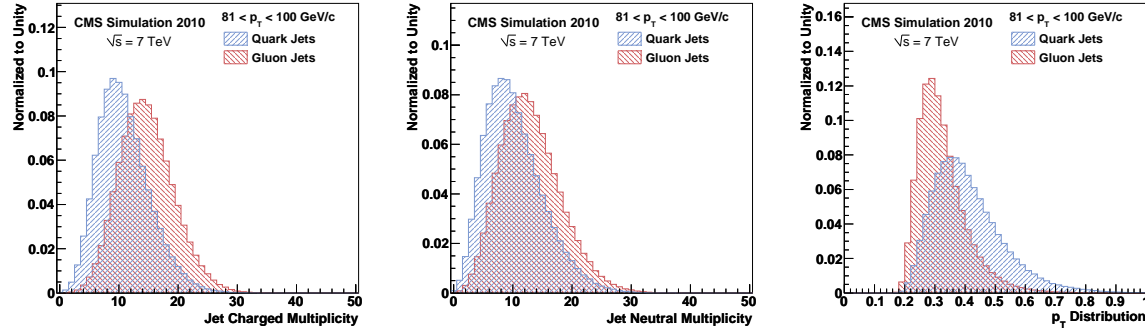
Figure 29: Multiplicity of charged PFCandidates in quark (red) and gluon (blue) jets. All distributions are normalized to unity.
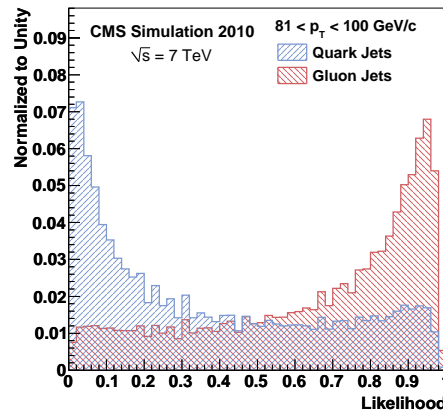
Figure 30: Multiplicity of charged PFCandidates in quark (red) and gluon (blue) jets. All distributions are normalized to unity.

The expected likelihood distributions, for the leading and subleading jets passing the aforementioned kinematic selections, are shown in Figs. 31, 32, and 33 for three Higgs masses ranges. Separation power improves at higher masses (with harder jets).

Data-MC comparisons of the discriminant, for leading and subleading jets passing preselection cuts, are shown in Fig. 34. There is a visible discrepancy in the distribution of the subleading jet. As will be shown in Section 8.5, we have no indication that the discriminant is performing differently from expected on quark jets. Further, even if we are limited in statistical power by the available data, there is no significant discrepancy yet for what concerns the leading jet. We therefore assume that the origin of the discrepancy lies in an incorrect description in the MC of the flavor of the subleading jet parton, i.e. it is more frequent to have it originating from a quark parton in the data than what modeled in the simulation.

The data-based validation of the quark-gluon discrimination likelihood is detailed in Section 8.5 and in [23].
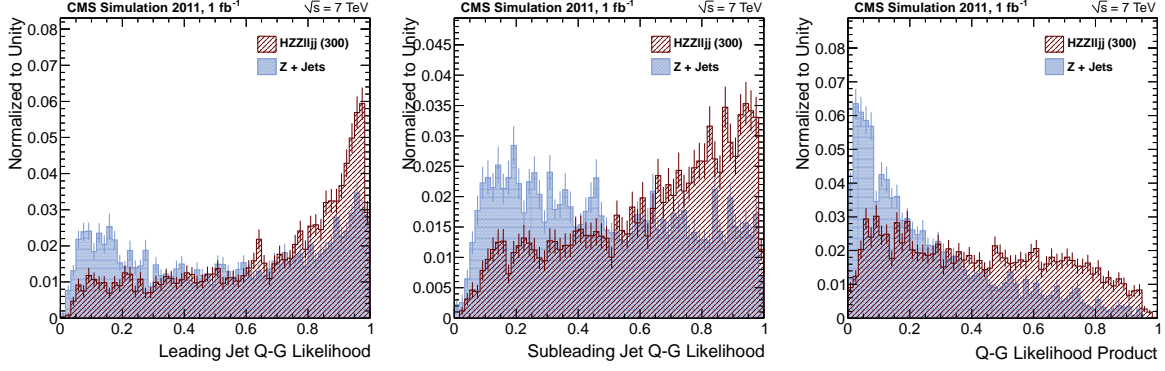
Figure 31: Quark-gluon likelihood distributions for leading jet (left) and subleading jet (center) passing selection, and for the two combined (left). Higgs at 300 GeV and Z+jets background in the range of 300 GeV are shown.
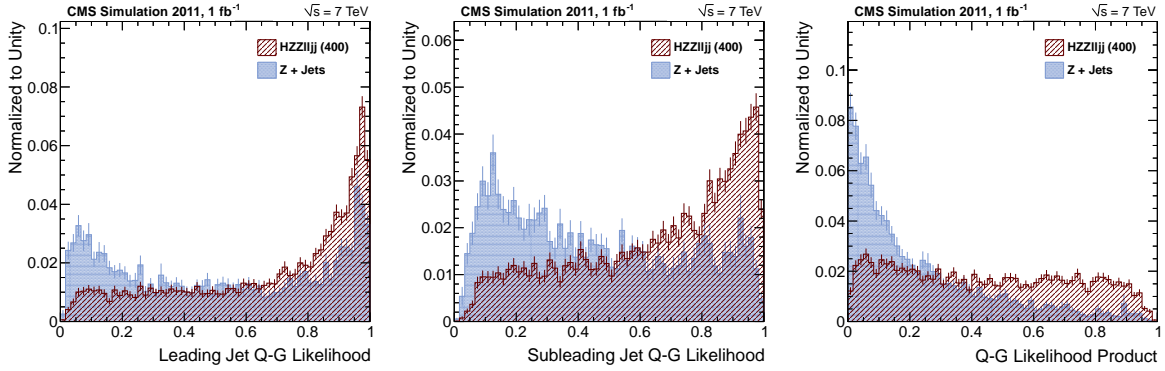
Figure 32: Quark-gluon likelihood distributions for leading jet (left) and subleading jet (center) passing selection, and for the two combined (left). Higgs at 400 GeV and Z+jets background in the range of 400 GeV are shown.

Figure 33: Quark-gluon likelihood distributions for leading jet (left) and subleading jet (center) passing selection, and for the two combined (left). Higgs at 500 GeV and Z+jets background in the range of 500 GeV are shown.

Figure 34: Quark-gluon likelihood distributions for leading jet (top-left) and sub-leading jet (top-right), and combined likelihood (bottom). Points with error bars show data after loose pre-selection, histograms show contribution of dominant background channels with MC.
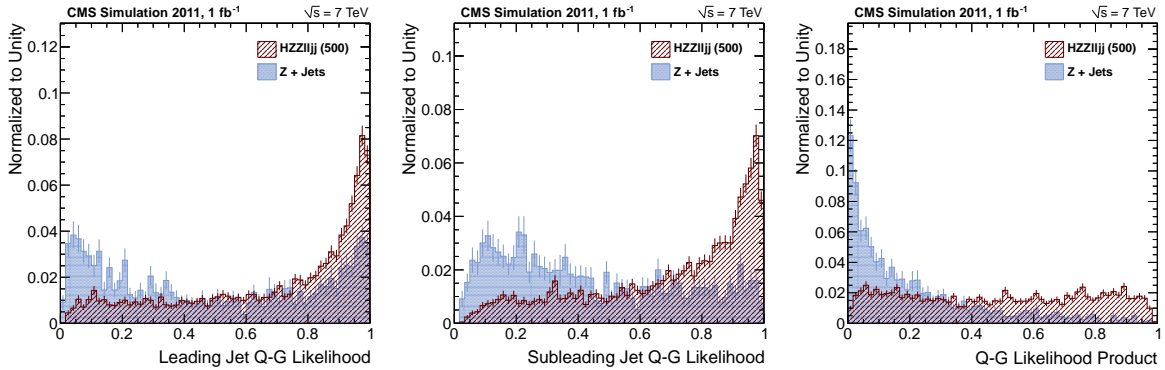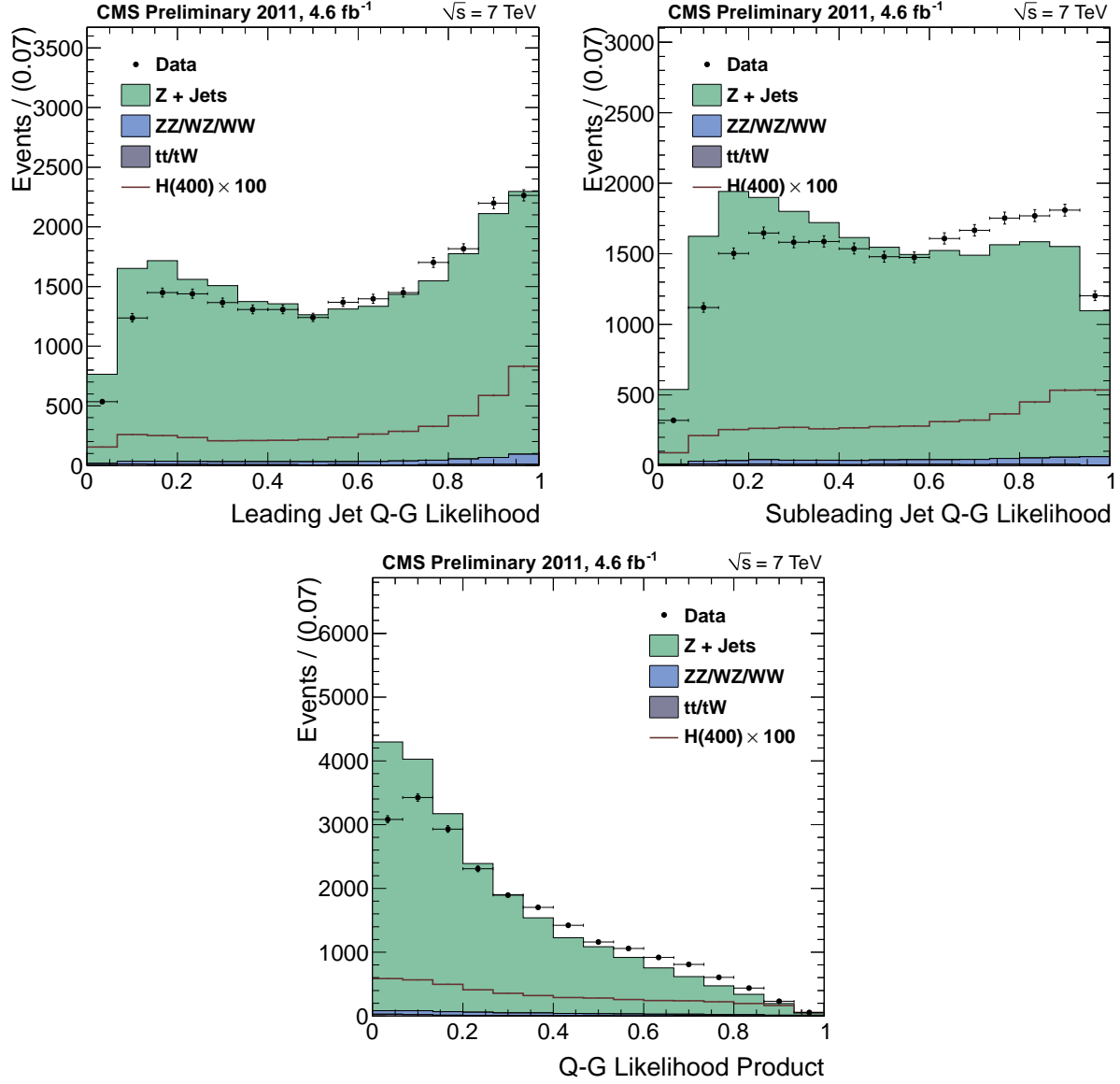
6 Optimization Procedure and Selection Requirements

Optimizing selection based on a large number of kinematic observables is a complicated task and we use the TMVA tool [24] to find an optimal point in a multidimensional space of observables. We employ several complementary approaches. In the default approach we use angular and mass variables and optimize requirement on the likelihood discriminant which is a function of the reconstructed mass m_{ZZ}. In Table 8 we show optimized selection requirements in the three b-tag categories. We remove glue-tag category from further consideration in analysis because it is fully dominated by background.

Table 8: Optimized selection requirements in the three b-tag categories.

	0 b-tag	1 b-tag	2 b-tag
b-tag	none	TCHEL	TCHEM & TCHEL
Helicity LD	$> (0.55 + 0.00025 \times m_{ZZ})$	$> (0.302 + 0.000656 \times m_{ZZ})$	> 0.5
Quark-Gluon LD	> 0.10	–	–
pf MET significance	–	–	< 10
m_{ZZ}	cut&count only $[0.94 \times m_H, 1.10 \times m_H]$		
m_{jj}	[75,105] GeV		
m_{ll}	[70,110] GeV		
	preselection		
$p_T(l^\pm)$	$> 20/40$ GeV		
$p_T(\text{jets})$	> 30 GeV		
$|\eta|(l^\pm)$	$(\text{e}^\pm) < 2.5, (\mu^\pm) < 2.4$		
$|\eta|(\text{jets})$	< 2.4		
lepton quality	see Section 3.2		
jet quality	see Section 3.3		

We with the above default selection, the expected yield (corresponding to 1 fb^{-1} of data) of signal and background events in the full ZZ invariant range [183,800] GeV as listed in Table 9. Further discrimination of signal and background will be achieved with the likelihood fit which uses invariant mass m_{ZZ} distributions. These invariant mass distributions are shown in Fig. 58, where we show three b-tag categories and the glue-tag category. The latter category is fully dominated by background and is removed from further analysis. However, without applying glue rejection, the background in the 0 b-tag category would increase by 34%, 43%, 50%, and 56% at the m_{ZZ} masses around 250, 300, 400, and 500 GeV, respectively. Effect of glue veto on signal is small, since only small fraction of signal events is removed, and those removed events are also more likely to be mis-reconstructed with worse resolution, as shown in Fig. 36.

For further illustration of results, we show various background contributions and split yields in several invariant mass ranges corresponding to typical cut-and-count mass windows to be used in analysis. These expected yields are shown in Tables 10, 11, and 12.

Table 9: List of expected background and signal yields with 1 fb^{-1} of data after all selections and within the ZZ invariant range [183,800].

	0 b-tag yields	1 b-tag yields	2 b-tag yields
$\mu^-\mu^+jj$ background	351.5 ± 5.6	371.2 ± 5.9	23.7 ± 1.6
e^-e^+jj background	304.3 ± 5.4	332.6 ± 5.8	23.6 ± 1.7
200.00 GeV	2.57 ± 0.37	3.43 ± 0.49	0.70 ± 0.19
250.00 GeV	5.34 ± 0.75	4.75 ± 0.67	1.46 ± 0.38
300.00 GeV	5.84 ± 0.83	4.97 ± 0.69	1.75 ± 0.46
350.00 GeV	6.45 ± 0.94	5.61 ± 0.80	2.15 ± 0.56
400.00 GeV	5.33 ± 0.76	4.83 ± 0.67	1.96 ± 0.50
450.00 GeV	3.54 ± 0.53	3.38 ± 0.48	1.43 ± 0.35
500.00 GeV	2.21 ± 0.34	2.21 ± 0.32	0.97 ± 0.24
550.00 GeV	1.36 ± 0.22	1.41 ± 0.22	0.63 ± 0.16
600.00 GeV	0.83 ± 0.21	0.86 ± 0.21	0.39 ± 0.15

Table 10: Expected yields of signal (signal efficiency is shown in parentheses) and background with 1/fb based on simulation in the 0 b-tag category. In each case the two numbers show $2e2j/2\mu2j$ expectations. Tighter m_{ZZ} mass requirements are applied as (-6%,+10%) of the mass.

Mass [GeV]	Signal	Z+Jets	Diboson	tt/tW	Total Background
250	2.2/2.5 (2.10%/2.31%)	81/99	2.8/3.2	0.92/0.97	85/1e+02
300	2.4/2.5 (3.01%/3.13%)	40/53	1.7/2.4	0.25/0.36	42/55
350	2.5/2.5 (3.38%/3.48%)	21/28	1.3/1.5	0.11/0.1	23/29
400	1.8/1.8 (3.28%/3.26%)	11/15	0.74/0.84	0.0076/0.079	12/16
450	1.1/1.1 (2.94%/3.06%)	8.3/7.4	0.59/0.55	0.03/0.0067	8.9/8
500	0.61/0.67 (2.63%/2.89%)	3.3/3.7	0.32/0.4	0/0.0046	3.6/4.1

Table 11: Expected yields of signal (signal efficiency is shown in parentheses) and background with 1/fb based on simulation in the 1 b-tag category. In each case the two numbers show $2e2j/2\mu2j$ expectations. Tighter m_{ZZ} mass requirements are applied as (-6%,+10%) of the mass.

Mass [GeV]	Signal	Z+Jets	Diboson	tt/tW	Total Background
250	1.7/1.9 (1.57%/1.81%)	69/81	2.4/3	7.4/8.4	79/93
300	1.7/1.9 (2.15%/2.40%)	39/48	1.7/1.9	2.8/3.8	44/54
350	1.9/2.1 (2.59%/2.83%)	23/30	0.91/1.2	1/0.93	25/32
400	1.5/1.6 (2.62%/2.85%)	14/19	0.71/0.75	0.34/0.23	15/20
450	0.93/0.98 (2.57%/2.70%)	11/11	0.43/0.5	0.18/0.026	12/11
500	0.55/0.58 (2.36%/2.50%)	7.6/5.6	0.36/0.49	0.065/0.051	8/6.1

Table 12: Expected yields of signal (signal efficiency is shown in parentheses) and background with 1/fb based on simulation in the 2 b-tag category. In each case the two numbers show $2e2j/2\mu2j$ expectations. Tighter m_{ZZ} mass requirements are applied as (-6%,+10%) of the mass.

Mass [GeV]	Signal	Z+Jets	Diboson	tt/tW	Total Background
250	0.71/0.79 (0.66%/0.74%)	5.3/4.8	0.41/0.35	1.2/1.2	6.8/6.3
300	0.82/0.8 (1.03%/1.01%)	2.7/3.1	0.26/0.33	0.48/0.76	3.4/4.2
350	0.9/0.95 (1.22%/1.30%)	1.3/1.5	0.2/0.22	0.14/0.19	1.7/1.9
400	0.7/0.74 (1.26%/1.32%)	0.45/1.3	0.1/0.16	0.022/0.0084	0.58/1.5
450	0.46/0.49 (1.26%/1.34%)	0.63/1.3	0.097/0.16	0.0042/0.048	0.73/1.5
500	0.29/0.3 (1.26%/1.31%)	0.87/0.8	0.1/0.089	0/0.062	0.97/0.95
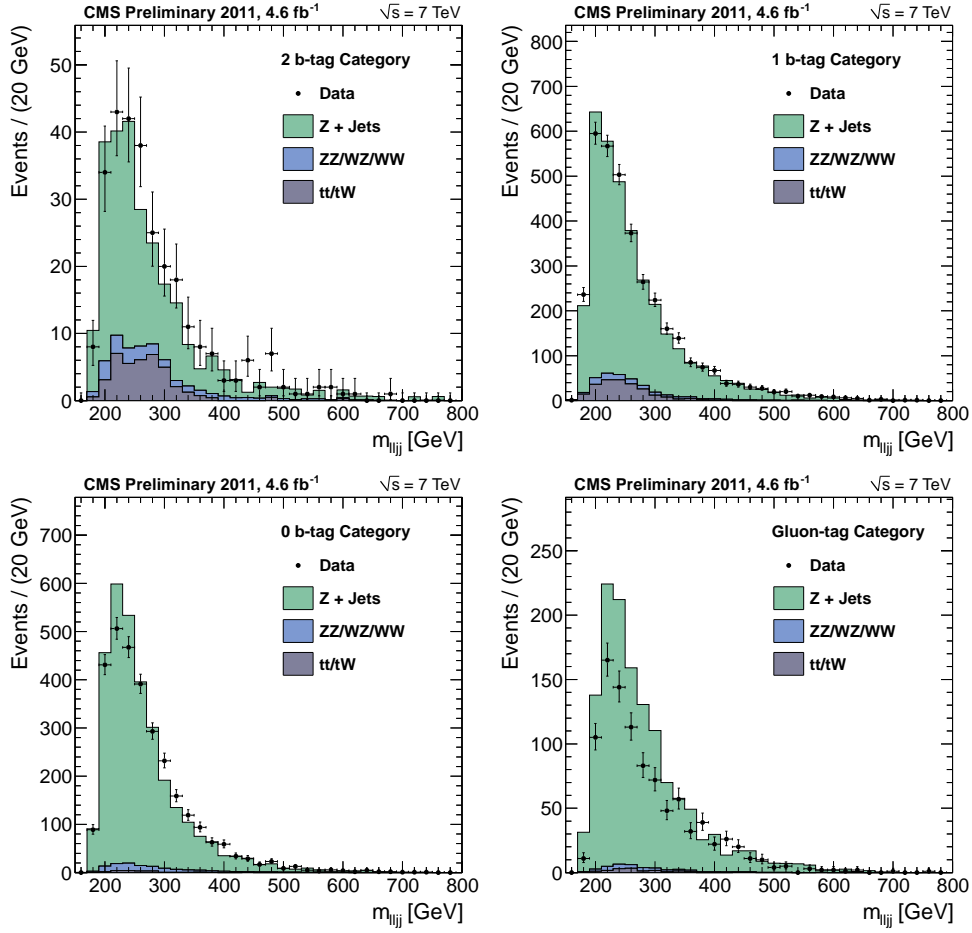
Figure 35: Expected background composition with 1 fb^{-1} of data in four tagging categories: 2 b-tag (top-left), 1 b-tag (top-right), 0 b-tag (bottom-left), glue-tag (bottom-right). Contribution from two SM Higgs hypotheses are shown for comparison.
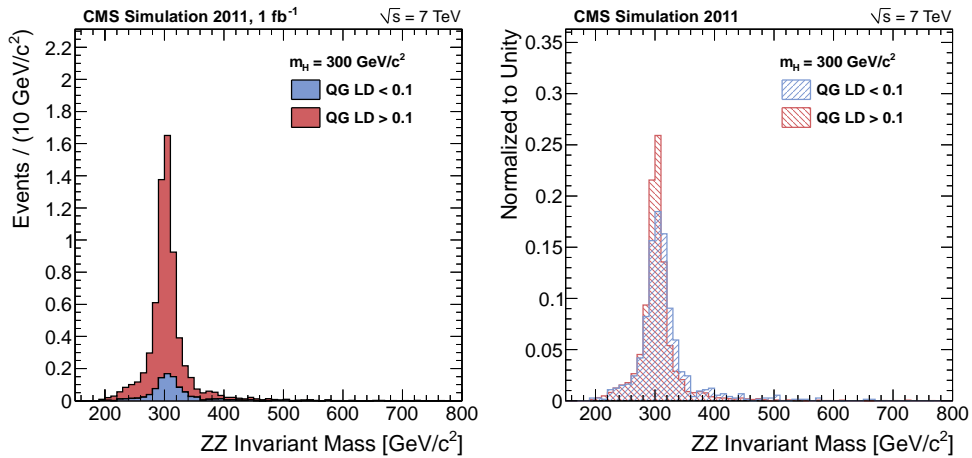
Figure 36: Invariant mass of the Higgs candidate generates at 300 GeV and reconstructed in two tagging categories 0 b-tag (red, higher distribution) and glue-tag (blue, lower distribution). Left plot shows properly normalized distributions, right plot shows the two distributions normalized to the same unit area.

7 Background Estimate

After the final selection, discussed in previous sections, we have three m_{ZZ} distributions corresponding to the three b-tag categories 0 b-tag, 1 b-tag, and 2 b-tag. These distributions are the same for any of the Higgs mass hypothesis analysis. Therefore, they do not change while we change the signal prediction according to a hypothesis under investigation. These three distributions with the currently available data are shown in Fig. 37. We must note that the analysis has been performed blind, that is signal region in data has never been looked at while selection requirements were optimized. Once selection is "frozen," we investigate the m_{JJ} sidebands first, also shown in Fig. 37. Only when we observe an agreement in the sideband, we study the signal region.

In order to minimize systematic uncertainties from MC predictions, we normalize background to sidebands. The procedure is applied independently in each b-tag category since background composition varies between categories. In all cases, the dominant backgrounds include Z+jets with either light or heavy flavor jets and top background. All these backgrounds equally populate the m_{JJ} signal region and m_{JJ} sidebands, as can be seen from Fig. 37. The di-boson background amounts to less than 5% in the 0 and 1 b-tag categories and about 10% in the 2 b-tag category. Even very conservative uncertainty of 30% on MC prediction of the di-boson production would result in only 1-3% uncorrelated contribution to the total background prediction error. Therefore, we have developed a procedure which extrapolates the m_{JJ} sideband distribution of background, as shown in Fig. 37, to the signal m_{JJ} region. This extrapolation accounts for the 5-10% contribution of di-boson production not modeled in sideband using MC prediction. Uncertainties in this procedure result in uncertainties in both normalization and shape parameterization of the m_{ZZ} distributions. It is easy to show that the typical normalization uncertainties due to statistics in the sideband (XXX update numbers) is about 5% in the 0 and 1 b-tag categories and 17% in the 2 b-tag category (expected with 1/fb of data). If we were to rely on MC prediction of background, uncertainties in the b-tag efficiency alone would result in about 20% uncertainty in the 2 b-tag category. Observe good agreement of m_{JJ} distributions in the three b-tag categories and in different m_{ZZ} mass ranges for the range $60 < m_{JJ} < 130$ GeV as shown in Fig. 38.

We can use parameterization of the m_{ZZ} mass spectrum in the the full background MC cocktail in the m_{JJ} signal region and m_{JJ} sideband, as shown in Fig. 37. We create a ratio $\alpha(m_{ZZ})$ between the two, which predicts how sideband data can be scaled to obtain background prediction in the signal region. This is shown in Fig. 39. Since the full cocktail is used, this scale factor accounts for the di-boson production as well, with the small uncertainty discussed above. Then background expectation $N_{\mathrm{bkg}}(m_{ZZ})$ is obtained from distribution of events in the sideband $N_{\mathrm{sb}}(m_{ZZ})$ as follows:

$$N_{\mathrm{bkg}}(m_{ZZ}) = N_{\mathrm{sb}}(m_{ZZ}) \times \frac{N_{\mathrm{bkg}}^{\mathrm{MC}}(m_{ZZ})}{N_{\mathrm{sb}}^{\mathrm{MC}}(m_{ZZ})} = N_{\mathrm{sb}}(m_{ZZ}) \times \alpha(m_{ZZ}) \qquad (1)$$

The advantage of the above approach is that most systematic uncertainties cancel in the ratios while the remaining factor $\alpha(m_{ZZ})$ reflects small kinematic differences between the signal region and sideband, which is mostly independent from the theoretical prediction of cross-sections. This procedure also provides automatic normalization of background and makes any needed adjustments to the shape of the m_{ZZ} mass spectrum should there be any discrepancy. However, we would still like to note that there is very good agreement between data and MC prediction of the m_{ZZ} and m_{JJ} distributions with preselection selection requirement as discussed in previous sections.

To estimate the shape of background in data, the events in the sideband region, $60 < m_{jj} < 130$ GeV excluding the signal region, have been rescaled according to the corresponding $\alpha(m_{ZZ})$ shown in Fig. 39. These distributions are then fit using parameterization derived from MC. The result of such fits are shown in Fig. 40. The fit function used is a Crystall-Ball function, multiplied by Fermi-function to describe the sharp kinematic turn-on at low mass. Only the with of the Gaussian core and of the CB parameterization and the turn-over point to the power-law are free parameters in the fit. The others (Fermi-function postion and width, Crystal-Ball center and powerlaw index) are fixed to values extracted from the simulation. The final fit result are expressed not as function of the the CB witdth and turn-over point directly, but as linear combinations of the two, such that the two resulting free parameters are uncorelated and have a mean of zero with s standard deviation of one. This is done for two reasons: (1) the current version of Higgs combination tools does not allow correlations different from +-100% or zero, so that this manual decorrelation is necessary for accurate uncertainty estimates (2) it allows for the proper inclusion of the statistical uncertainties originating from the limited MC sample used to compute α (discussed below). Figures 41 and 42 show the result of the decorrelation.

The main systematic uncertainties in the above procedure are statistical in nature and scale with the expected size of the sideband data samples. Table 13 shows the expected yield from applying the above procedure and observed yield in each of the 6 channels. The errors on these expectations are on the order of $\sim 5\%$ for the 0 and 1 b-tag

⁵⁵¹ categories and ∼ 20% for the 2 b-tag category. Errors on the shape parameters are taken from fits to the sideband.

⁵⁵² Different models used for simulating the background lead to different α ratio as shown in Figure 39. The ratio
⁵⁵³ using the Sherpa MC [32] differs slightly from the default one using Madgraph, with differences largely covered
⁵⁵⁴ by the statistical uncertainties. Repeating the fit procedure with the Sherpa sample brings changes in the final
⁵⁵⁵ background estimation smaller than the statistical uncertainty of the simulation and they are neglected in the final
⁵⁵⁶ results.

Table 13: Observed and expected yields with 4.6 fb^{-1} of data. The yields are quoted in the range $125 < m_{ZZ} <$ 170 GeV or $183 < m_{ZZ} < 800$ GeV, depending on the Higgs mass hypothesis, while signal extraction requires further analysis of the m_{ZZ} spectrum. The expected background is quoted from the sideband procedure (data) and from simulation (MC). The errors on the expected background from simulation include only statistical uncertainties.

		0 b-tag	1 b-tag	2 b-tag
$m_{ZZ} \in [125, 170]$				
observed yield		1087	360	30
expected background (data)		1129 ± 66	300 ± 27	23 ± 6
expected background (MC)		1393 ± 166	336 ± 76	20 ± 3
$m_{ZZ} \in [183, 800]$				
observed yield		3036	3454	285
expected background (data)		3041 ± 54	3470 ± 59	258 ± 17
expected background (MC)		3105 ± 39	3420 ± 41	255 ± 11
signal expectation (MC)				
	m_H=150 GeV	10.4 ± 1.7	4.3 ± 0.7	1.6 ± 0.3
	m_H=250 GeV	24.5 ± 3.5	21.7 ± 3.0	8.1 ± 1.7
Higgs	m_H=350 GeV	29.6 ± 4.3	26.0 ± 3.7	11.8 ± 2.5
	m_H=450 GeV	16.5 ± 2.4	15.8 ± 2.2	7.9 ± 1.7
	m_H=550 GeV	6.5 ± 1.0	6.5 ± 0.9	3.6 ± 0.8

⁵⁵⁷ In addition to the statistical uncertainties from the data, there are statistical uncertainties on the extrapolation
⁵⁵⁸ factors α due to the limited size of the simulated samples. These uncertainties are propagated to the the final
⁵⁵⁹ background parameterization in the following way: A large number of alternative sets of extrapolation factors is
⁵⁶⁰ randomly generated from from the nominal set of factors, according to their statistical uncertainties. The fit to
⁵⁶¹ the extrapolated sidebands is repeated and the varied extrapolated shape noted. Figure 43 shows a set of these
⁵⁶² alternative fits, showing that the uncertainty due to MC statistics is smaller than the one due to data-statistics, but
⁵⁶³ not negligible.

⁵⁶⁴ The shape parameters derived from these alternative fits are shown in Figure 44. The fact that the varied parameters
⁵⁶⁵ follow a Gaussian distribution centered around the nominal fit value indicates that the width of these Gaussian
⁵⁶⁶ distributions may be added in quadrature to the data statistical errors to include the uncertainty do to limited MC
⁵⁶⁷ statistics.
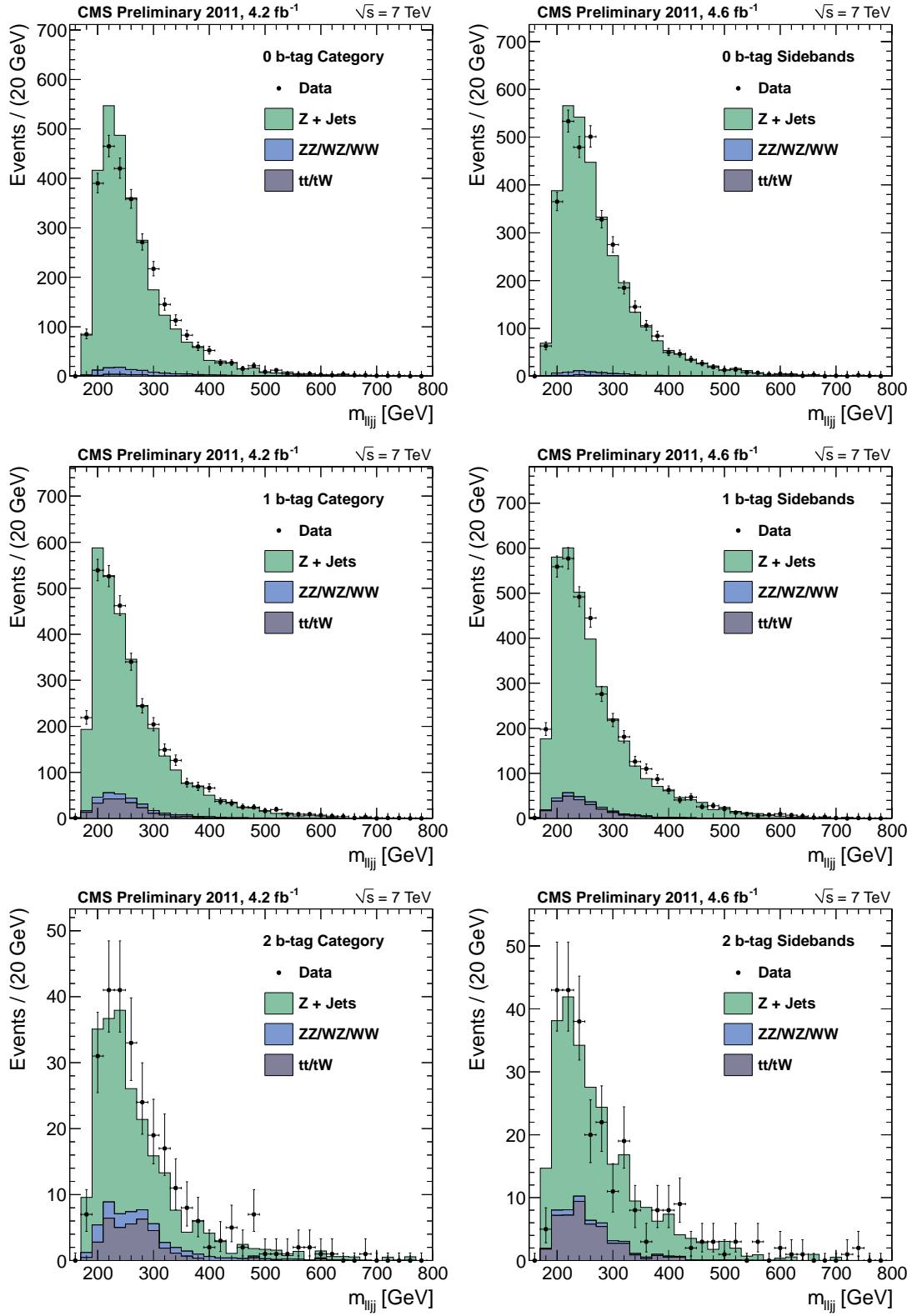
Figure 37: The m_{ZZ} distribution in the three b-tag categories from top to bottom: 0 b-tag (top), 1 b-tag (middle), and 2 b-tag (bottom). left: distribution in the signal m_{JJ} range; right: distribution in the sidband m_{JJ} range. Points with error bars show data after final selection, histograms show MC prediction with the dominant contributions shown separately.
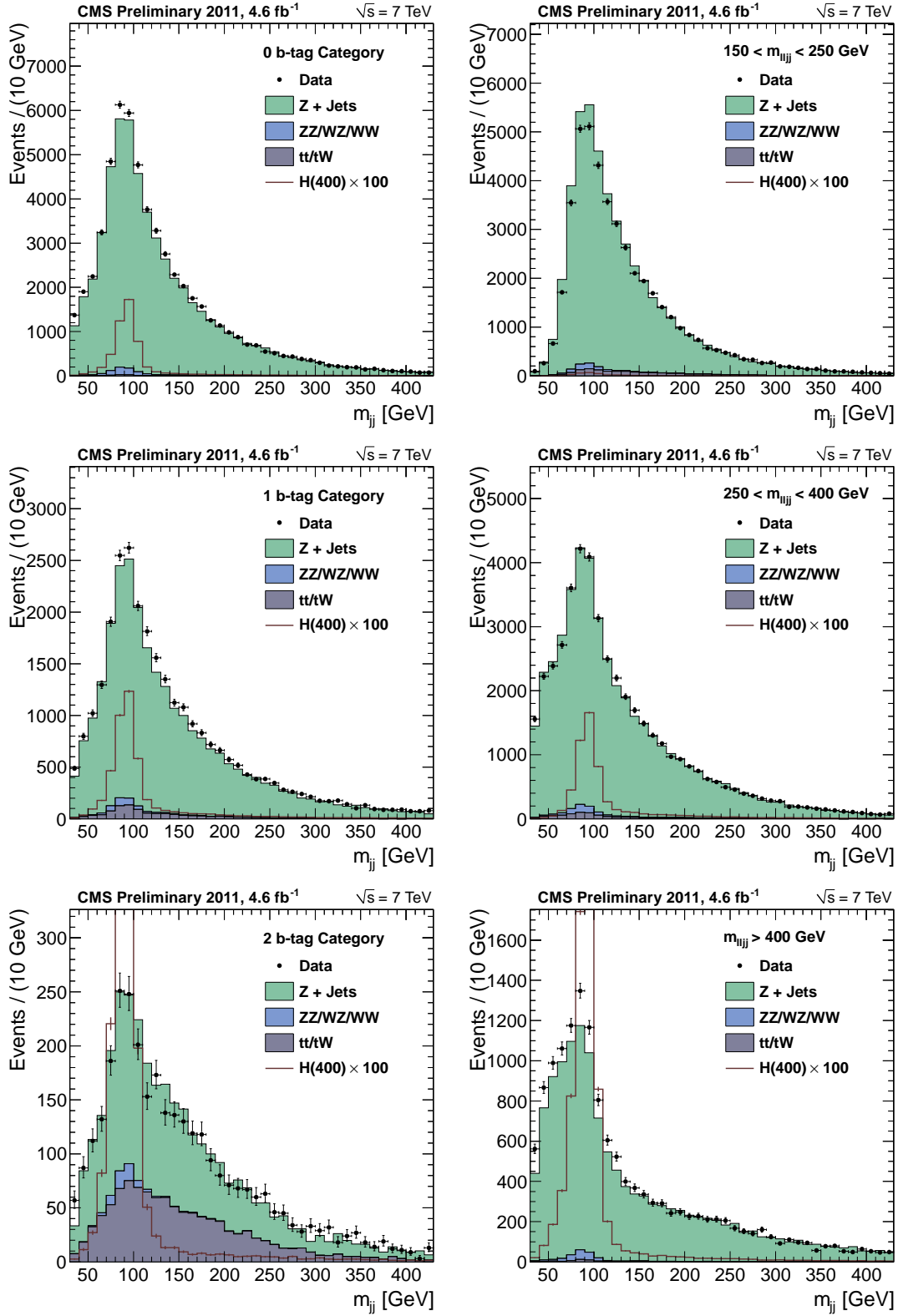
Figure 38: Left column: The m_{jj} distribution in the three b-tag categories from top to bottom: 0 b-tag (top), 1 b-tag (middle), and 2 b-tag (bottom). Right column: The m_{jj} distribution in the three m_{ZZ} mass ranges categories from top to bottom: low (top), middle (middle), and high (bottom).
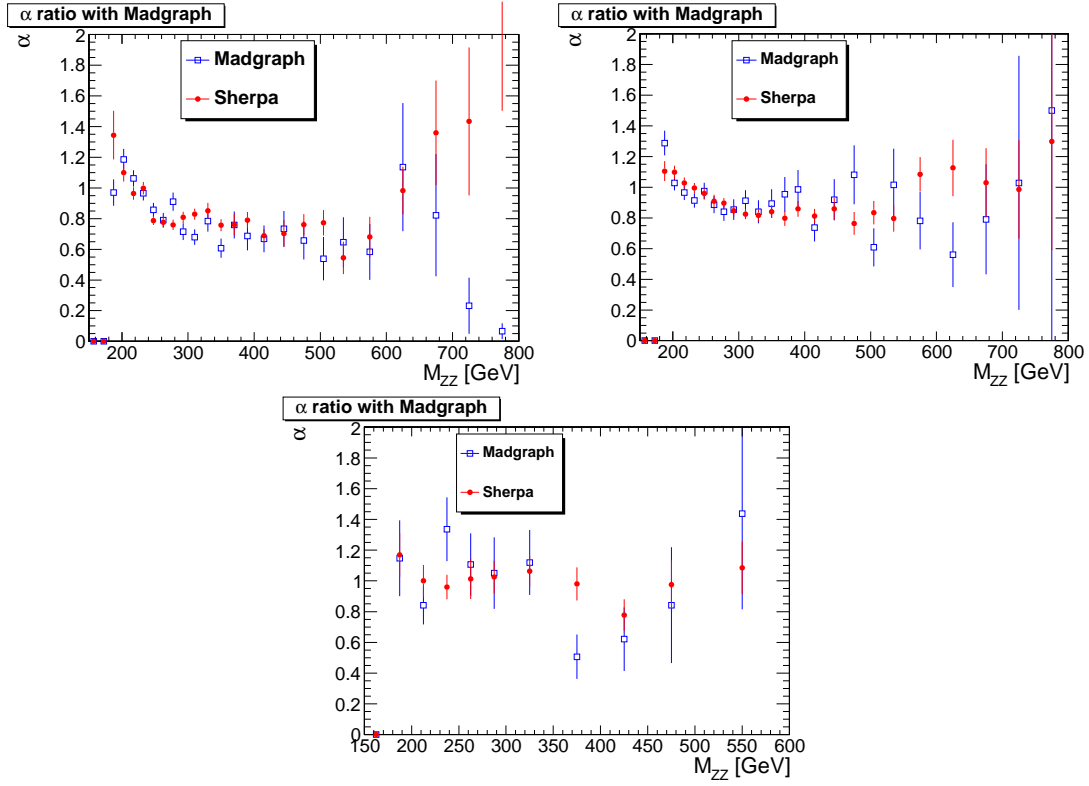
Figure 39: Histograms of $\alpha(m_{ZZ})$ for 0 btag (top left), 1 b-tag (top right), and 2 b-tag (bottom) categories using all relevant MC samples. Two options for Z+jets MC are used: Sherpa and MadGraph.

Figure 40: Fits to sideband data rescale to signal region, using 4.6 fb^{-1} lumi. Three b-tag categories are shown from top to bottom: 0, 1, 2 b-tag. The two parameters of the Crystal-Ball parameterization are allowed to float: linear combinations of the effective width of the core and position of the tail. Left: linear scale, right: log scale.
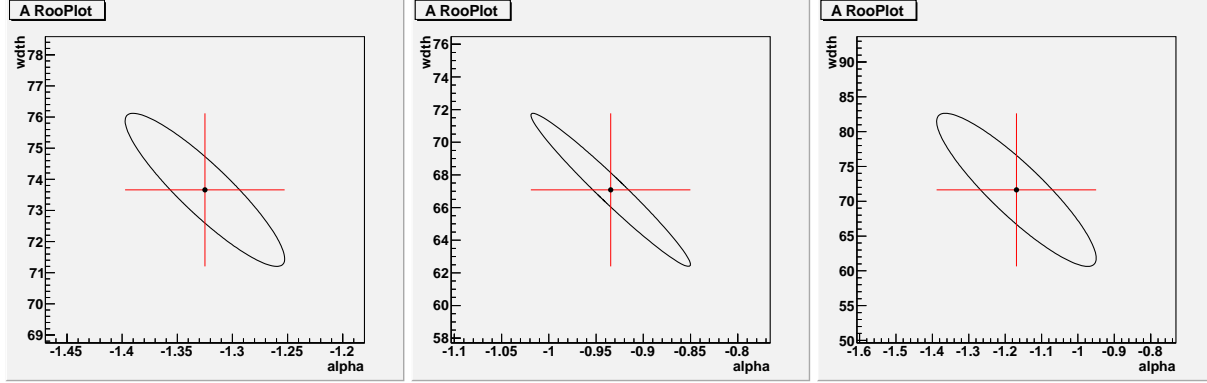
Figure 41: Likelihood contour of the parameters determined in the fit to sideband data shown in Fig. 40. The two parameters indicate effective width of the core and position of the tail of the Crystal-Ball parameterization. Three b-tag categories are shown from left to right: 0, 1, 2 b-tag.
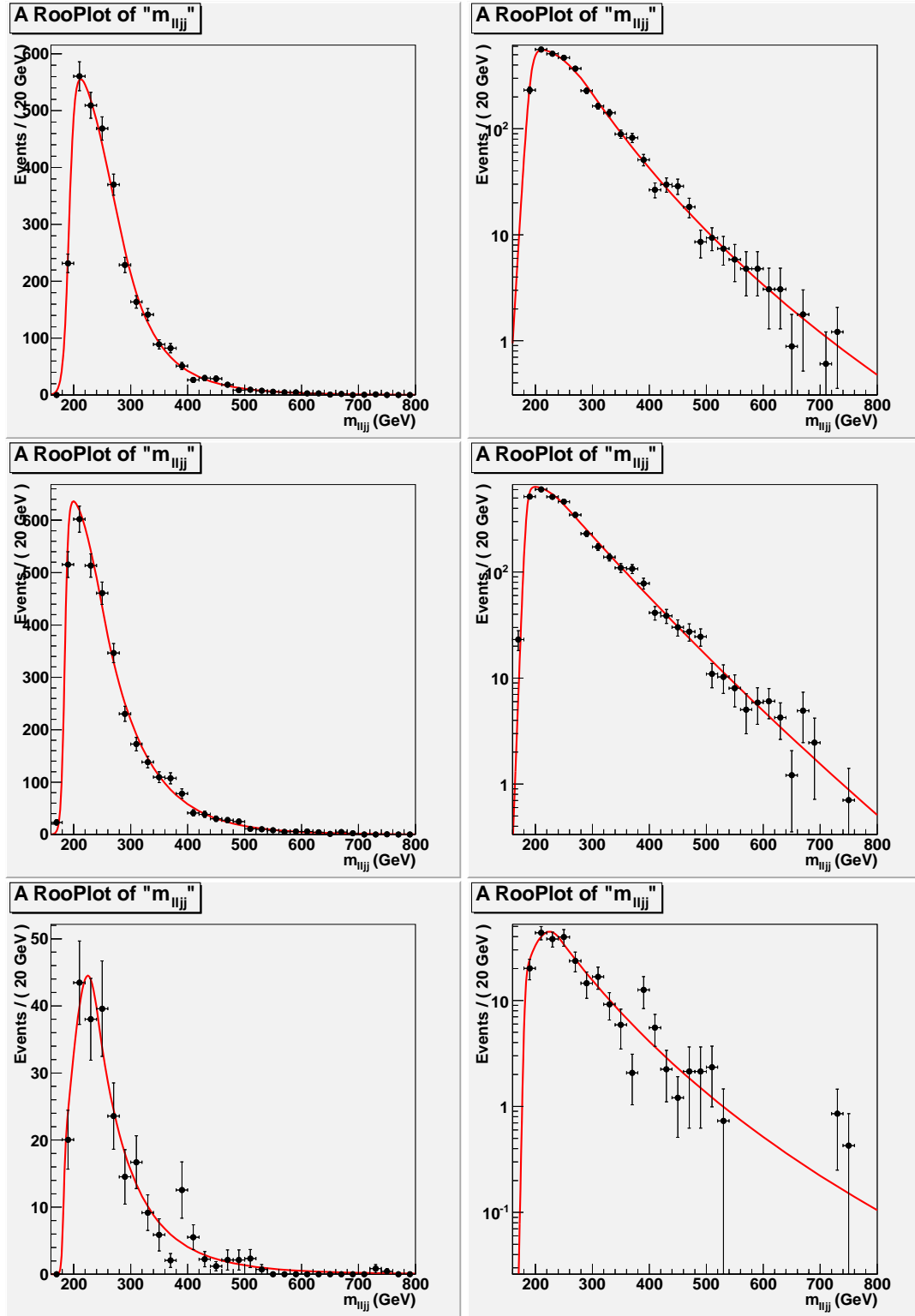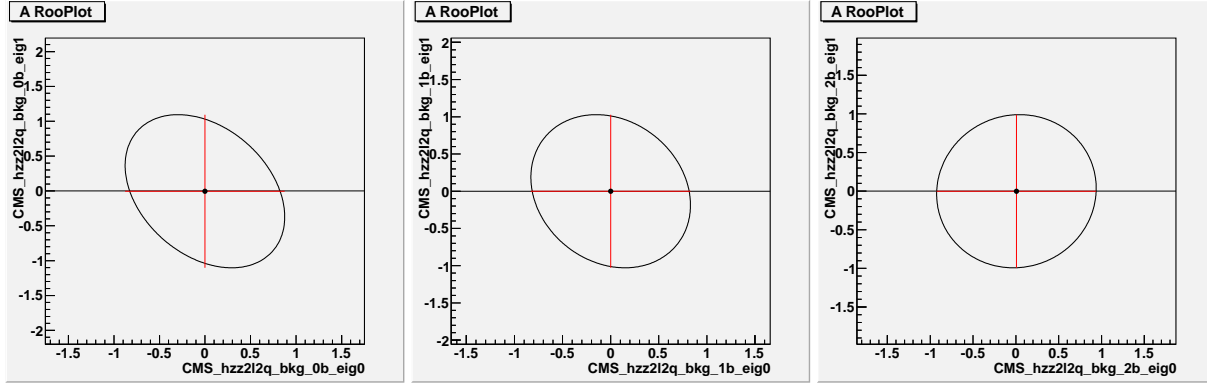

Figure 42: Likelihood contour of the parameters determined in the fit to sideband data shown in Fig. 40. The two parameters are linear combinations of the effective width of the core and position of the tail of the Crystal-Ball parameterization. Two b-tag categories are shown from left to right: 0, 1 and 2 b-tag.
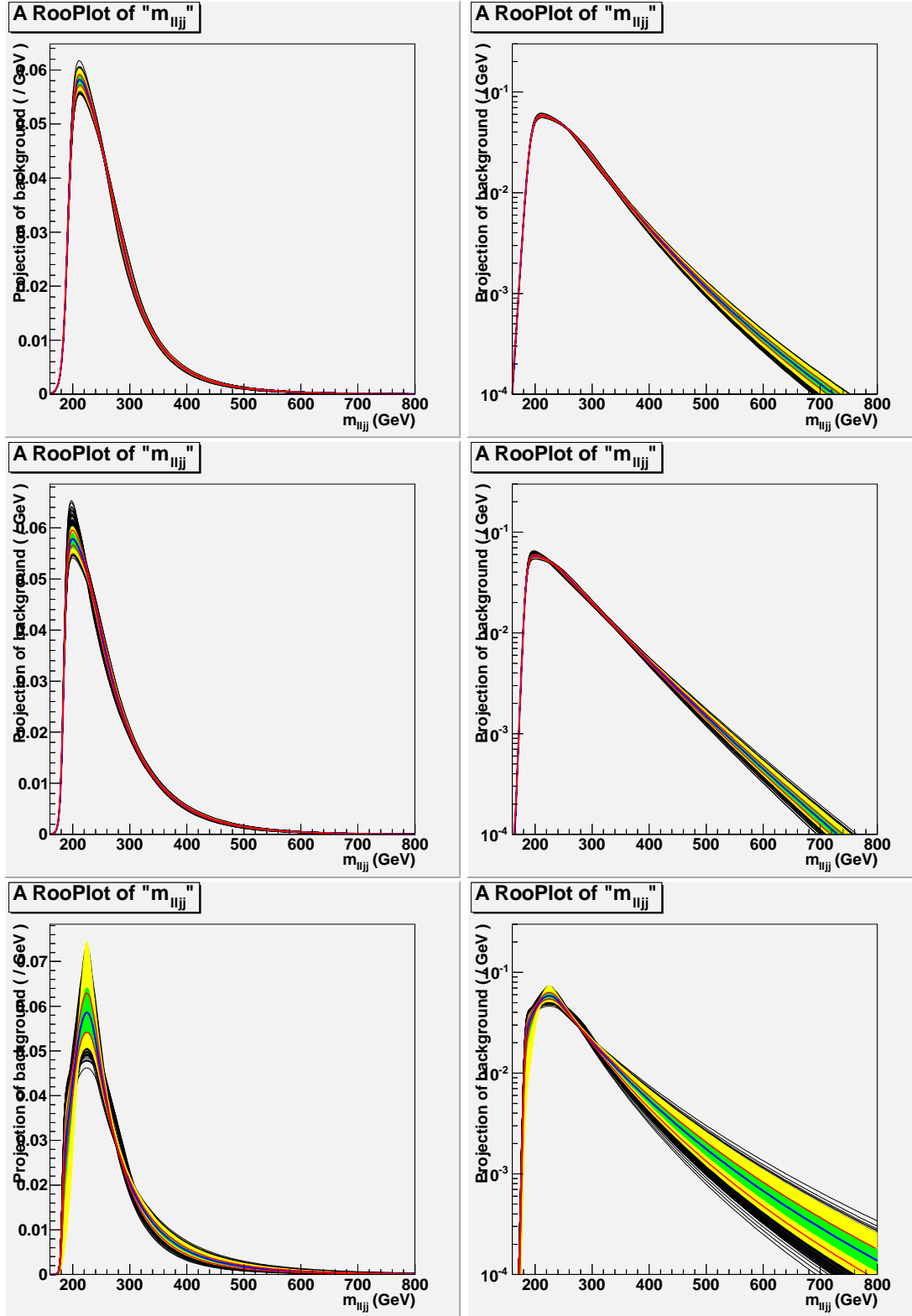
Figure 43: Fits, blue lines, to extrapolated sideband distributions, in 0 b-tag (top left), 1 b-tag (top right), and 2 b-tag (bottom) categories. The error bands show the uncertainties due to the data statistical uncertainty. The thin black lines indicate shapes derived from alternate extrapolation factors. The Red lines show the central 66% of varied extrapolations.
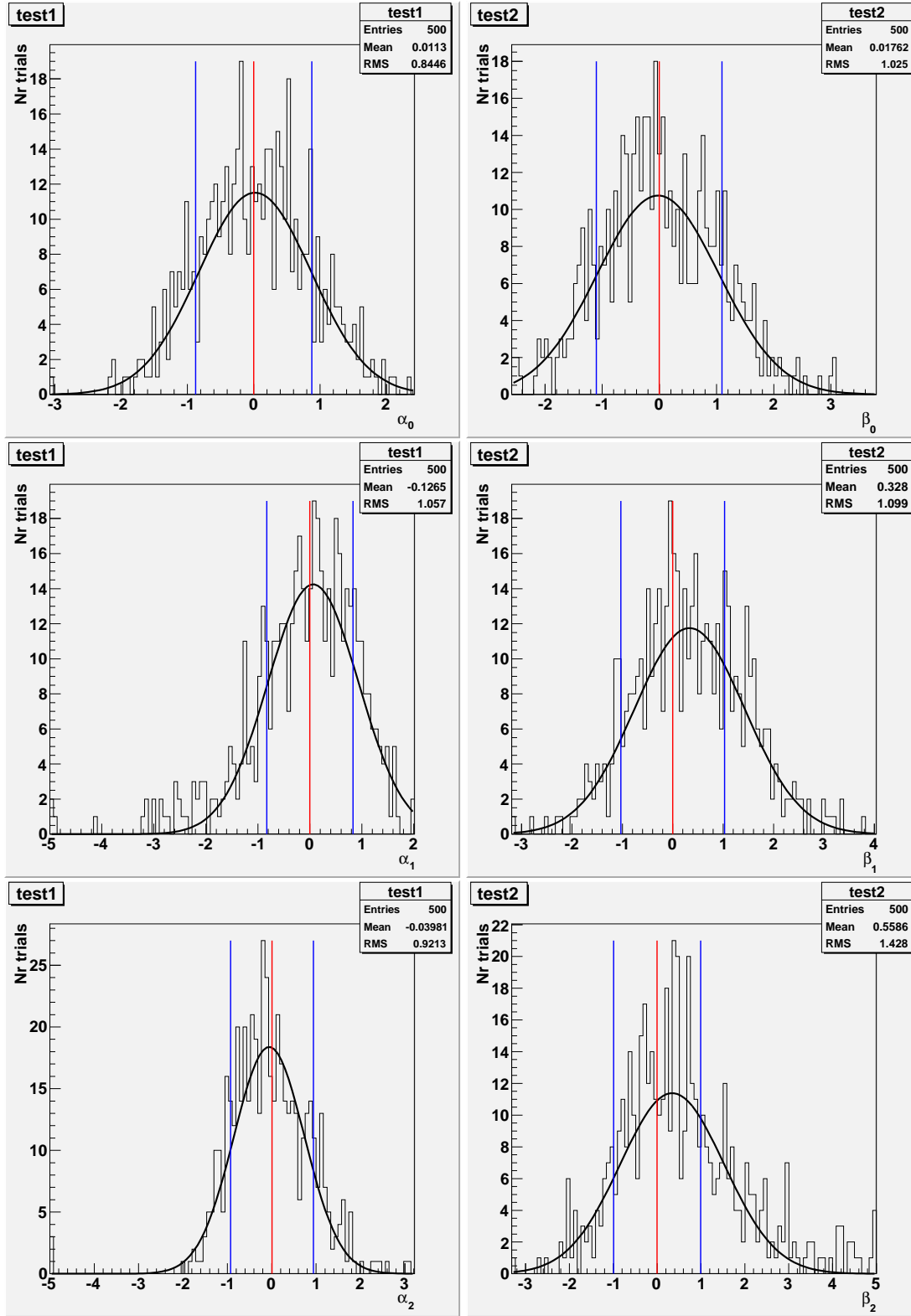
Figure 44: Background shape parameters as derived from the alternative extrapolation factors (black histogram), compared to the nominal values (red line) and uncertainty due to data statistics (blue lines).

8 Systematic Uncertainties

Uncertainty on background is considered separately and is one of the dominant effects on the exclusion limits. Systematic uncertainties on background are discussed in Section 7. Uncertainty on the signal shape parameterization arise from two sources: theory uncertainty in the BW width (Γ) parameterization, such as its mass-dependence, and experimental uncertainty in the CB resolution function. The former is taken from comparison of the mass dependent and mass-independent width parameterization used in the POWHEG and JHU generators. The latter is estimated from various sources discussed below, such as jet energy uncertainty, resolution, etc. In general signal shape uncertainties are not the dominant sources of systematics with expected signal yield of several events.

The main systematic uncertainties on signal normalization are summarized in Table 14, and are discussed in more detail below. Lepton efficiencies are evaluated with a tag-and-probe approach when one lepton from an inclusive sample of Z decays serves as a tag and efficiency for the other lepton is calculated. Effects of jet reconstruction are evaluated with variation of the jet energy and resolution within calibration uncertainties. Effects of pile-up are taken as a difference between reconstruction efficiency with pileup below and above the average expected value, otherwise distributed according to observed values in data. Requirement on the MET significance translates into about 3% inefficiency and the resulting uncertainty does not surpass this value. Uncertainty on the b-tagging has been evaluated with inclusive sample of b-jets. Uncertainty on quark-glue LD selection efficiency was evaluated with predominantly quark jets in the γ+jets sample. Uncertainties in the production mechanism affect both longitudinal momentum of the Higgs, due to PDFs, and transverse momentum of the Higgs, due to QCD initial-state radiation effects. We follow the PDF4LHC recommendation to estimate uncertainty due to PDF knowledge and calculate uncertainty on signal acceptance. We rescale the transverse momentum distribution of the Higgs using HQT as a reference and take the full change in efficiency as systematic uncertainty. Uncertainties on the Higgs cross-section are taken from the Yellow Report which includes uncertainties from QCD renormalization and factorization scales, PDFs, and α_s. These uncertainties are separated between the gluons fusion and VBF production mechanisms, but gluon fusion uncertainties dominate in the total production cross-section.

Table 14: Summary of systematic uncertainties on signal normalization. Most sources are multiplicative errors on the cross-section measurement, except for expected Higgs cross-section (which is relevant for the measurement of the ratio to SM expectation R). See text for more details.

source	0 b-tag	1 b-tag	2 b-tag	comment
muons reco		2.7%		tag-and-probe study
electrons reco		4.5%		tag-and-probe study
jet reco		1%–8%		JES uncert., JER uncert. negligible; correlated between categ
pileup		3-4%		correlated between categ
b-tagging	2-7%	3-5%	10-11%	anti-correlated between categ.
glue-tagging	4.6%	–	–	loose requirement $\Rightarrow$ expected small, studies on-going
MET	–	–	3-4%	loose requirement
production mechanism (PDF)		3%		PDF4LHC, acceptance only
production mechanism (HQT)	2%	5%	3%	only for $M_H = 200$ GeV, $< 1\%$ for $M_H = 200, 400$
production mechanism (VBF)		1%		
luminosity		6%		same for all analyses
Higgs cross-section (for R)		13–18%		detailed table from YR available

8.1 Lepton energy scale, resolution, selection, and trigger

Lepton trigger and selection is common among several $H \to ZZ$ analyses and we benefit from common study based on tag-and-probe techniques. In particular, recent studies within the framework of Ref. [5] indicate systematics of 1.0% due trigger, 0.5(3.3)% due to muon (electron) identification, 0.2(0.8)% due to muon (electron) isolation mostly independent of the mass hypothesis, 1.0(2.0)% due to muon (electron) momentum/energy scale.

8.2 Jet Energy Scale and Resolution

The main uncertainty in jet reconstruction comes from jet energy scale (JES) uncertainty, while the uncertainty on the resolution contributes a much negligible effect to the total uncertainty. Preliminary estimate with 2010 data show that jet energy uncertainty could be kept within about 4% and resolution within 10%. For more details

see Refs. [26, 27]. Since the background is extracted from sidebands in data, the systematics due to JES and jet resolution uncertainty affects only signal efficiency and potentially m_{ZZ} distribution.

Our preliminary estimates show that JES variation by $\pm 1\sigma$ changes reconstruction efficiency of a 400 GeV Higgs by about 5%. In Fig. 45 the effect of a possible JES bias ($\pm 1\sigma$) is shown on some fundamental variables. The effect on the jets transverse momentum and dijet invariant mass is sizable and it drives the bias on the acceptance while the effect is very small on the Higgs candidate invariant mass, thanks to the m_{JJ} kinematical fit. The small effect on the angular LD is due to the bias in the boosts applied to compute the angles in the Higgs and Z reference frames. The bias on the QG discriminant and b-tag categorization is negligible, as expected. Detailed study as a function of Higgs mass hypothesis is provided in Table 15.
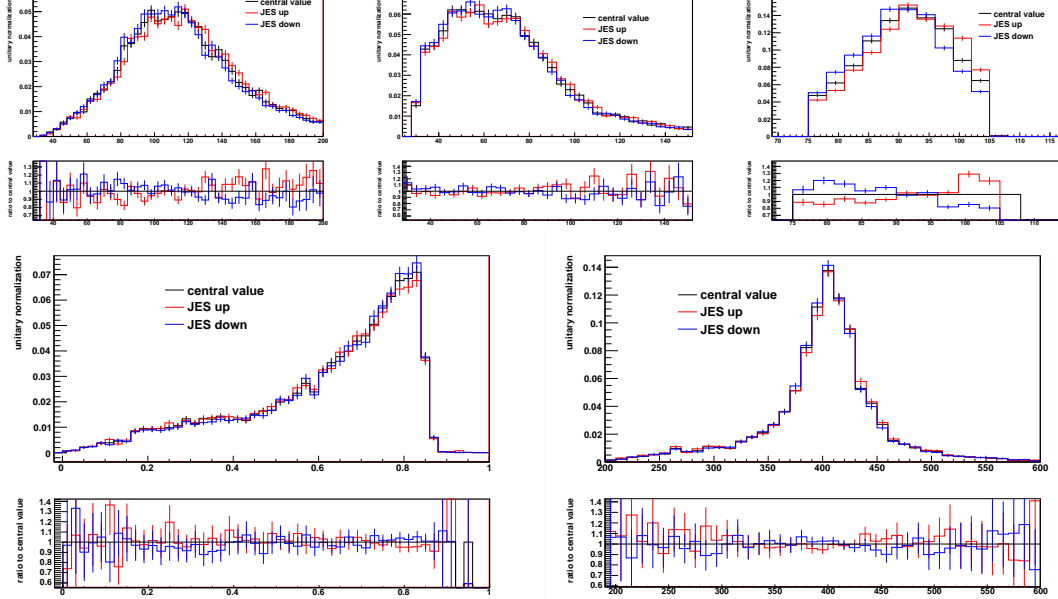

Figure 45: Distribution of leading (top, left) and subleading (top, center) jet transverse momentum, dijet invariant mass (top, right), angular LD (bottom, left) and Higgs candidate mass (bottom, right) after final selection requirements with nominal Jet Energy Scale (JES) and with JES changed by $\pm 1\sigma$.

Table 15: Cut acceptance for different jet energy scales. The uncertainty is due to the available MC statistics. Only the muon channel is considered and the acceptance is defined on the full m_H spectrum.

Sample	cuts	central value	JES $+1\sigma$	JES -1σ	systematics: $+1\sigma, -1\sigma$
signal (mh200)	preselection cuts	0.134 ± 0.002	0.141 ± 0.002	0.126 ± 0.002	
	LD and QG cut	0.058 ± 0.001	0.061 ± 0.001	0.054 ± 0.001	+5%, -7%
signal (mh300)	preselection cuts	0.282 ± 0.002	0.286 ± 0.002	0.275 ± 0.002	
	LD and QG cut	0.195 ± 0.002	0.198 ± 0.002	0.192 ± 0.002	+1%, -2%
signal (mh400)	preselection cuts	0.381 ± 0.002	0.380 ± 0.002	0.378 ± 0.002	
	LD and QG cut	0.266 ± 0.002	0.264 ± 0.002	0.266 ± 0.002	-1%, +0%
signal (mh500)	preselection cuts	0.417 ± 0.003	0.410 ± 0.003	0.417 ± 0.003	
	LD and QG cut	0.276 ± 0.002	0.269 ± 0.002	0.280 ± 0.002	-2%, +1%
signal (mh600)	preselection cuts	0.416 ± 0.003	0.408 ± 0.003	0.419 ± 0.003	
	LD and QG cut	0.255 ± 0.002	0.248 ± 0.002	0.260 ± 0.002	-3%, +2%

A bias on the JES can also affect the signal shape. The Higgs mass shape is defined in Sec. 9. In Tab. 16 the values of the Higgs shape parameters for different JES conditions are listed for various Higgs masses. In Fig. 46 the Higgs mass distribution and its fit are shown for different JES conditions.

The effect of the jet resolution uncertainty on the signal was evaluated by applying an additional smearing to the jets and comparing to the same sample without additional smearing. As the background is evaluated directly from the data it is not expected that the jet energy resolution will have a significant effect. The additional smearing applied to the jets is the nominal jet resolution at the given p_T and η multiplied by the difference observed between

Table 16: Value of the parameters for the signal higgs mass fit for different JES conditions. The last column is an estimation of the statistical error of the fit.

Sample	parameter	central value	JES $+1\sigma$	JES -1σ	fit error
signal (mh200)	CB mean	0.7	0.5	0.6	0.2
	CB sigma	3.0	3.0	3.0	0.4
	CB α_1	0.9	1.0	0.9	0.2
	CB n_1	2.7	1.8	3.0	0.5
	CB α_2	1.1	1.0	1.1	0.1
	CB n_2	1.2	1.3	1.2	0.1
signal (mh300)	CB mean	4.2	4.5	4.0	0.3
	CB sigma	6.6	7.0	7.2	0.7
	CB α_1	1.3	1.4	1.5	0.2
	CB n_1	1.4	1.4	1.3	0.2
	CB α_2	1.0	1.0	1.2	0.1
	CB n_2	2.4	2.5	2.0	0.3
signal (mh400)	CB mean	15.1	15.9	14.5	0.5
	CB sigma	11	12	11	1
	CB α_1	1.8	1.8	1.8	0.2
	CB n_1	0.9	0.8	0.9	0.2
	CB α_2	1.4	1.3	1.4	0.2
	CB n_2	2.2	2.3	2.1	0.4
signal (mh500)	CB mean	17	18	16	1
	CB sigma	15	15	14	3
	CB α_1	2.3	2.4	2.2	0.4
	CB n_1	0.3	0.3	0.5	0.3
	CB α_2	1.8	1.6	1.8	0.4
	CB n_2	1.2	1.4	1.2	0.5
signal (mh600)	CB mean	20	22	20	1
	CB sigma	25	23	26	3
	CB α_1	2.3	2.3	2.2	0.2
	CB n_1	0.1	0.1	0.2	0.2
	CB α_2	5	5	5	6
	CB n_2	10	9	8	8

resolution in data and simulation as given in [27] (differential in η). The applied factor is typically quite small, in the low percent to sub-percent range, due to the good data-MC agreement. The effect on the selection efficiency is very small ($< 1\%$) due to several effects: For all but the lowest mass working points, jet energies are high enough above the threshold of 30 GeV that the additional smearing has little effect on the selection. Distribution of m_{JJ} falls very softly, so that the number of events migrating into the acceptance roughly compensates the number of events migrating into it. The LD variable is indirectly affected by the smearing via boosts into the H and Z center of mass systems. However, this is counteracted by the kinematic fit. Similarly, the reconstructed Higgs line shape does not significantly broaden as shown in Fig. 47.

8.3 Pile-up

The PU is corrected as reported in Section 3.4. Since the background is extracted from sidebands in data, the main systematics due to PU residual effects after corrections can be the effect on the signal efficiency and m_{ZZ} distribution.

The MC samples are re-weighted to match the PU distribution measured in data and the main source of systematics may come from a mis-modeling of the PU in MC with respect to data (Pythia Z2 tune is used for the PU simulation) or from the uncertainty on the measurement of the amount of PU in data.

As systematics we quote in Table 17 the difference between the average efficiency and the efficiencies we get with more or less PU events than the mode of the data (7 PU events). This procedure is quite arbitrary but surely conservative.

To find a more motivated estimate of the systematics, the two sources of uncertainty can be separated:
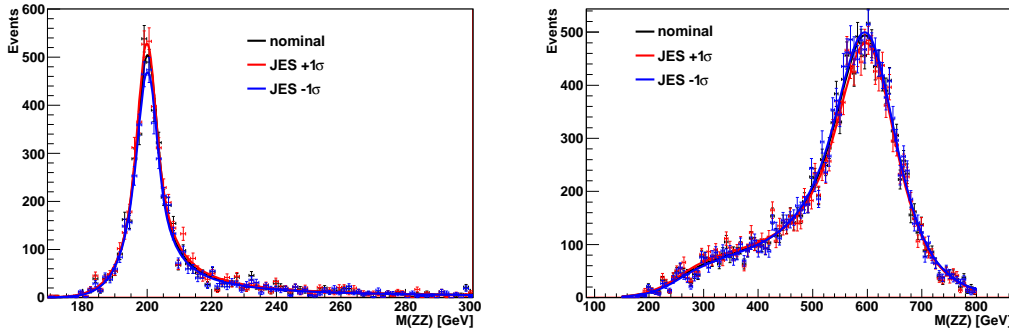
Figure 46: Reconstructed Higgs mass distributuions and its fit in different JES conditions for 200 GeV (left) and 600 GeV (right) Higgs mass hypothesis, integrated over all b-tag categories.
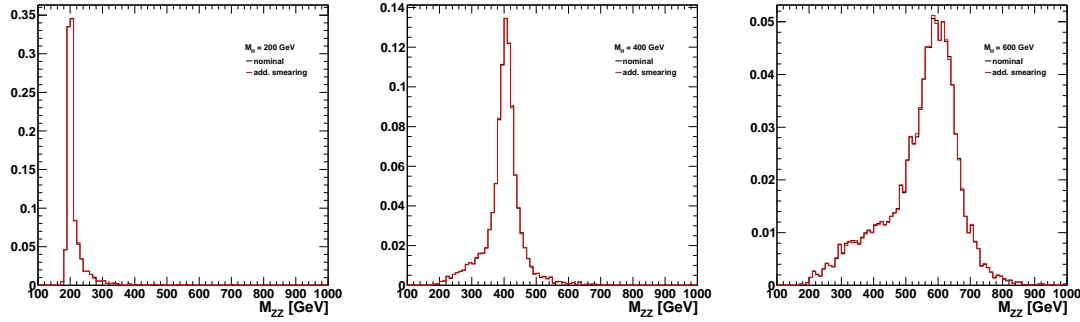

Figure 47: Reconstructed Higgs mass distributuions with (red) and without (black) additional jet-p_t smearing for several masses, integrated over all b-tag categories.

- The expected number of pileup events in a given collision is affected linearly by the luminosity uncertainty.

- The events overlayd in the simulation originate from a minimum bias simualtion and may not perfectly mirror the topology of overlaying events in the data.

The first point was studied by shifting the N_{PU} distribution extracted from data by the luminosity uncertainty. This leads to a change of $\sim 0.5\%$ in signal acceptance, approximately independent of higgs mass and b-tag category. The second point is much harder to address as the quality of the minimum bias simulation used to emulate pileup cannot be easily quantified. We use the distribution of ρ as defined in the Fastjet algorithm (an estimation of the energy spread around in the detector due to PU and underlying event) as a general indicator of the quality of the simulation. We compute the change in efficiency when reweigting this distribution in the signal simulation to the spectrum observed in data. Note, that the signal is dominated by quark jets, while the background dominated data contains mostly gluon jets, which are more likely to produce soft unclustered hadrons. Thus the reweighting may not be completely accurate. The observed effect of this reweighting is $< 1\%$. Until these studies on the PU event topology have been further consolidated, we use the conservative estimate discussed above.

To show which distributions are affected by the PU and how, we compare no-PU and PU corrected samples in signal MC. The distributions of the angular likelihood discriminant and of the QG discriminant are shown in Fig. 48 in different PU conditions for all the Higgs candidates, passing the preselection cuts listed in Sec. 3, in a signal MC sample with 400 GeV Higgs mass. The distributions of the Higgs mass and the b-tag categorization are shown in Fig. 49 for the same sample after all the cuts have been applied and the best Higgs candidate has been

Table 17: Summary of efficiency differences between low/high PU subsamples and the average.

M_H	$M_H = 200$ GeV			$M_H = 400$ GeV			$M_H = 600$ GeV		
	0 b-tag	1 b-tag	2 b-tag	0 b-tag	1 b-tag	2 b-tag	0 b-tag	1 b-tag	2 b-tag
Δ_{eff}	6.5%	1.7%	3.2%	1.6%	$< 1\%$	$< 1\%$	3.7%	3%	2.2%
total	3.7%			1%			3.1%		

chosen. The PU effect on the LD distribution and the Higgs mass is negligible. Moreover the PU may impact the b-tag performance moving events from one b-tag category to another.
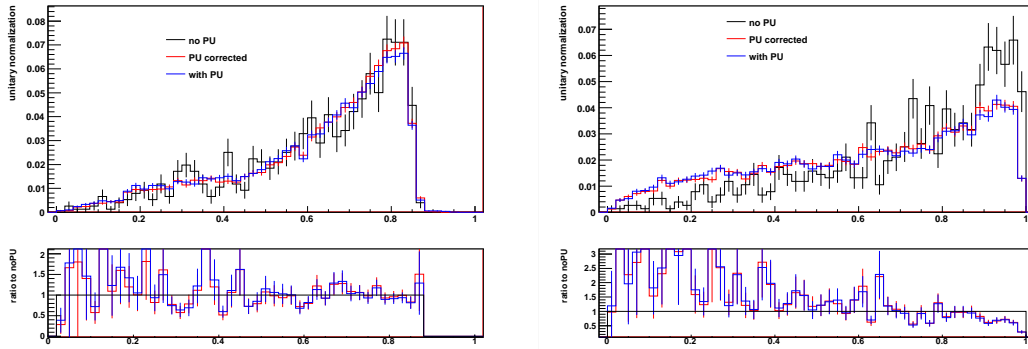

Figure 48: Angular (left) and QG (right) likelihood discriminant in signal with Higgs mass of 400 GeV for different PU conditions. *The QG plot has not been updated yet to the latest robust implementation of the QG LD, but the study includes the latest implementation*
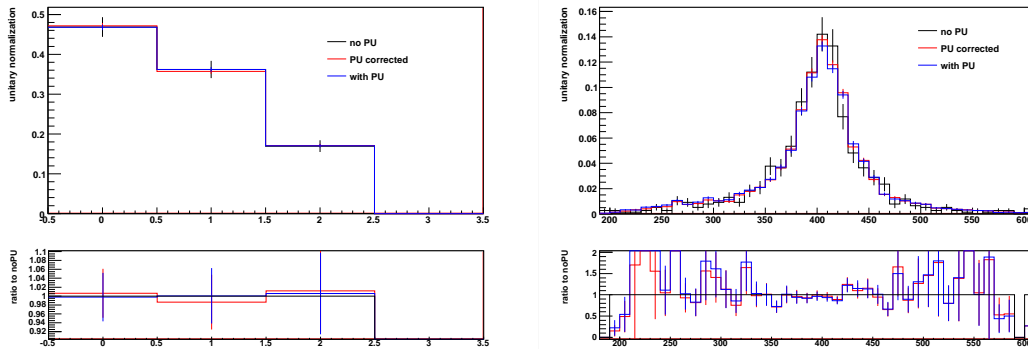

Figure 49: Categories of b-tags and reconstructed Higgs candidate mass in signal with Higgs mass of 400 GeV for different PU conditions.

While the above method properly estimates the residual effects of pileup after corrections, it is overly conservative as the residual effects of the pileup are at least partly accounted for in the simulation.

8.4 Heavy quark flavor tagging uncertainty

For more specific b-tag studies we refer to Ref. [5]. Preliminary estimates show uncertainties $\sim 20\%$ in 2 b-tag category and $\sim 5\%$ in 0 and 1 b-tag categories.

8.5 Quark-glue tagging

The quark-gluon discriminant is founded on general assumptions on the structure and couplings of the QCD Lagrangian, yet does rely on the modeling of hadronization done in the generator. Mismodelings of (light) quark hadronization, which affect the chosen observables (jet multiplicities and transverse momentum distributions) would alter the predicted signal efficiency of the selection. It is therefore important to verify that the performance of the discriminant on quark jets is similar to expectations.

A control sample is identified by photon+jet events, in which the leading jet originates from light quarks in more than 90% of the cases. In order to contrast the dominant background, constituted by QCD dijet events in which one of the two jets has fragmented mainly into a particle capable of creating a large energy deposit in ECAL (such as a neutral pion), a stringent photon identification is needed. We make use of the photon identification described in Ref. [25]. In order to ensure the absence of jets originated from b-quarks, events in which the leading jet has a positive loose TCHE b-tag have been vetoed. The expected photon+jet purity of this selection is of the order of 90% at high transverse momenta, and significantly lower at low transverse momenta (reaching $\sim 50\%$ at 20 GeV). It must be noted that a background infiltration does dilute the quark component, but not dramatically, as about 40% of jets in QCD events are originated from quark partons.
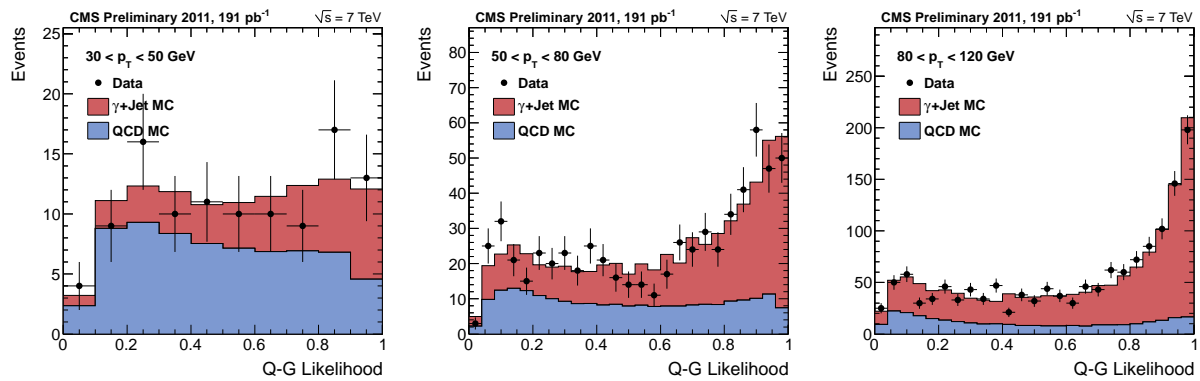
47

Figure 50: Distributions of the quark-gluon discriminant in photon+jet events in three transverse momentum ranges. The Monte Carlo distributions are normalized to the shape of the data.
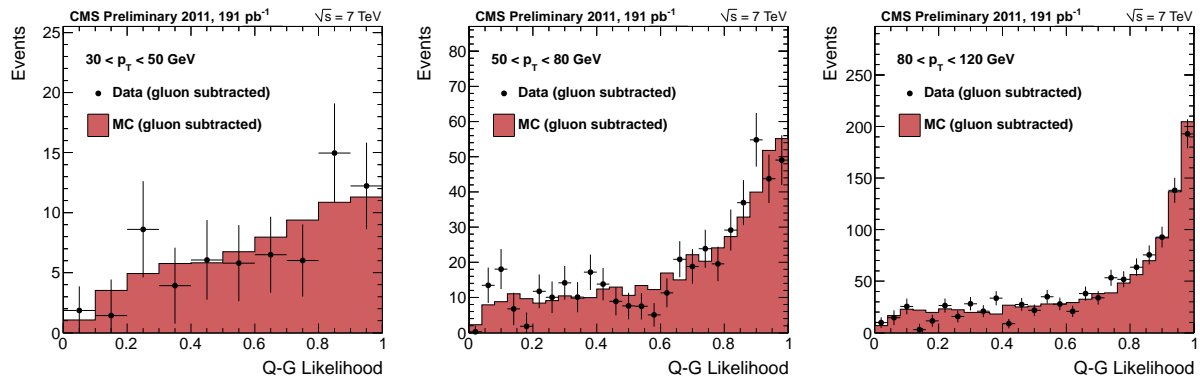

Figure 51: Expected distributions of the quark-gluon discriminant for quark jets in three transverse momentum ranges. The gluon contribution has been subtracted by accessing the MC truth. The Monte Carlo distributions are normalized to the shape of the data.

The shape of the quark-glue discriminant obtained on photon+jet events, in three different transverse momentum bins, is shown in Figures 50. The data is compared to the simulation, and the latter is normalized to the signal shape. The available amount of data decreases at lower transverse momenta because of the presence of high prescales in the photon triggers. The observed shape of the discriminant seems compatible with expectations, within the statistical precision granted by the analyzed data.

We are interested in studying a possible effect on quark efficiency, so the gluon contribution has to be subtracted. The latter is isolated in the simulation by applying a matching at MC truth level between jets and partons. Jets successfully matched to gluons are hence subtracted both from data and MC. The gluon-subtracted distributions are shown in Figures 51.

In order to evaluate the effect on signal efficiency, we have to simulate the effect of cutting on the product of two jet's likelihood, with similar kinematic properties as those expected in the case of a heavy Higgs decay. It is not possible to isolate a sample of photon+jet events with

Table 18: Efficiencies of requiring the quark-gluon discriminant to be greater than 0.2 on light quark jets, in data and MC, in three transverse momentum bins. The error on the Monte Carlo efficiency if negligible if compared to the error on data.

Jet p_T [GeV]	MC efficiency	Data efficiency
30-50	93.2%	$(95.1 \pm 3.3)\%$
50-80	91.3%	$(91.1 \pm 1.6)\%$
80-120	91.8%	$(94.0 \pm 0.8)\%$

It is not possible to isolate a sample of photon+jet events with two highly quark-enriched jets with similar kinematica properties as the ones expected from the decay of a heavy Higgs boson. We will therefore have to simulate the effect of the decay kinematics, and will proceed as follows. We choose a threshold of 0.2 on the single jet Q-G

likelihood distribution, as it is expected to provide an efficiency ϵ such that $\epsilon^2 \approx 85\%$, which is the expected signal efficiency of the cut applied in the analysis. The efficiency of this cut on quark jets is measured in data and MC by applying the requirement on the gluon-subtracted distributions shown in Figures 51, and is reported in Table 18.

Table 19: Efficiencies of requiring the quark-gluon discriminant to be greater than 0.2 on light quark jets, in data and MC, in three transverse momentum bins. The error on the Monte Carlo efficiency if negligible if compared to the error on data.

	30-50 GeV	50-80 GeV	80-120 GeV
Leading Jet	11%	64%	22%
Subleading Jet	68%	32%	2.3%

As no significant deviation is observed between the data and the MC prediction, the uncertainty will originate from the statistical uncertainty of the comparisons. Therefore, we expect the lowest transverse momentum bin (30-50 GeV) to play the driving role. The kinematic properties of the jets in signal will depend on the mass of the decaying Higgs boson, being on average harder as the mass increases. In order to provide a conservative estimate of this systematic uncertainty, we have considered the case of a relatively light mass Higgs boson, 250 GeV, where the relative weight of the lowest p_T bin is inflated. In the decay of a 250 GeV Higgs boson, the jets are expected to populate the three transverse momentum bins as reported in Table 19. We estimate the uncertainty U on the single jet as the average of the statistical error in the three transverse momentum bins, weighted on the expected fractions:

$$\text{U(jet)} = \sum x_i \Delta_i$$

where $i = 1, 2, 3$ are the three transverse momentum bins, x_i is the fraction of jets which fall in the given bin, and Δ_i is the statistical uncertainty of that bin. We find:

$$\text{U(lead)} = 22\% \cdot \left(\frac{0.8\%}{94.0\%} \right) + 64\% \cdot \left(\frac{1.6\%}{91.1\%} \right) + 11\% \cdot \left(\frac{3.3\%}{95.1\%} \right) = 1.7\%$$

$$\text{U(sublead)} = 2.3\% \cdot \left(\frac{0.8\%}{94.0\%} \right) + 32\% \cdot \left(\frac{1.6\%}{91.1\%} \right) + 68\% \cdot \left(\frac{3.3\%}{95.1\%} \right) = 3.0\%$$

We then take the product of the uncertainties of the two jets as an estimate of the uncertainty on the cut of the product of the two likelihoods, and therefore find a total systematic uncertainty of $\text{U(prod)} = 4.6\%$.

8.6 MET uncertainty

MET affects directly only the 2 b-tag category. The dominant effects are from the knowledge of the rest of the event, such as jet energy reconstruction and pileup. Therefore, both of the above subsections cover MET uncertainty to a large extent. The uncertainty is computed following the method also used in the low mass analysis (see section 10.8.1). Requirement on the MET significance translates into about 3% inefficiency and the resulting uncertainty does not surpass this value, as shown in fugure 52.

8.7 Production mechanism

The expected kinematics of the Higgs production is subject to uncertainties due to limited knowledge of the underlying parton distribution functions (PDFs) as well as the shortcomings in the theoretical prediction (missing higher orders in the perturbation series). These uncertainties are propagated to an uncertainty on the selection acceptance and efficiency. Their additional effect on the Higgs production cross section is discussed in a separate section below.

The PDF uncertainties is evaluated according to the PDF4LHC recommendations, by evaluating the selection efficiency for the PDF sets CT10 [29], MSTW2008NLO [30] and NNPDF2.1 [31] and their error sets. Table 8.7 summarizes the resulting acceptance uncertainties. The envelope of the various PDF sets is used as the total uncertainty, as recommended and amounts to 2-4% without strong dependence on Higgs mass or b-tag category.

The uncertainty from the matrix element is evaluated with the help of the HQT program, which includes NLL effects and exhibits a modified Higgs p_T spectrum, especially for low Higgs masses. The nominal POWHEG sample is re-weighted as a function of Higgs p_T to match the HQT spectrum and the selection efficiency evaluated in each case. Figure 53 shows the generated Higgs p_T spectra from POWHEG and HQT for three Higgs masses.
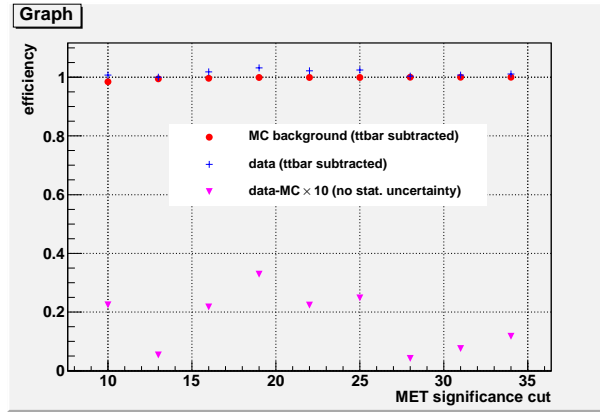
Figure 52: Efficiency in data and Monte Carlo (after $t\bar{t}$ subtraction) for various MET significance cuts in the 2 btag category after the preselection cuts. The difference between data and Monte Carlo efficiencies (magnified by 10) is also shown.

The effect of this re-weighting is strongest for the lowest Higgs mass studied (200 GeV): the efficiency drops by 3% as the softer Higgs p_T spectrum from HQT leads to slightly softer leptons and jets on average. The loss of efficiency depends only weakly on the b-tag category (0-tag: -2%, 1-tag: -5%, 2-tag: -3%). At higher Higgs masses (400 and 600 GeV) the difference in efficiency is less than one percent for all b-tag categories. The trend of decreasing uncertainties at higher Higgs masses is caused by two separate effects: Firstly, POWHEG and HQT show better agreement at higher Higgs masses. Secondly, the decay energy of the Higgs dominates over the Higgs p_T in determining the kinematics of the decay products for high Higgs masses.
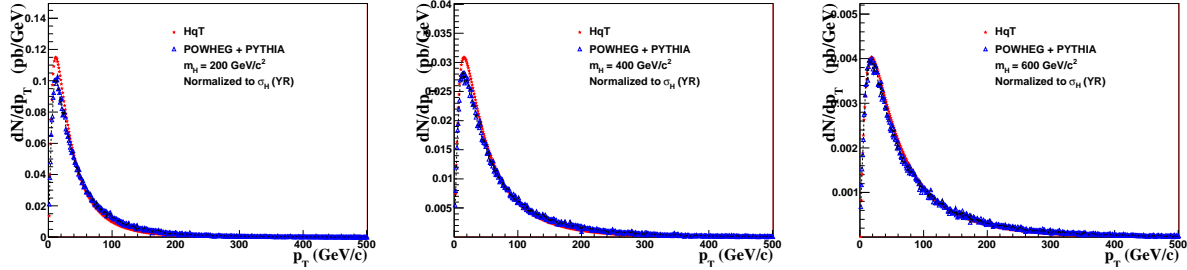

Figure 53: Generated Higgs p_T distributions from POWHEG (red) and HQT (blue) several masses.

We additionally estimate the uncertainty that originates from the fact that the analysis has been tuned using gluon fusion based simulation while a real signal contains a mixture of events produced by gluon fusion and VBF. Here we compute the difference in signal acceptance between the two production mechinisms in Monte Carlo and multiply this difference with the expected fraction of VBF production, leading to a global uncertainty on the

Table 20: Summary of systematic uncertainties on the signal acceptance following PDF4LHC recommendations.

PDF	$M_H = 200$ GeV			$M_H = 400$ GeV			$M_H = 600$ GeV		
	0 b-tag	1 b-tag	2 b-tag	0 b-tag	1 b-tag	2 b-tag	0 b-tag	1 b-tag	2 b-tag
CT10	+0.7% −3.7%	+0.9% −3.7%	+1.3% −4.6%	+0.8% −3.5%	+0.5% −3.3%	+0.9% −4.0%	+0.4% −2.6%	+0.4% −3.4%	+0.7% −4.3%
all categories	+1.0% −3.9%			+0.7% −3.4%			+0.6% −4.1%		
MSTW2008NLO	−0.6% −0.6%	0.5% −0.8%	0.9% −0.8%	+0.5% −0.5%	+0.4% −0.3%	+0.8% −0.3%	−0.30% −0.0%	+0.3% −0.2%	+0.5% −0.3%
all categories	0.6% −0.8%			+0.5% −0.4%			+0.4% −0.3%		
NNPDF2.1	+1.8% +0.3%	+1.7% +0.1%	+2.2% +0.0%	+1.4% +0.0%	+1.4% +0.3%	+1.5% +0.1%	+0.7% +0.1%	+1.1% +0.3%	+1.6% +0.3%
all categories	+1.8% +0.1%			+1.3% +0.2%			+1.4% %+0.3		
Total	+1.8% −3.7%	+1.7% −3.7%	+2.2% −4.5%	+2.3% −3.5%	+1.4% −3.3%	+1.5% −3.9%	+0.7% −2.6%	+1.1% −3.4%	+1.6% −4.3%
all categories	+1.8% −3.9%			+1.3% −3.4%			+1.4% −4.1%		

50

production cross section.

Table 21: Summary of systematic uncertainties due the VBF.

M_H	$M_H = 200$ GeV			$M_H = 400$ GeV			$M_H = 600$ GeV		
	0 b-tag	1 b-tag	2 b-tag	0 b-tag	1 b-tag	2 b-tag	0 b-tag	1 b-tag	2 b-tag
Δ_{eff}	20%	15%	6%	-2%	4%	4%	-8%	6%	-0.3%
total	7%			11%			13%		
uncertainty	2.4%	1.8%	0.7%	-0.16 %	0.3 %	0.3 %	-1.4 %	1 %	0%
total	2%			0.1%			-1.4%		

8.8 Luminosity uncertainty

The latest recommendation is the uncertainty on LHC luminosity of 6%.

8.9 Higgs cross-section and branching fractions

The Higgs production cross-section uncertainty depends on production mechanism, either gluon fusion or weak boson fusion (WBF). However, since the gluon fusion mechanism dominates, it drives the total uncertainty. We use gg and WBF errors separately and for each mass point according to Yellow Report prescription. The total weighted error is in the range 13.4–18.0%. We note that this uncertainty is relevant only for the measurement of the ratio to SM expectation R, while it does not affect the absolute cross-section measurement.

9 Statistical Interpretation of Results

We follow the strategy of the CMS collaboration to search for the Higgs boson at 173 m_H mass points, as illustrated in Fig. 54. However, since exclusion power is limited below 130 GeV and between 165 and 200 GeV, we provide analyses at 43 m_H mass points between 130 GeV and 164 GeV, and at 73 m_H mass points between 200 GeV and 600 GeV. Parameterization of signal is extrapolated to all mass points from the several signal MC samples available and listed in Section 2.1.
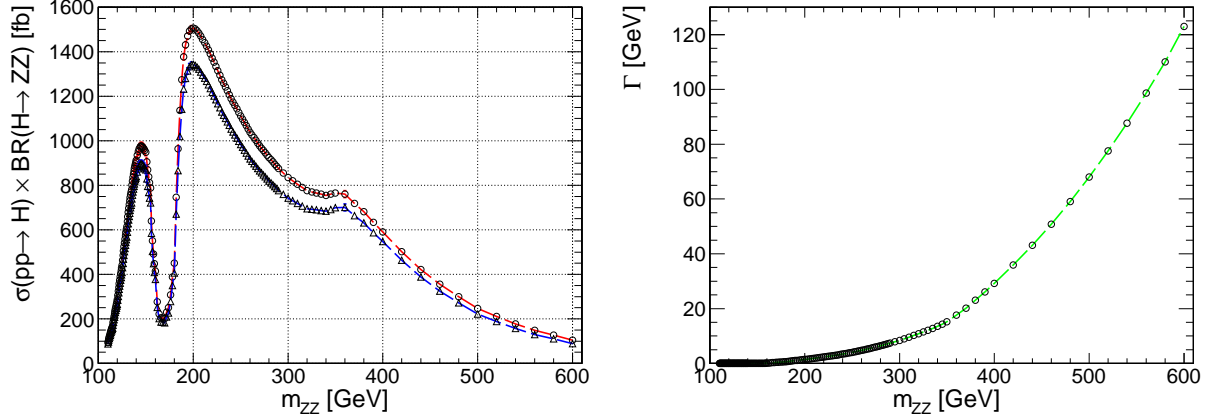

Figure 54: Left: expected Higgs production cross-section (total and gg only) multiplied by the branching fraction of $H \to ZZ$ as a function of Higgs mass. Right: expected Higgs boson width Γ as a function of its mass. Values are shown for 173 mass points for which exclusion limits will be calculated.

The analysis is split into two sub-ranges: the low-mass m_{ZZ} range between 125 GeV and 170 GeV, and the high-mass m_{ZZ} range between 183 GeV and 800 GeV. Below we discuss analysis specific to the high-mass range $183 < m_{ZZ} < 800$ GeV, where details of the low-mass range analysis are given in Section 10.

The same m_{ZZ} distribution of events is examined for each of the hypotheses of Higgs mass. For each mass hypothesis, we perform a simultaneous likelihood fit of the six m_{ZZ} distributions (three b-tag categories and two lepton flavors) using the statistical approaches discussed in Ref. [34]. As the prime method for reporting limits we use the $\mathrm{CL_s}$ modified frequentist technique [35]. As a complementary method to the frequentist paradigm, we use the Bayesian approach. In this method, the Bayes theorem [36] is invoked to assign a degree of belief to the Higgs hypothesis by calculating the posterior "probability density function" on the signal strength. All results are validated by using two independent sets of software tools, RooStats package [37] and L&S [38].

The m_{ZZ} distribution of background events is illustrated in Fig. 56 in three b-tag categories using MC simulation. Detailed discussion of application of the background determination technique to data is given in Section 7. The background distribution is parameterized with an empirical Crystal-Ball shape distribution multiplied by the Fermi function to describe threshold effects. The signal distribution varies depending on Higgs mass hypothesis and several examples are shown in Fig. 57. The signal shape is parameterized as the sum of two distributions: A double Crystal-Ball function (i.e. a Gausian core with powerlaw tails on both sides) is fit to MC events in which the two hadronic legs of the reconstructed candidate match the generate quarks from the Higgs decay. A triangel smeared with a Crystall-Ball function is used to describe the remaining unmatched events. The Signal reconstruction efficiency is parameterized as a function of mass and are extrapolated to all 73 mass points. An example of efficiency parameterization is shown in Fig. 55. The parameters for the signal shape at these 73 mass points, is obtained by linear interpolation between the fitresults to 17 simulated samples, whith roughly evenly spaced Higgs mass hypothesis.

Based on expected yields presented in Tables 9, 10, 11, and 12 and expected shapes shown in Fig. 57, we perform toy MC experiments where expected background samples are generated and a likelihood fit is performed. Expected and observed exclusion limits are presented in Table 22, where cut-and-count approach is compared to the shape analysis. We observe systematically better limits with the likelihood fit approach compared to cut-and-count. For one mass point we show more detailed calculations of the upper limits in Table 23,
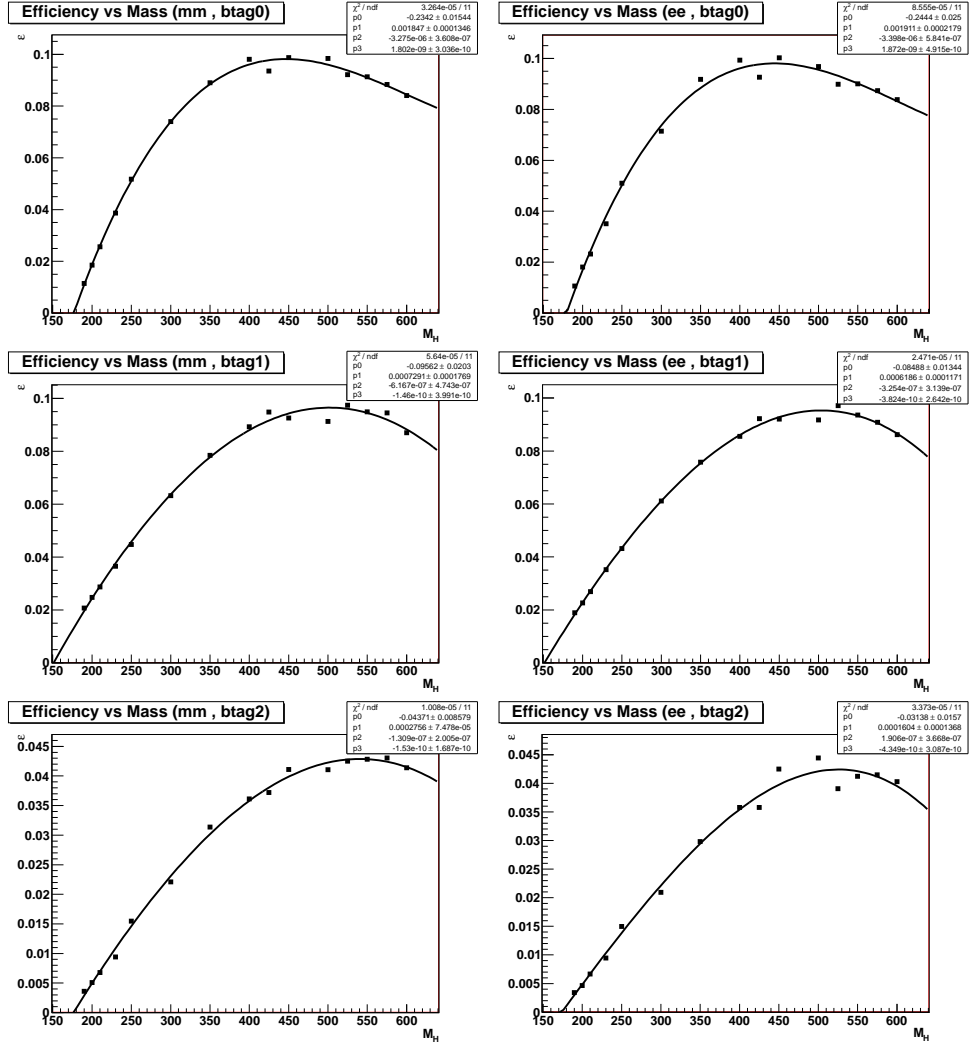
Figure 55: Parameterization of signal efficiency as a function of Higgs mass hypothesis in 0 b-tag (top), 1 b-tag (middle), 2 b-tag (bottom) categories and in the muon (left) and electron (right) channels.

Table 22: Projected and observed upper limits on the cross-section normalized to the SM Higgs cross-section for a cut and count experiment and a likelihood-based UL using the m_{ZZ} invariant mass shape.

Higgs mass	UL (c&c) expected	UL observed (c&c)	UL expected (shape)	UL observed (shape)
250	4.02	4.04	3.74	4.05
300	3.08	2.61	2.66	2.96
350	2.14	1.99	1.77	1.53
400	2.16	2.89	1.94	1.96
460	2.90	2.36	2.72	2.35
500	3.67	7.20	3.50	3.40
560	5.80	6.10	5.54	4.80
600	7.99	11.6	7.32	5.95

Table 23: The number of expected signal and background events, observed number of events, and upper limit on the ratio to SM expectation in analysis of a 400 GeV Higgs hypothesis. Results are separated between three btag categories and are combined. No systematics is included in the cut and count calculation for simplicity (this changes the final result from 2.89 to 2.58). The last column shows results with the shape analysis (including systematics).

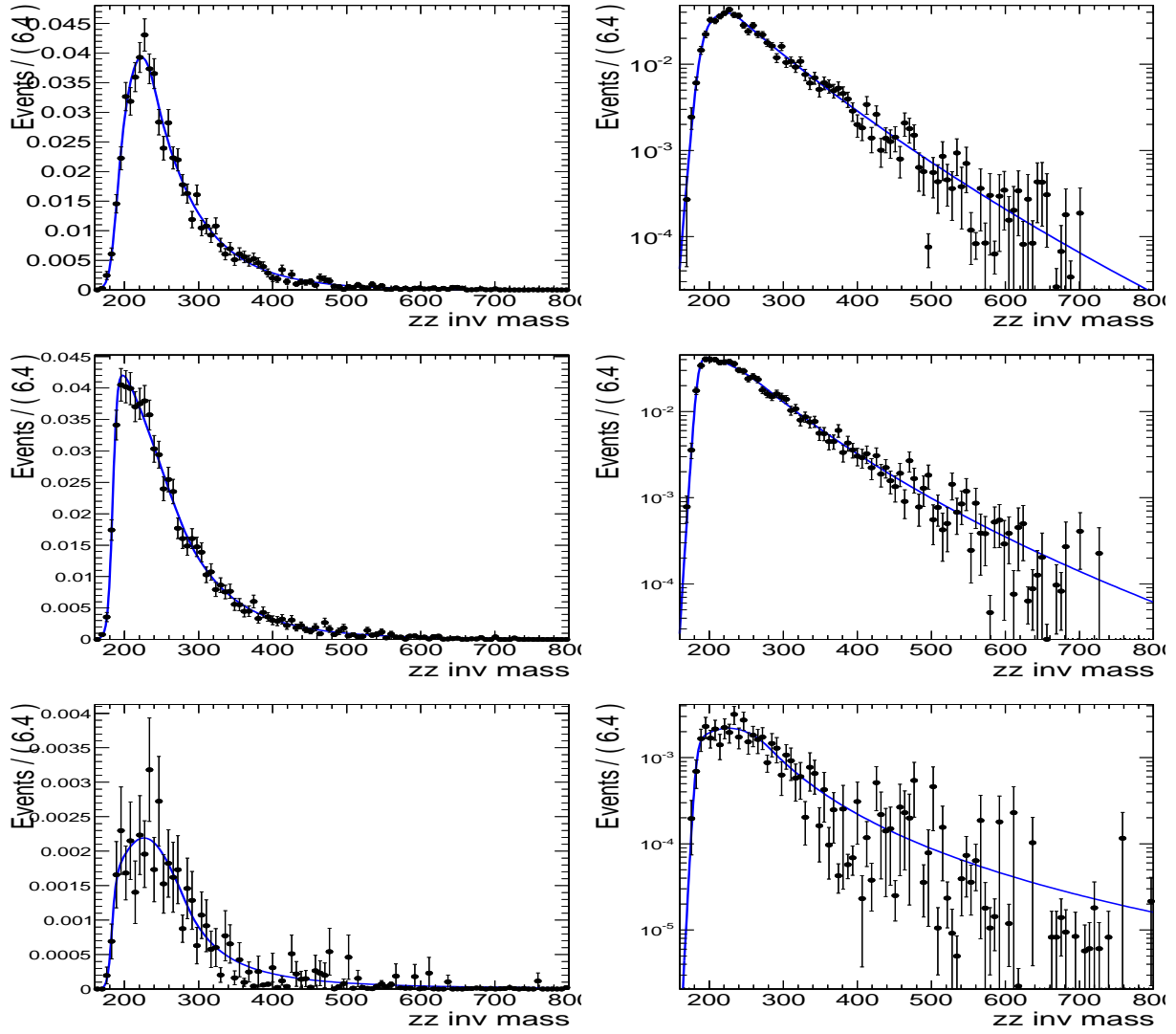| categ.	exp sig	exp bkg	obs	obs UL	obs shapes
0btag	3.4	32.7	33	4.18	3.1
1btag	2.8	40.7	46	6.58	3.9
2btag	1.3	1.9	2	3.70	4.3
combined				2.58	1.96

Figure 56: Distribution of m_{ZZ} invariant mass for background simulation and probability parameterization in 0 b-tag (top), 1 b-tag (middle), and 2 b-tag (bottom) categories.
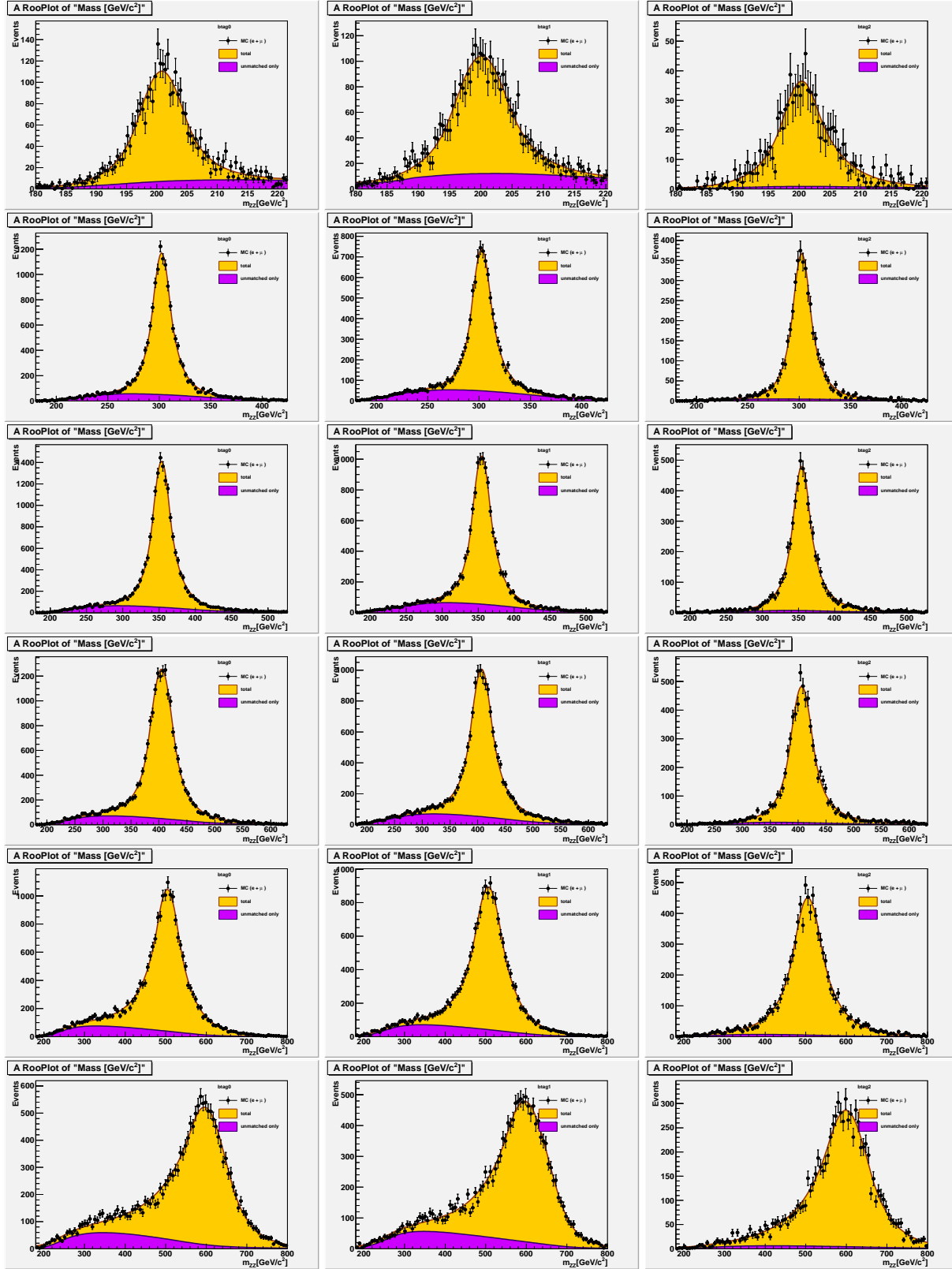
Figure 57: Distribution of m_{ZZ} invariant mass and probability parameterization in 0 b-tag (left), 1 b-tag (middle), and 2 b-tag (right) categories. From top to bottom: background, SM Higgs $m_H = 200$ GeV, $m_H = 300$ GeV, $m_H = 350$ GeV, $m_H = 400$ GeV, $m_H = 500$ GeV, and $m_H = 600$ GeV.
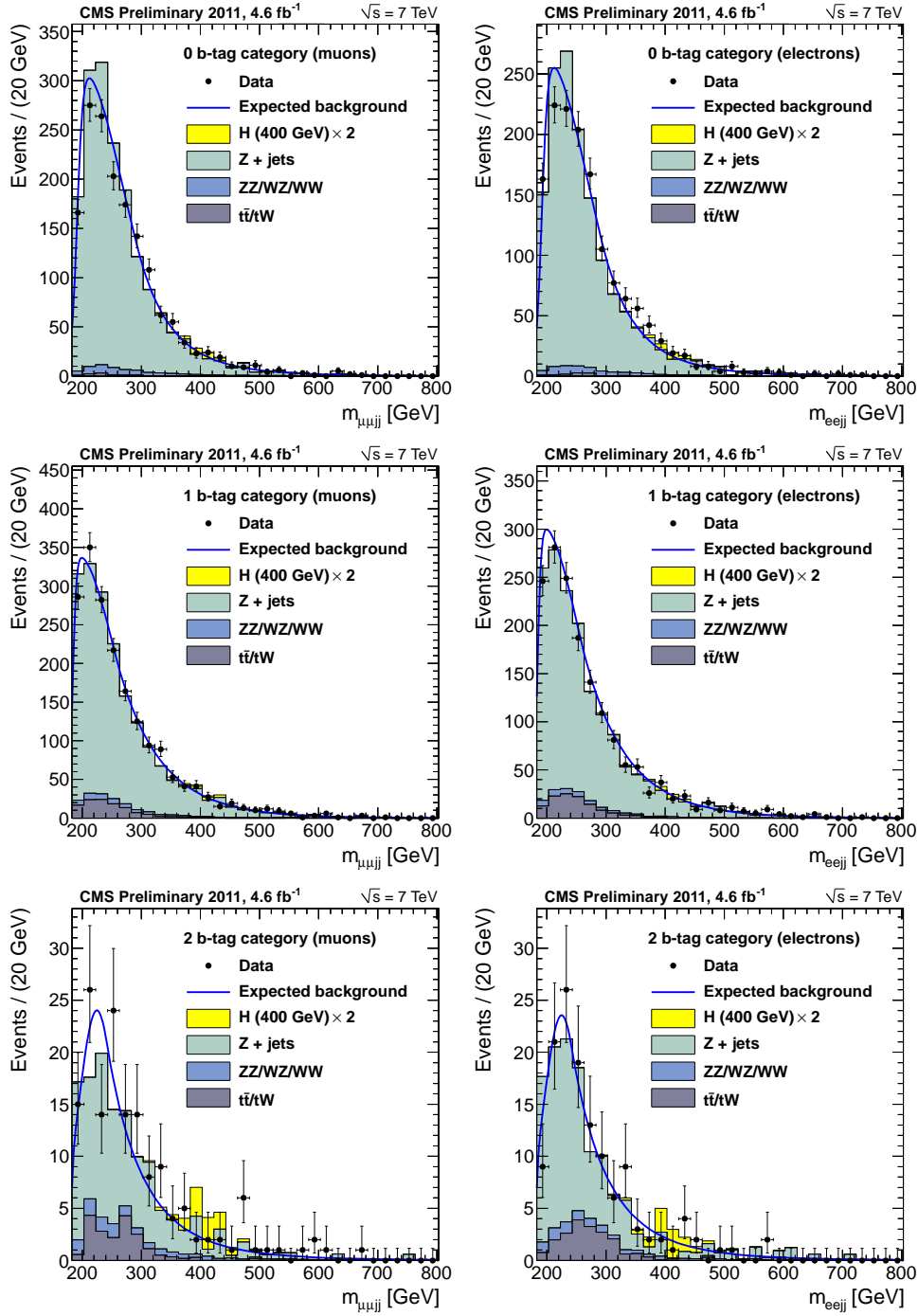
Figure 58: The m_{ZZ} invariant mass distribution after final selection in six categories: 0 b-tag (top), 1 b-tag (middle), 2 b-tag (bottom), $\mu^-\mu^+q\bar{q}$ (left) and $e^-e^+q\bar{q}$ (right), Points with error bars show distributions of data, solid histograms depict the background expectation from simulated events with the different components illustrated. Also shown is a hypothetical signal with mass of 400 GeV, multiplied by a factor of 10 for illustration. Solid curved line shows prediction of background from sideband extrapolation procedure, with the hypothetical signal included.

Based on the expected normalization and shape of the m_{ZZ} distribution, for signal and background, and the corresponding systematic uncertainties, we generate a large number of random pseudo-experiments. For each of them, the expected background distribution is generated and a likelihood fit is performed. Observed and expected exclusion limits on the product of the Higgs boson production cross section and the branching fraction of $H \to ZZ$ are presented in Fig. 59. For comparison, expectation of the production cross section and the branching fraction are shown in the SM and in the SM4 model. We further incorporate uncertainties on the Higgs production cross section and present a limit on the ratio of the SM Higgs boson production cross section to the SM expectation in Fig. 60. A similar limit on the ratio to the Higgs boson production cross section in the SM4 model is shown in Fig. 61. The ranges 153 – 162 GeV and 200 – 470 GeV of SM4 Higgs mass hypotheses are excluded at 95% CL. The exclusion limits in Fig. 60 are approaching those of the SM expectation for the Higgs boson production. Results with the Bayesian approach are consistent with those of $\mathrm{CL_s}$.

In the absence of the Higgs boson, these limits are expected to reach the SM expectation with the increased LHC luminosity. At the same time, these presented results along with comparable results from the CMS collaboration [34] obtained with the other channels of the $H \to ZZ$ decay, such as $H \to ZZ \to 4l$ and $2l2\nu$, and with the $H \to WW$ decay provide exclusion of the SM Higgs boson at 95% CL in a wide range within the mass window in this search.
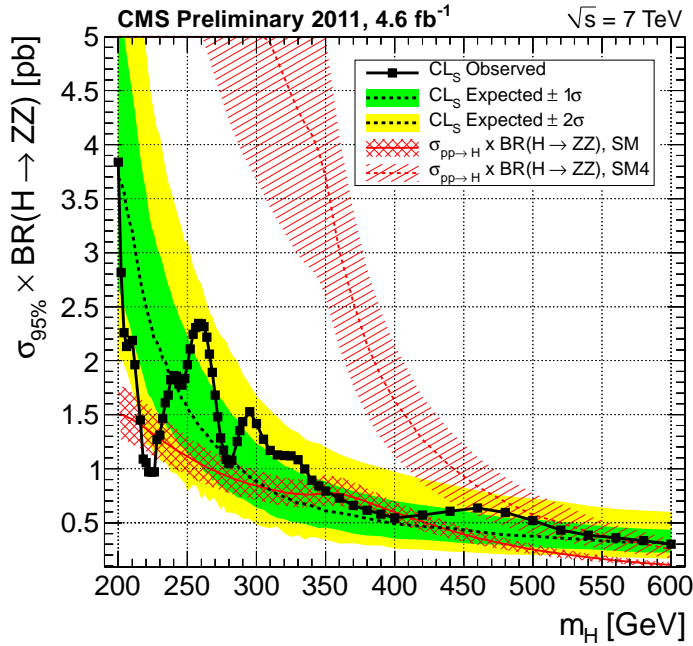

Figure 59: Observed (dashed) and expected (solid) 95% CL upper limit on the product of the Higgs boson production cross section and the branching fraction of $H \to ZZ$ using 4.6 fb^{-1} of data obtained with the $\mathrm{CL_s}$ technique. The 68% and 95% ranges of expectation are also shown with green and yellow bands. The expected product of the SM Higgs production cross section and the branching fraction is shown as a red solid curve with a band indicating theoretical uncertainties at 68%. The same expectation in the SM4 model are shown with a red dashed curve with a band indicating theoretical uncertainties.
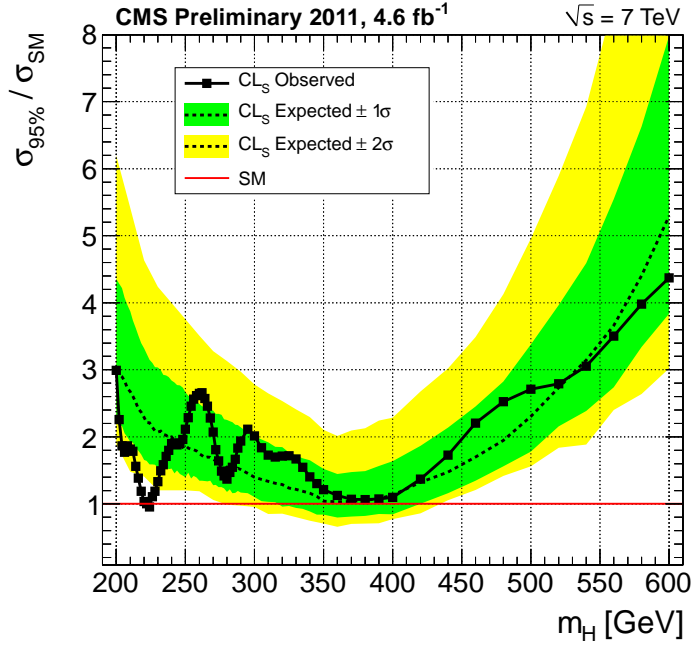
Figure 60: Observed (dashed) and expected (solid) 95% CL upper limit on the ratio of the Higgs boson production cross section to the SM expectation using 4.6 fb^{-1} of data obtained with the CL_s technique. The 68% and 95% ranges of expectation are also shown with green and yellow bands. The solid line at 1 indicates SM expectation.
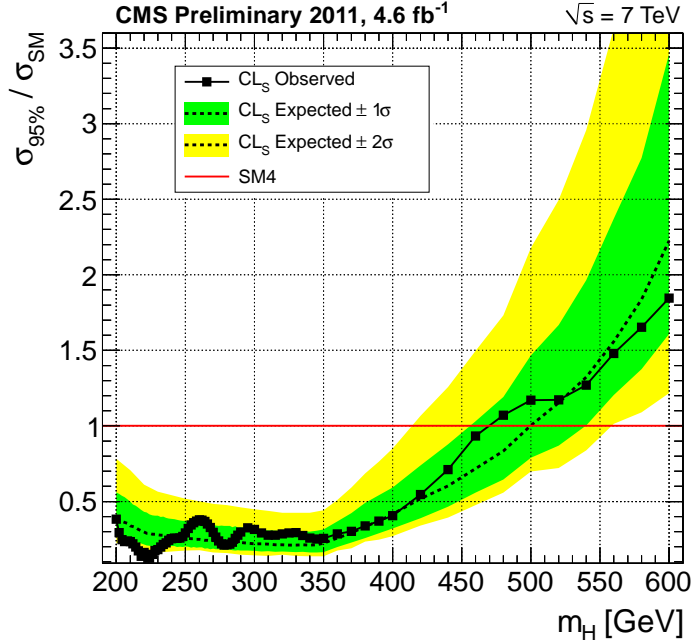

Figure 61: Observed (dashed) and expected (solid) 95% CL upper limit on the ratio of the Higgs boson production cross section to the expectation with the SM4 model using 4.6 fb^{-1} of data obtained with the CL_s technique. The 68% and 95% ranges of expectation are also shown with green and yellow bands. The solid line at 1 indicates SM4 expectation.

10 Analysis of the Lower Mass Range

Analysis of the $H \rightarrow ZZ$ final state is possible with one virtual Z, therefore extending the analysis to Higgs boson masses below the $2m_Z$ GeV threshold. This has been done successfully in the $H \rightarrow ZZ \rightarrow 4\ell$ final state. However, both $H \rightarrow ZZ \rightarrow 2\ell 2q$ and $H \rightarrow ZZ \rightarrow 2l2\nu$ final states were expected to be overwhelmed with the dominant Z+jets background without selection on the high-p_T objects.

Nonetheless, the $H \rightarrow ZZ^*$ analysis is still feasible when we require the on-shell Z to decay to two jets, therefore reducing the Z+jets background with an invariant mass cut on the dijet mass m_{jj}. This approach also leaves the sidebands of the m_{jj} variable for data-driven background estimate, in the same manner as in analysis above the ZZ threshold. The signal production rate (cross-section times branching fraction) falls as we go below threshold, but so does background production rate, as can be seen in Fig. 62. As a result, competitive sensitivity could be obtained on the SM Higgs production in the mass range between about 130 and 160 GeV. Below 130 GeV and between 160 and 180 GeV, $H \rightarrow ZZ$ production rate falls dramatically. The mass range between 130 and 160 GeV has been of particular interest recently after SM Higgs boson had been excluded at higher masses and after certain excess of events above expectation had been observed in this mass range.

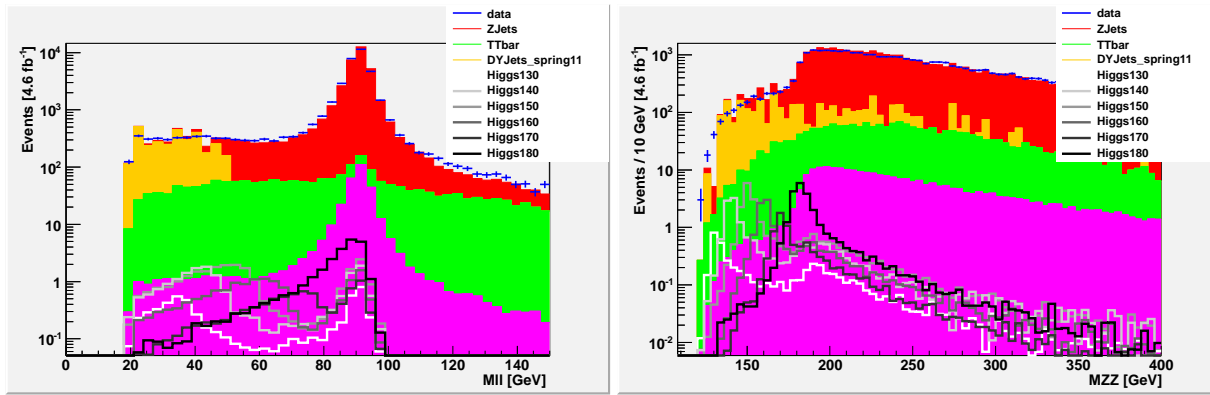*All the low mass plots are affected by: low statistics DY+jets sample and spring11 samples for mh140,160,170,180*

Figure 62: Leptonic Z invariant mass (left) and ZZ invariant mass (right) for signal and backgrounds. Monte Carlo expectations are compared to data after the preselection cuts listed in Sec.10.1.

10.1 Event selection in the lower mass range

The analysis follows an approach similar to the high mass, with few modifications. The lepton p_T requirements have been relaxed to 10(20) GeV, for the lower (higher) p_T leptons. Correspondingly, only double electron and double muon triggers are exploited, the threshold of single muon trigger being above 20 GeV (see Section 3.1 for more details). The dilepton invariant mass $m_{\ell\ell}$ is no longer required to be consistent with the Z mass peak, since we are reconstructing $Z^* \rightarrow \ell^-\ell^+$. We require $m_{\ell\ell} > 20$ GeV. The upper bound on $m_{\ell\ell}$ come naturally from the kinematic constraint $m_{\ell\ell} < m_{ZZ} - m_Z$, where $m_Z \simeq 91.2$ GeV. Here the dijet invariant mass is constrained to the m_Z value when the m_{ZZ} mass is calculated, using the same kinematic fit approach as in the higher mass range analysis.

In summary the preselection requirements are

- at least 2 muons or 2 electrons;

- leading lepton $p_T > 10$ GeV, subleading lepton $p_T > 20$ GeV, $M(ll) > 20$ GeV;

- muons $|\eta| < 2.4$ GeV;

- electrons $|\eta| < 2.5$ GeV;

- lepton quality requirements as listed in Section 3.2;

- at least 2 jets with $p_T > 30$ GeV and invariant mass $75 < m_{jj} < 105$ GeV;

59

817   • jet id and jet pile-up correction as listed in Section 3.3.

818   For more details see Section 3.

10.2   Kinematic and angular distributions in the lower mass range

820 Upon closer investigation, we observe only weak discrimination of the five angular distributions between signal
821 and background. This is due to the fact that Higgs at lower masses has nearly democratic composition of different
822 helicity amplitudes in decay and therefore helicity angles have weak discrimination power. There is also small
823 difference in the production angle distributions, as shown in Fig. 63. Therefore to simplify the approach, we do
824 not apply selection on the angular likelihood in analysis of the lower mass range. Such likelihood selection might
825 still be considered, but no significant differences are expected.
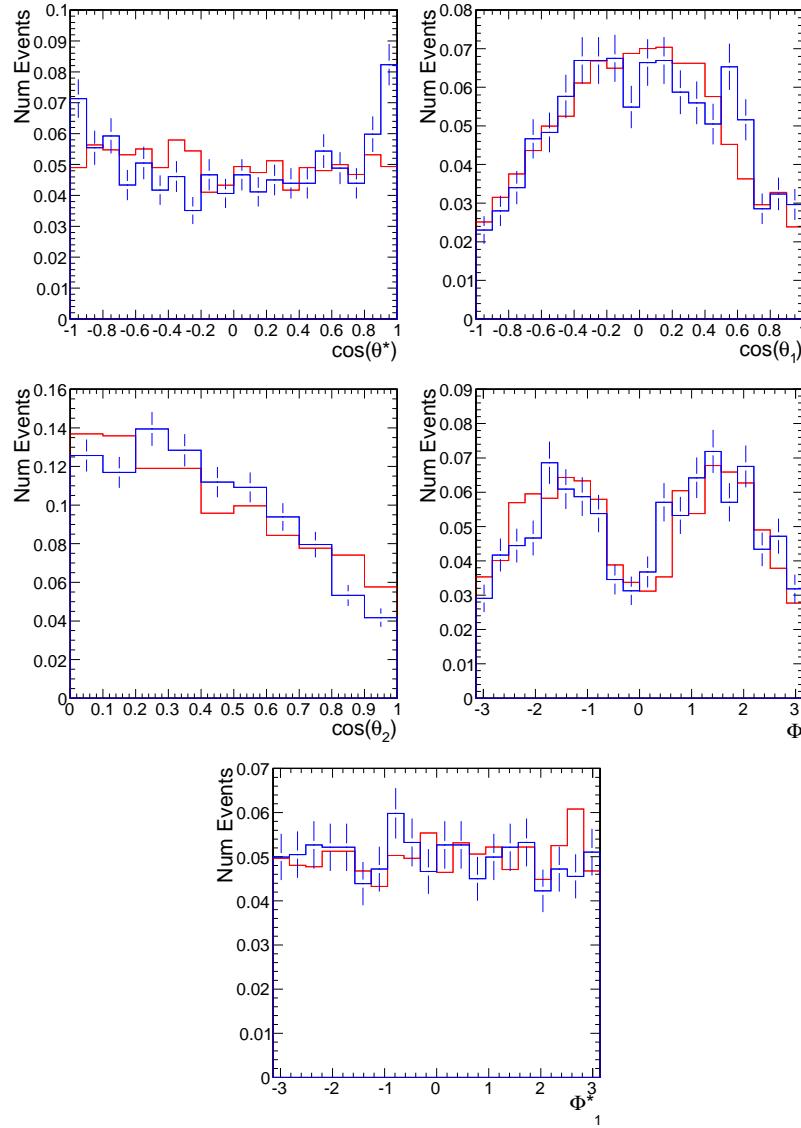

Figure 63: Distribution of helicity and production angles for a 150 GeV Higgs signal (red lines) and data sidebands (blue lines with error bars).

826 On the other hand, distributions of the dilepton invariant mass $m_{\ell\ell}$ shows significant difference between the signal
827 and background, see Fig. 64. A statistical analysis incorporates both $m_{\ell\ell}$ and m_{ZZ} to maximize sensitivity.
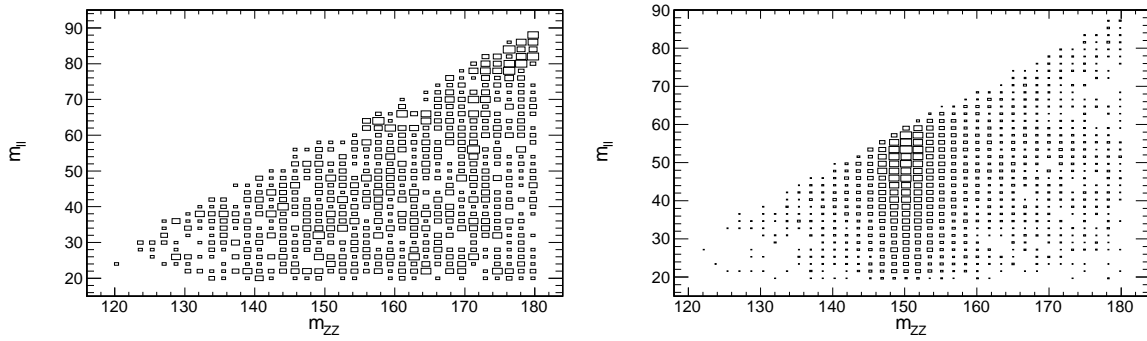
Figure 64: Scatter plot of m_{ZZ} vs $m_{\ell\ell}$ for background (left) and signal (right) simulation.

10.3 Jet structure and flavor, and MET at the lower mass range

We follow the same strategy to split events into three b-tag categories (0, 1, and 2 b-tag). The same TCHE b-tag algorithm thresholds are used. In the $0b$-tag category, no quark-gluon likelihood cut is applied since the distribution is very similar in signal and Z+jets, especially for very low Higgs mass, as can be seen in Fig. 65.
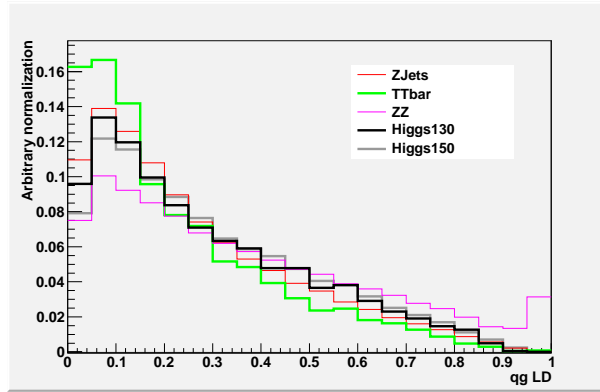

Figure 65: QG likelihood for signal and backgrounds in the 0 btag category (shape comparison) after the preselection cuts listed in Sec.10.1.

To suppress $t\bar{t}$ background in the $2b$-tag category, we apply selection on MET. This selection is different from the higher-mass range where MET significance is used, because here we do not need to deal with strong mass-dependence of MET threshold. In Fig. 66, the MET and MET significance distributions, after the selection cuts in the 2 b-tag category, are shown. As can be seen, large portion of the background in this category is due to $t\bar{t}$ ($\sim$ 50 % in the full $M(ZZ)$ spectrum and $\sim$ 100% in the region $120 < M(ZZ) < 170$ GeV) and that is mainly concentrated at high MET. In Fig. 67 the signal and background efficiency in the 2 btag category is plotted as a function of the MET or MET significance cut. Higgs samples with 150 GeV and 130 GeV masses have been considered and a cut on m_{ZZ} within ± 10 GeV with respect to the nominal Higgs mass has been applied. As can be seen, the efficiency of the MET cut can be slightly lower at low Higgs masses but we can identify a MET cut ($< 50 GeV$) which gives 100% efficiency for the signal at all the masses and with high background rejection (65%). Moreover, as shown in Section 10.8.1, the systematics on a MET significance cut is larger than for a simple MET cut.
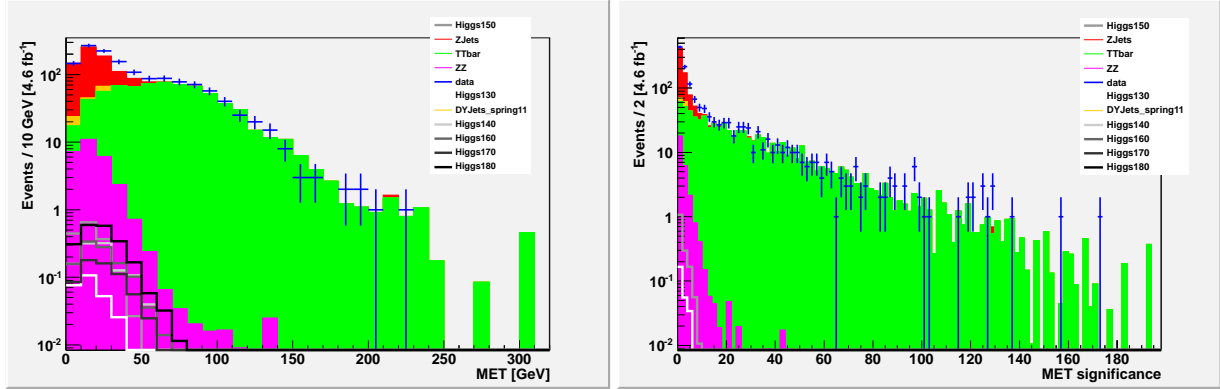
Figure 66: MET and MET significance distributions in the 2 btag category after the preselection cuts listed in Sec.10.1. Monte Carlo expectations for signal and backgrounds are compared with data.
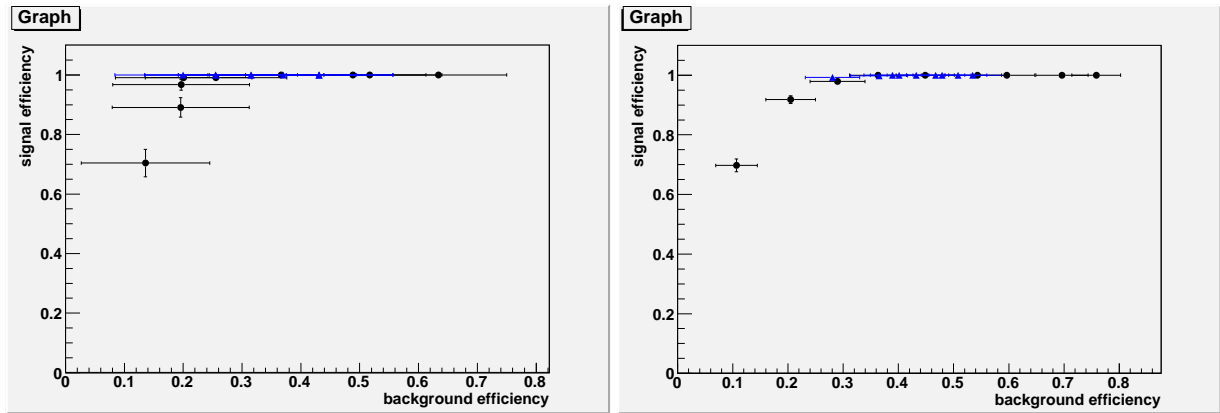

Figure 67: Signal against background efficiency for several MET cut (from 20 to 100 GeV in steps of 10 GeV, black bullets) and MET significance cuts (from 10 to 34 with steps of 3, blue triangles). Higgs samples with nominal mass of 130 GeV (left) and 150 GeV (right) are considered and a ZZ mass cut ± 10 GeV is applied on top of the preselection cuts listed in Sec.10.1.

10.4 Signal parameterization in the lower mass range (m_{ZZ})

Signal parameterization is performed for mass points $m_H = 130, 140, 150, 160, 170\,\text{GeV}$, see Fig. 68. Parameterization in the intermediate mass points is extrapolated from these distributions, as shown for efficiency in Fig. 69.
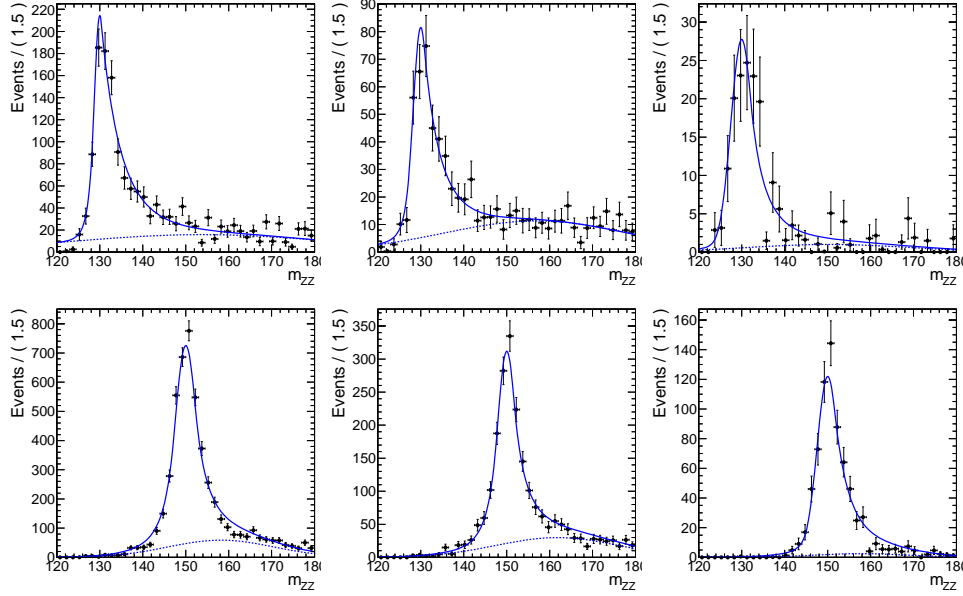

Figure 68: Signal parameterizations for two choice Higgs masses in each of the three b-tag categories after extrapolating parameters to arbitrary Higgs mass.
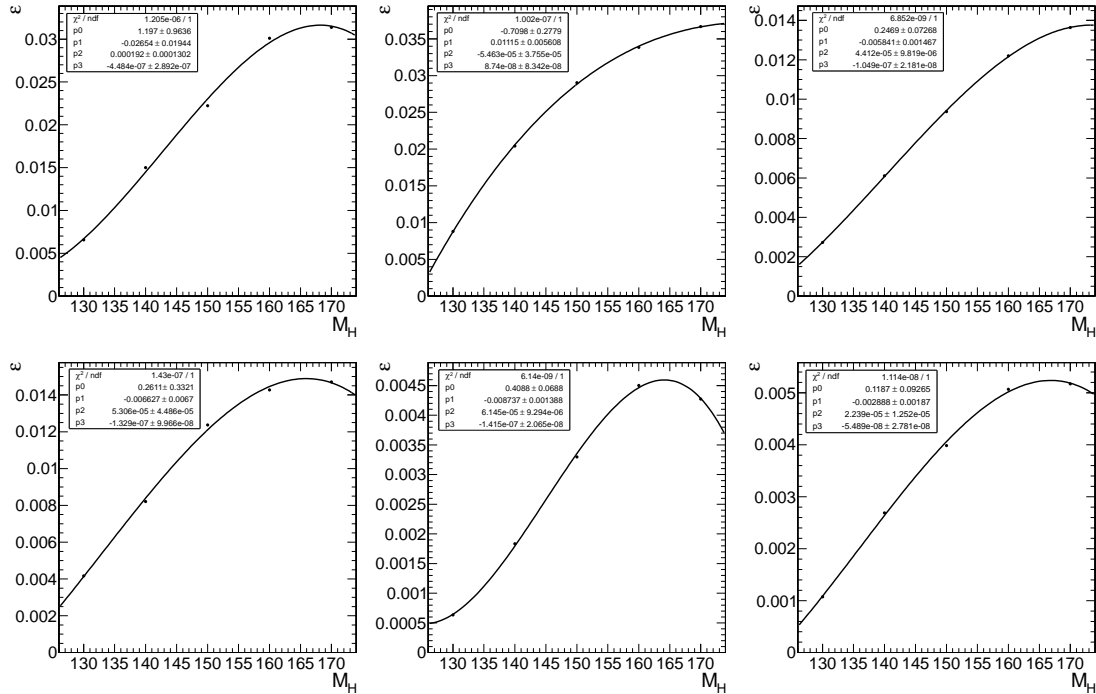

Figure 69: Extrapolation of signal efficiency to arbitrary Higgs mass for all 6 channels: 0 b-tag electrons (top left), 0 b-tag muons (top middle), 1 b-tag electron (top right), 1 b-tag muons (bottom left), 2 b-tag electron (bottom middle), and 2 b-tag muons (bottom right).

10.5 Background estimates in the lower mass range (m_{ZZ})

We extrapolate background m_{ZZ} and $m_{\ell\ell}$ distributions from the m_{jj} sidebands. While at the high-mass range we had to deal with threshold effect near the ZZ kinematic limits, there is no such an effect at the lower mass range. Recall that the scale factor $\alpha(m_{ZZ})$ was nearly constant, but deviated from this trend as it was approaching the threshold. No such non-uniformity has been observed in the low mass range with available MC statistics. Therefore, we extrapolate the background distributions from the m_{jj} sidebands using a single α value which is treated as independent from the mass for $120 < m_{ZZ} < 170$ GeV. Given the very low statistics of the Monte Carlo sample for low mass Drell-Yan + jets ($0.6 fb^{-1}$), this contribution has not been considered in the α computation. *We will need to review this computation, as well as the plots in previous sections when larger Monte Carlo sample is available for DY+jets.* In Table 24 the values of α in different b-tag categories is reported, also considering separately the various background contributions.

Table 24: Values of α in different b-tag categories and for different backgrounds. The errors are due to available statistics in Monte Carlo. It can be noticed that in the 2 b-tag category no events from the low mass Drell-Yan Monte Carlo sample pass the cuts because of the very low statistics of the sample.

	low mass DY	Z+jets	$t\bar{t}$	ZZ	total	total (w/o low mass DY)
0 btag	1.37 ± 0.39	1.31 ± 0.06	1.20 ± 0.20	2.41 ± 0.19	1.35 ± 0.24	1.31 ± 0.06
1 btag	0.84 ± 0.47	1.19 ± 0.13	0.78 ± 0.07	2.38 ± 0.33	0.90 ± 0.28	0.99 ± 0.07
2 btag	-	1.63 ± 0.86	0.89 ± 0.16	3.8 ± 1.1	1.02 ± 0.18	1.02 ± 0.18

In Fig. 70, we show the m_{ZZ} distribution of events in the m_{jj} sideband and the parameterization of this distribution. This distribution is compared separately to sideband data in each b-tag category in Fig. 71. Fig. 71 also illustrates expected background distributions and the observed data in the signal region. Table 25 reports the number of events observed in sidebands and observed and expected (sidebands times α) in signal region.
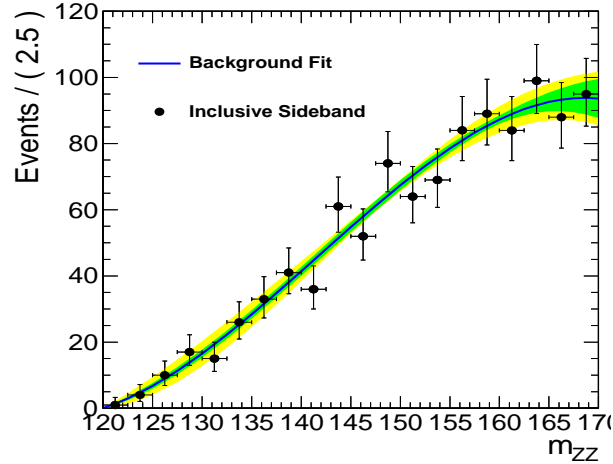

Figure 70: Fit to data sidebands. The blue line represents the maximum likelihood fit result while the green and yellow area represent the 1σ and 2σ bands respectively.

Table 25: Number of events observed in sidebands; expected number of events (sidebands times α) and the observed number of events in signal region with 4.6 fb^{-1}. The uncertainty in the number of expected events is due to the uncertainty on α added in quadrature with the statistical uncertainty due to the number of observed events in sidebands, see Table 24.

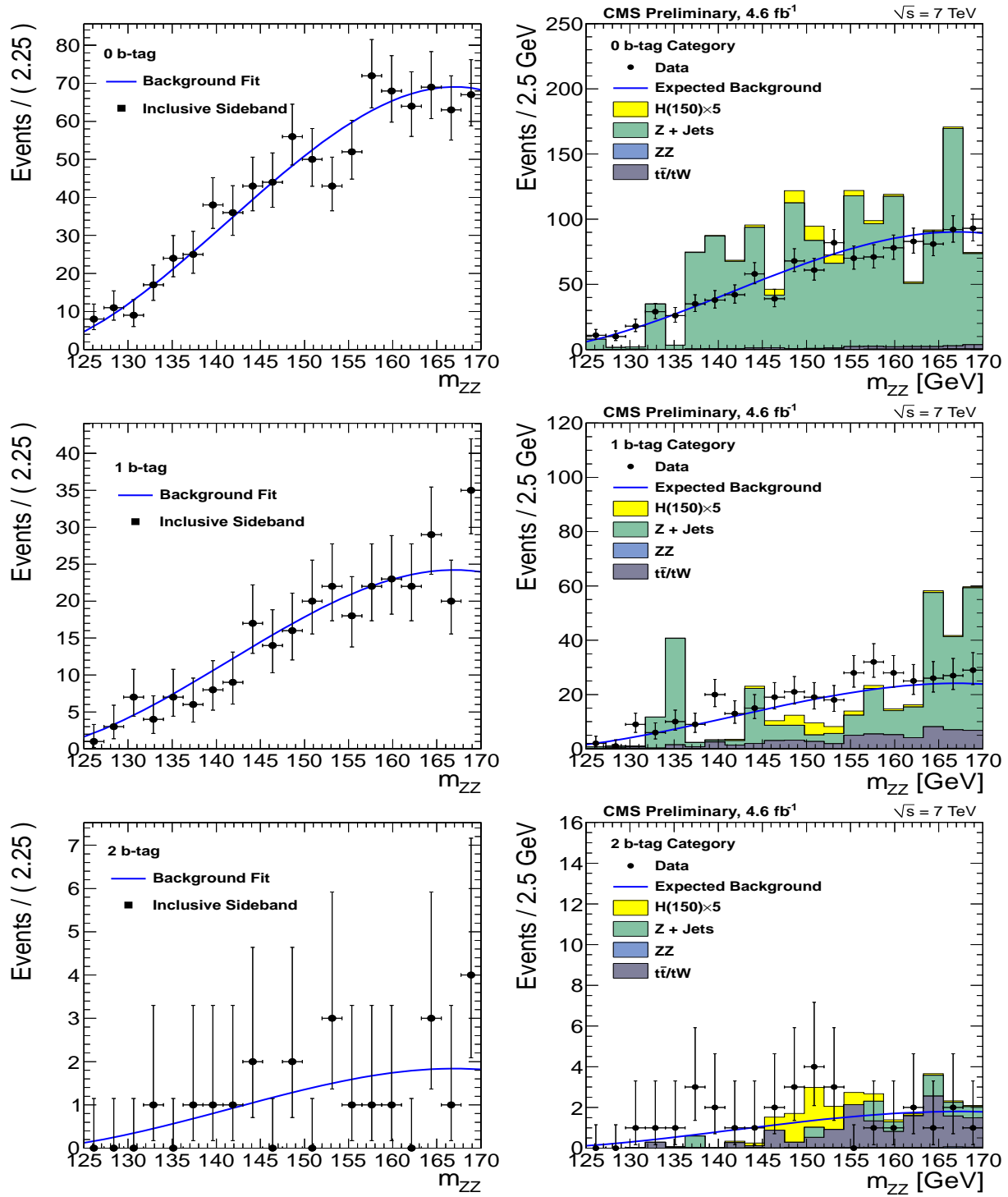|	observed in sidebands	expected in signal region	observed in signal region
0 btag	864	1129 ± 66	1087
1 btag	303	300 ± 27	360
2 btag	23	23 ± 6	30

Figure 71: Distribution of m_{ZZ} invariant mass shown in the m_{jj} sideband region (left) and signal region (right) in the 0 b-tag (top), 1 b-tag (middle), and 2 b-tag (bottom) categories. Shown are the data (points with error bars), expected distribution for background obtained from sidebands (blue lines). and in the signal region background simulation with different contributions.

10.6 Signal parameterization in the lower mass range $(m_{ZZ}, m_{\ell\ell})$

In the analysis of $H \rightarrow ZZ^*$ decay, signal and background distributions differ not only in the m_{ZZ}, but in the $m_{\ell\ell}$ observable as well, as shown in Fig. 64. The signal m_{ZZ} parameterization is discussed in Section 10.4. Extension to the 2D parameterization requires proper treatment of correlation of variables. This has been extensively discussed in Ref. [2] and we follow its implementation. The signal probability distributions becomes:

$$\mathcal{P}_{\text{sig}}(m_{ZZ}, m_{\ell\ell}) \propto \frac{m_{\ell\ell}^3}{(m_{\ell\ell}^2 - m_Z^2)^2 + m_Z^2 \Gamma_Z^2} \times \beta(m_{ZZ}, m_{\ell\ell}) \times F_{JPC}(m_{ZZ}, m_{\ell\ell}) \times \mathcal{P}_{\text{CB}}(m_{ZZ}) \times \mathcal{G}(m_{\ell\ell}) \quad (2)$$

where we have defined the Z^* propagator term with the threshold function [39]:

$$\beta(m_{ZZ}, m_{\ell\ell}) = \sqrt{\left[1 - \frac{(m_Z + m_{\ell\ell})^2}{m_{ZZ}^2}\right]\left[1 - \frac{(m_Z - m_{\ell\ell})^2}{m_{ZZ}^2}\right]} \quad (3)$$

the term which depends on quantum numbers of the Higgs resonance, with the angular dependence integrated out:

$$F_{JPC}(m_{ZZ}, m_{\ell\ell}) = \int d\cos\theta_1 \int d\cos\theta_2 \int d\Phi \, \frac{d\Gamma(m_{ZZ}, m_{\ell\ell}, \cos\theta_1, \cos\theta_2, \Phi)}{d\cos\theta_1 d\cos\theta_2 d\Phi} \quad (4)$$

the Higgs resonance $\mathcal{P}_{\text{CB}}(m_{ZZ})$ parameterization in m_{ZZ}, as shown in Section 10.4, and acceptance function $\mathcal{G}(m_{\ell\ell})$ due to detector effects (loss of low momentum leptons). The resulting distributions are shown in Fig. 72. The Higgs width Γ is negligible compared to detector resolution for Higgs masses considered here, see Fig. 54. Therefore, $\mathcal{P}_{\text{CB}}(m_{ZZ})$ does not require convolution with the Breit-Wigner function, and is parameterized with a double-Crystal-Ball function to describe non-Gaussian detector resolution and final state radiation effects.
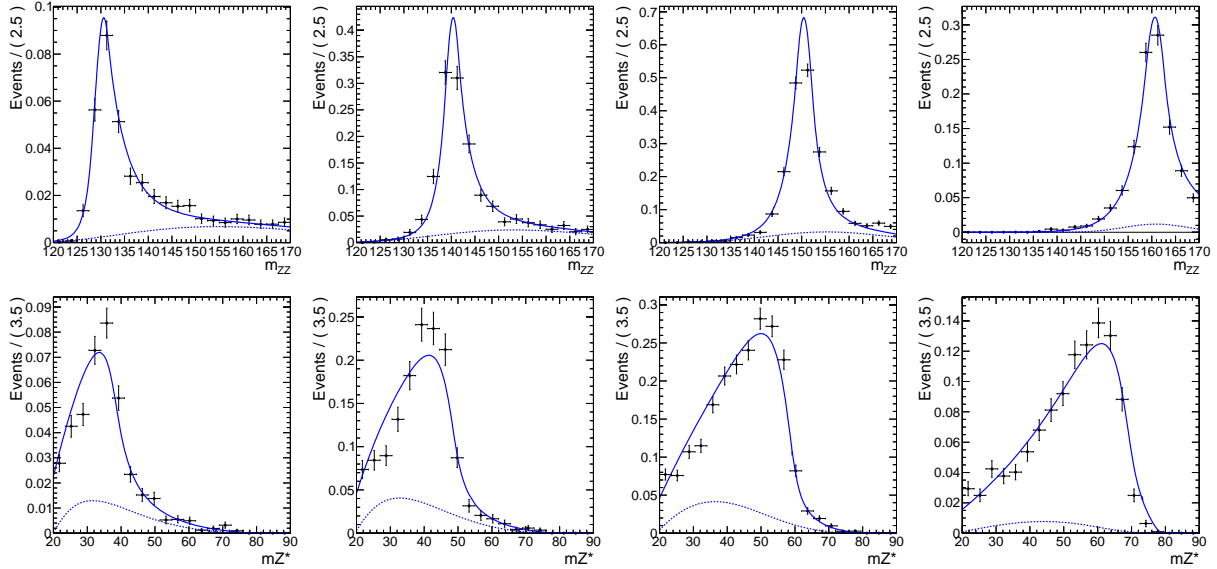

Figure 72: Projection of the 2D $(m_{ZZ}, m_{\ell\ell})$ signal parameterization on the m_{ZZ} (top) and $m_{\ell\ell}$ (bottom) observable. Signal parameterizations is shown for four choice Higgs masses, from left to right: 130, 140, 150, 160 GeV, in the 0 b-tag category.

10.7 Background parameterization in the lower mass range $(m_{ZZ}, m_{\ell\ell})$

In order to keep backwards-compatibility with 1D background parameterization of m_{ZZ} distribution discussed in Section 10.5, our 2D parameterization is written as follows:

$$\mathcal{P}_{\text{bkg}}(m_{ZZ}, m_{\ell\ell}) \propto \mathcal{P}_{\text{bkg}}^{\text{1D}}(m_{ZZ}) \times \frac{F_{\text{bkg}}(m_{ZZ}, m_{\ell\ell})}{\int dx F_{\text{bkg}}(m_{ZZ}, x)} \tag{5}$$

where the function $F_{\text{bkg}}(m_{ZZ}, m_{\ell\ell})$ describes $m_{\ell\ell}$ distribution at any given value of m_{ZZ} and the integral (done analytically) in the denominator insures that the function projection on m_{ZZ} is $\mathcal{P}_{\text{bkg}}^{\text{1D}}(m_{ZZ})$, taken from Section 10.5. The function $F_{\text{bkg}}(m_{ZZ}, m_{\ell\ell})$ reflects correlation between the two observables and includes the threshold function from Eq. (3). Otherwise the m_{ZZ} and $m_{\ell\ell}$ dependence is parameterized with polynomial functions.

Projections of the $\mathcal{P}_{\text{bkg}}(m_{ZZ}, m_{\ell\ell})$ parameterizations are illustrated in Fig. 73 where the left plots show projections on m_{ZZ} and $m_{\ell\ell}$ of the full distribution, while the other plots show projections for several slices in m_{ZZ}.

Both signal and background parameterizations ensure that there is an exact kinematic limit of $m_{\ell\ell}$ distribution for a given value of m_{ZZ}:

$$m_{\ell\ell} < m_{ZZ} - m_Z \tag{6}$$

where $m_Z \simeq 91.2$ GeV. This relationship in Eq. (6) is exact because the kinematic fit ensures that $m_{jj} = m_Z$ when m_{ZZ} is calculated. This effect is specific to the $H \to ZZ^{(*)} \to (q\bar{q})(\ell^-\ell^+)$ analysis with a kinematic fit and a constraint $m_{jj} = m_Z$. In the $H \to ZZ^{(*)} \to (\ell^-\ell^+)(\ell^-\ell^+)$ analysis, a very similar approach can be made, but one has to substitute $m_{\ell\ell}$ with a new variable $m^* = (m_{\ell\ell}^{(1)} + m_{\ell\ell}^{(2)} - m_Z)$. Then the relationship in Eq. (6) still holds for m^* and m_{ZZ}.
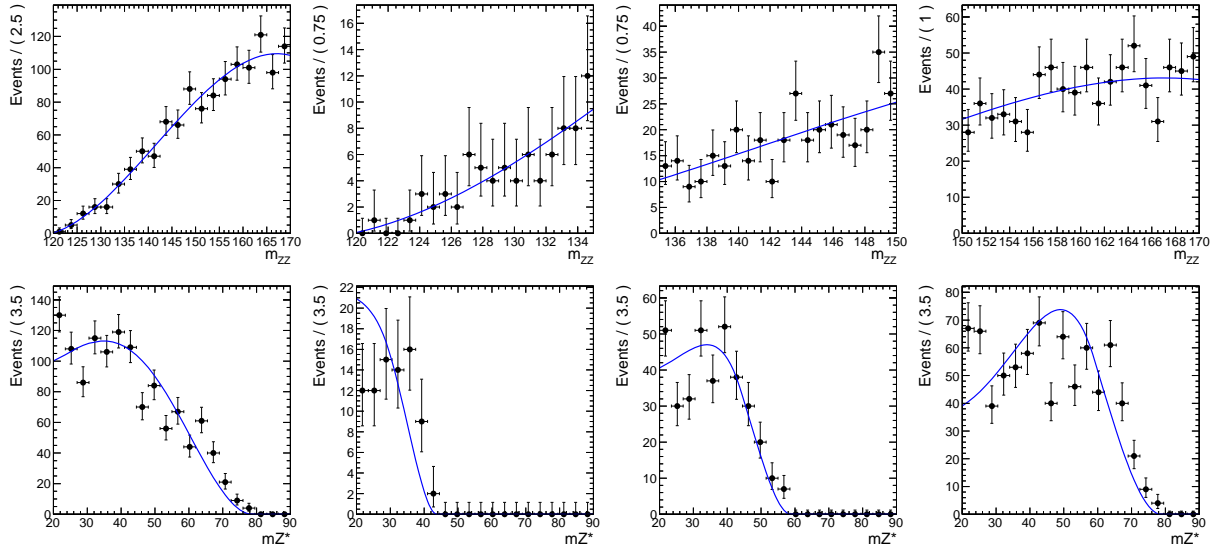

Figure 73: Projection of the 2D $(m_{ZZ}, m_{\ell\ell})$ background parameterization on the m_{ZZ} (top) and $m_{\ell\ell}$ (bottom) observable. The data points are obtained from m_{jj}) sideband. Left plots show the full $120 < m_{ZZ} < 170$ GeV range, while the other plots show subranges $120 < m_{ZZ} < 135$ GeV (second from the left), $135 < m_{ZZ} < 150$ GeV (third from the left), $150 < m_{ZZ} < 170$ GeV (right).

10.8 Systematic uncertainties in the lower mass range

Uncertainties in the expected signal yields are mostly identical to those estimated in Table 14.

Uncertainties in the expected background yields and mass distributions shapes come from sideband extrapolation and are dominated by statistical uncertainties in the sideband samples. *Statistical uncertainties from Monte Carlo samples still to be finalized when the low-mass DY samples are available.*

10.8.1 MET resolution

The uncertainty on the MET cut signal efficiency is estimated by comparing Monte Carlo and data. We expect no real MET in the signal and Z+jets events reproduce quite well the features of signal events. The $t\bar{t}$ contribution, as predicted by Monte Carlo, is therefore subtracted to the MET and MET significance distributions (also in data), as shown in Fig. 74. The difference in efficiency of the chosen MET cut in data and Monte Carlo is then estimated as systematics. This systematics is shown in Fig. 75 and that stays below 4% for all the MET cut above 40 GeV.
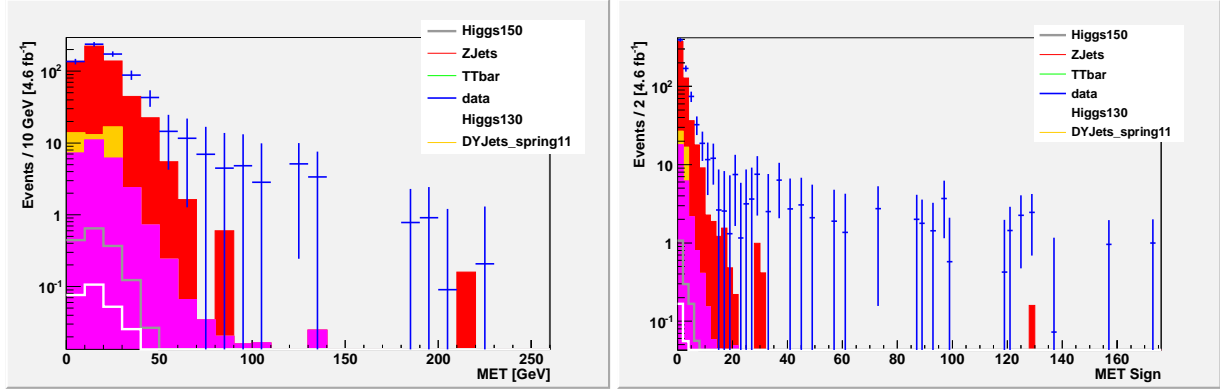

Figure 74: MET and MET significance distributions in the 2 btag category after the preselection cutslisted in Sec.10.1. $t\bar{t}$ contribution, as predicted by Monte Carlo, has been subtracted, even in data.
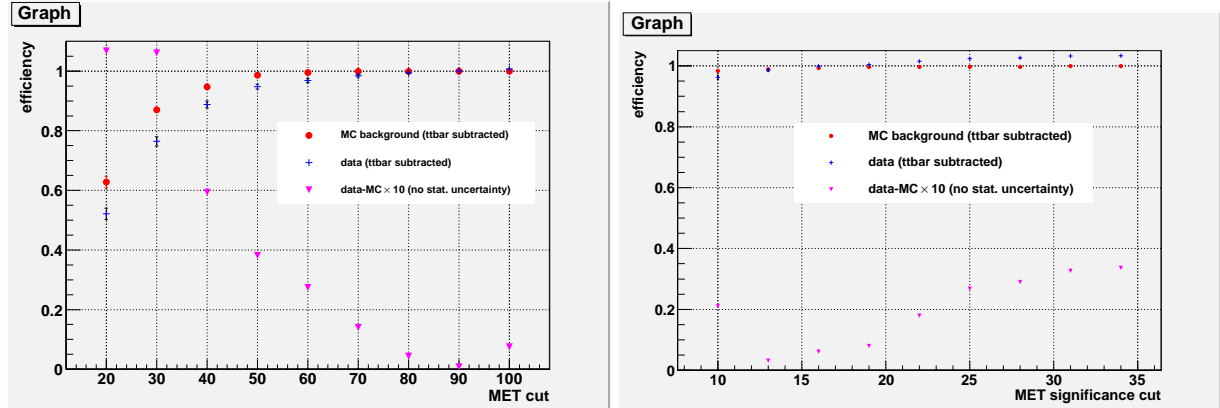

Figure 75: Efficiency in data and Monte Carlo (after $t\bar{t}$ subtraction) for various MET (left) and MET significance cuts (right) in the 2 btag category after the preselection cutslisted in Sec.10.1. The difference between data and Monte Carlo efficiencies (magnified by 10) is also shown.

10.8.2 Pile Up

To estimate the systematics uncertainty on signal efficiency due to Pile-Up simulation, we shift the distribution of the number of observed Pile-Up events by ±1. This choice, clearly arbitrary, is still expected to cover conservatively possible difference in Pile-Up between data and MC.

Table 26: Systematics on Pile-Up simulation

Higgs mass	expected yields	yields for PU-1	yields for PU+1	systematics
150	13.36	13.58	13.09	-2.0%, + 1.6%
130	2.49	2.56	2.44	-2.0%, +2.8%

10.8.3 Jet energy scale

Similarly to what has been done for the high mass analysis (see Sec. 8.2), we compare the efficiency for signal events with jet energy scale modified by $\pm 1\sigma$. The results for several Higgs masses are reported in Tab. 27.

Table 27: Systematics on jet energy scale: yields are quoted for 4.6 fb^{-1}

Higgs mass	yields at nominal JES	yields with JES $+1\sigma$	yields with JES -1σ	systematics
170	2.14	2.04	2.06	-4.7%, -3.7%
160	7.91	8.23	7.24	+4.0%, -8.5%
150	13.36	13.85	12.62	+3.7%,-5.5%
140	10.3	10.8	9.8	+4.4%, - 5.3%
130	2.49	2.7	2.3	+8.4 %, -7.6%

10.8.4 Production mechanism

Similarly to what has been done for the high mass analysis (see Sec. 8.2), we compare the efficiency for signal events in gg and VBF production. The results for several Higgs masses are reported in Tab. 28.

Table 28: Systematics on Higgs production

Higgs mass	efficiency in gg	efficiency in VBF	systematics on VBF component	systematics on total yields
150	2.49%	2.25%	-11%	-0.9%
130	0.713%	0.837%	-15%	-1%

10.9 Statistical analysis of the lower mass range

We consider two statistical approaches. The first approach is identical to the approach at higher masses where the spectrum of the m_{ZZ} distributions is examined for presence of signal peak. The results of this approach are shown in Fig. 76. Certain deviations of the observed limit with respect to expected can be traced to distribution of events in the m_{ZZ} spectrum with respect to background expectation. The latter has large uncertainty due to low statistics of the low-mass Drell-Yan MC. In Section 10.10 we discuss an alternative approach to remove dependence on MC.

The second approach is to examine 2D distribution of m_{ZZ} and $m_{\ell\ell}$. This approach was shown to have about 20% lower expected limits, but it is a more complex approach. Details of this approach are given in Sections 10.6 and 10.7, and results will be documented soon.
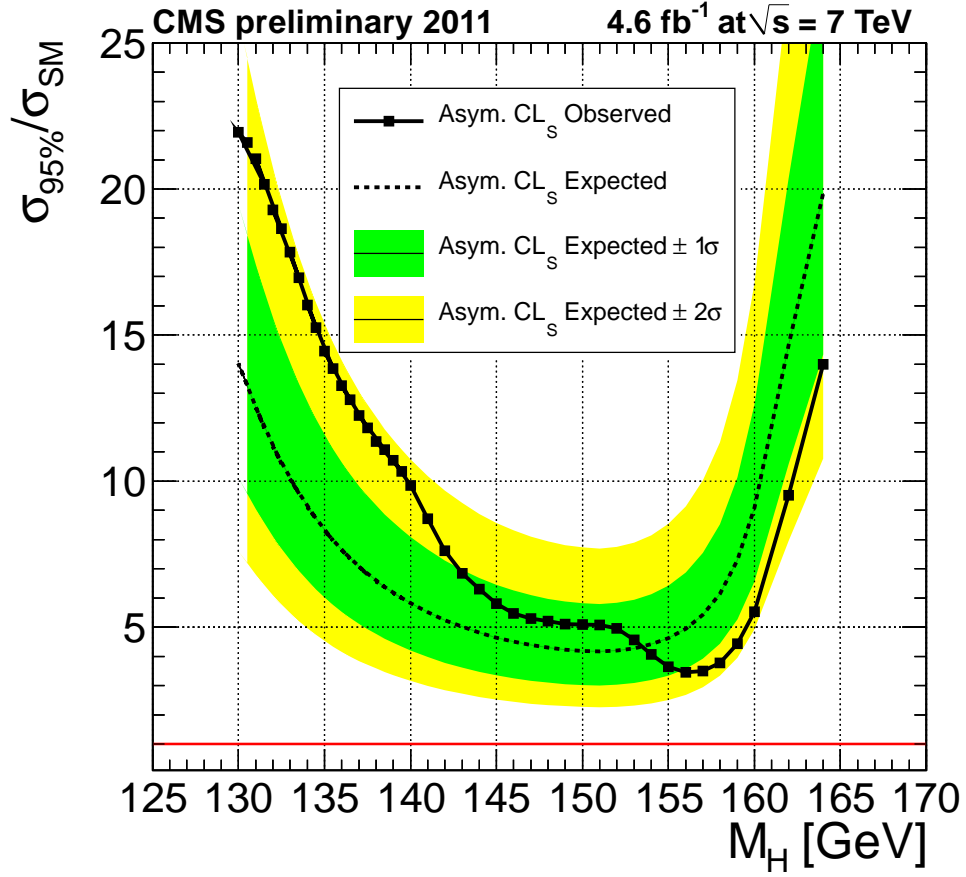
Figure 76: Result obtained using the cross-check m_{jj} sideband approach technique. Observed (dashed) and expected 95% CL upper limit on the ratio of the Higgs boson production cross section to the SM expectation using 4.6 fb^{-1} of data obtained with the CL$_s$ technique. The 68% and 95% ranges of expectation are also shown with green and yellow bands. The solid line at 1 indicates SM expectation.

10.10 Statistical analysis of the lower mass range using m_{ZZ} sideband

In Section 10.9, results with the nominal approach have been shown. With low statistics in MC simulation used for the scale factor α calculation between the m_{jj} sideband and signal region, it is possible to have fluctuations in the normalization of background parameterization. This is for example visible in normalization offset of background expectation in the 1 b-tag category in Fig. 71 and in the numbers in Table 25. While this is still covered by statistical uncertainties within 2σ, as shown in Table 25, a different approach may provide a better normalization of background expectation until a larger MC sample is available. The approach is to obtain background normalization from sidebands of the m_{ZZ} distribution rather than m_{jj}. This approach does not use any MC input, except for consistency checks. We count the number of events in the m_{ZZ} signal region distribution removing the events in the range $m_H \pm 5$ GeV, for a given Higgs mass m_H hypothesis under study. Then we rescale this number to the full m_{ZZ} range between 125 and 170 GeV using extrapolation into the removed range. The results of this approach are shown in Fig. 77. We provide more details in the individual b-tag categories in Fig. 79. While normalization changes noticeably in the 1 b-tag category, it is the least sensitive category and this effect is offset by the opposite effect in the 0 b-tag category. As a result, the exclusion limits in Fig. 77 are very similar to those in Fig. 76. We take results with normalization to m_{ZZ} sideband as the nominal. Exclusion on cross-section is shown in Fig. 78.
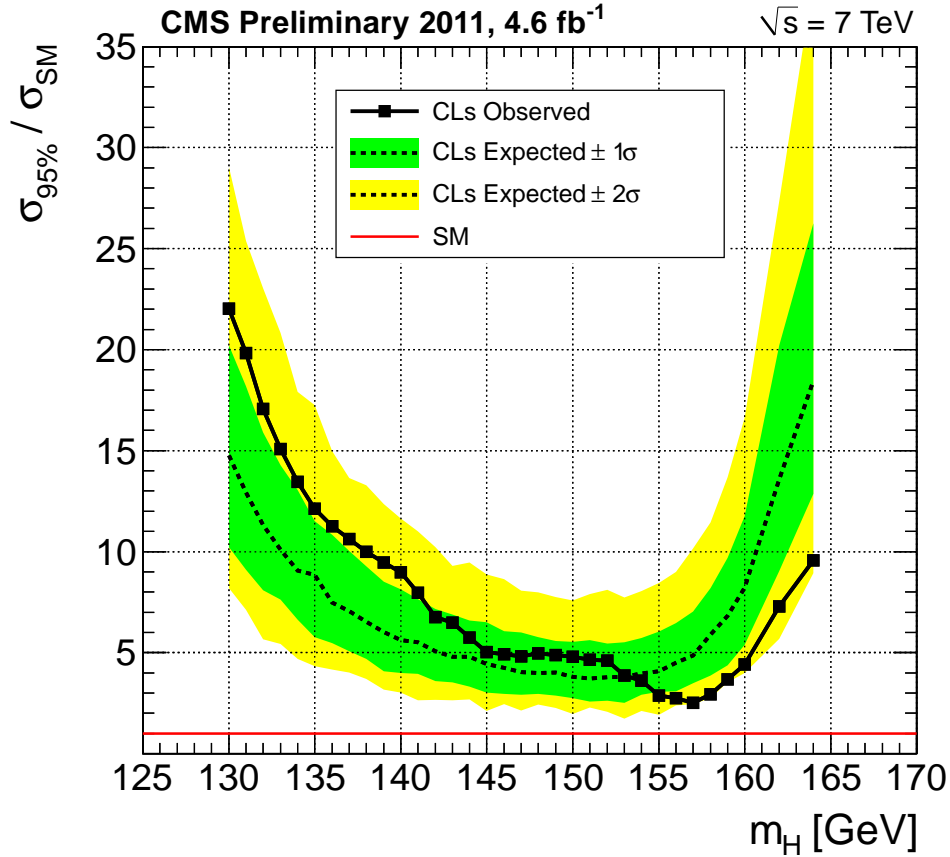

Figure 77: Result obtained using the nominal m_{ZZ} sideband approach technique. Observed (dashed) and expected 95% CL upper limit on the ratio of the Higgs boson production cross section to the SM expectation using 4.6 fb^{-1} of data obtained with the CL$_s$ technique. The 68% and 95% ranges of expectation are also shown with green and yellow bands. The solid line at 1 indicates SM expectation.
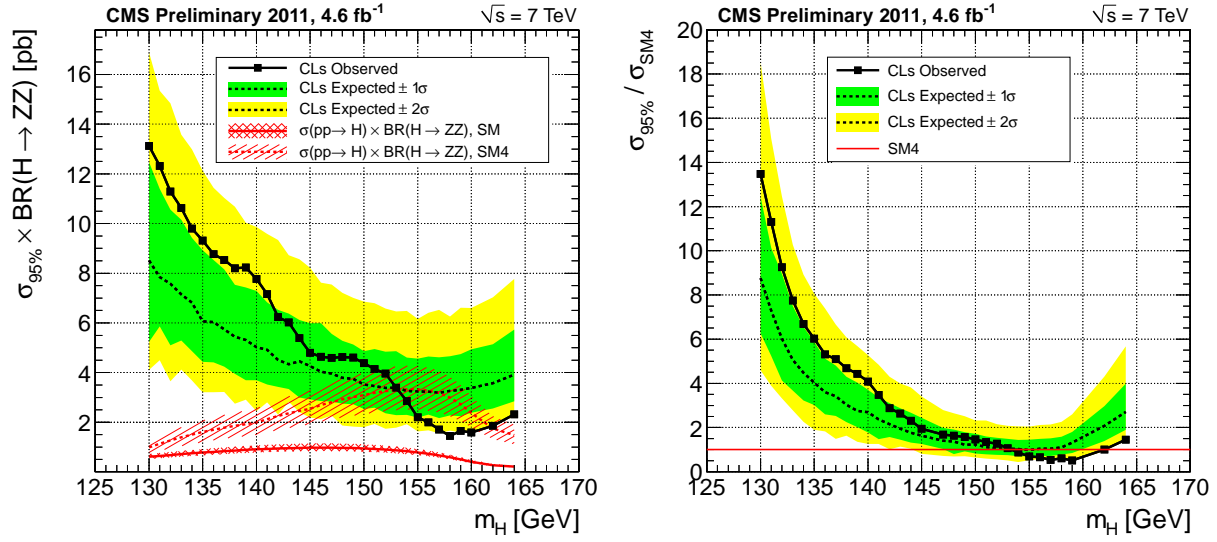
Figure 78: Expected 95% CL upper limit on the product of the Higgs boson production cross section and the branching fraction using $4.6\,\mathrm{fb}^{-1}$ of data obtained with the $\mathrm{CL_s}$ technique. The 68% and 95% ranges of expectation are also shown with green and yellow bands. The expected product of the SM Higgs production cross section and the branching fraction is shown as a red solid curve with a band indicating theoretical uncertainties at 68%. The same expectation in the SM4 model are shown with a red dashed curve with a band indicating theoretical uncertainties. Right plot shows 95% CL upper limit on the ratio of the Higgs boson production cross section to the SM4 expectation.
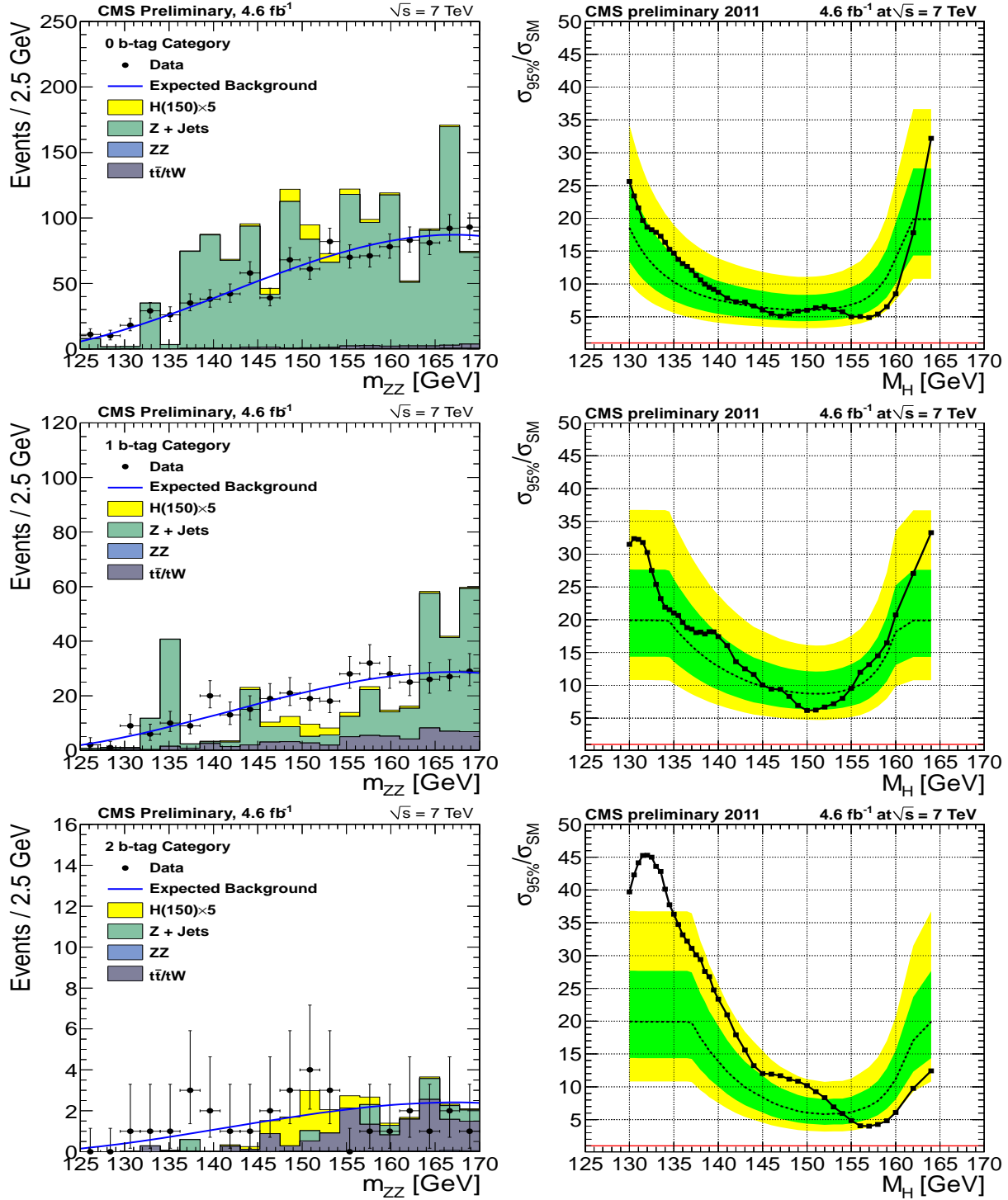
Figure 79: Distribution of m_{ZZ} invariant mass shown in the signal region (left) and 95% CL upper limit on the ratio of the Higgs boson production cross section to the SM expectation (right) in the 0 b-tag (top), 1 b-tag (middle), and 2 b-tag (bottom) categories. The left plots show are the data (points with error bars), expected distribution for background obtained from m_{ZZ} sidebands (blue lines). and background simulation with different contributions. In the right plots the expected limits with the ratio above 20 are truncated due to asymptotic approximations.

11 Summary and Conclusions

In summary, we have presented an optimized search for a Standard Model Higgs boson decay to two Z bosons with a subsequent decay to two leptons (di-electrons or di-muons) and two quark jets, $H \to ZZ^{(*)} \to 2q2\ell$. Detailed Monte Carlo simulation of a wide range of signal mass scenarios and the dominant background channels is presented, along with validation based on data collected in 2011. The selection is based on kinematic and topological quantities to discriminate between signal and background. The jet flavor is tagged based on topological probability for it to originate either from a heavy flavor quark, light flavor quark, or a gluon and the data are characterized by three signal categories with different signal and background composition. The primary selection is based on the invariant masses of the Z boson candidates and the Higgs boson candidate after a kinematic fit of the decay chain. The remaining kinematic selection is based on probability description of the angular spin correlations in the decay chain. Sideband data are used to control the dominant background contributions. Special attention is payed to systematic uncertainties in the analysis, including handling of the pile-up events in 2011 data condition.

No evidence for a SM-like Higgs boson has been found and upper limits on the production cross section for the SM Higgs boson have been set in the range of masses between 130 and 164 GeV, and between 200 GeV and 600 GeV. In this analysis we have excluded a large range of Higgs mass hypotheses in the model with the fourth generation SM-like couplings of the Higgs and, when results are combined with other Higgs decay channels from CMS, excluded [34] a wide range of masses of the SM Higgs within the mass window in this search. Prospects for a Beyond the Standard Model boson exclusion have been discussed.

74

A   Control Samples: γ+jets

The main background to the analysis is represented by continuous Standard Model Z boson production, in association with two hard jets. Given that event selections based on tight cuts on kinematic variables may distort the resulting di-boson invariant mass spectrum, creating artificial peaks also in backgrounds, we need additional handles to adequately describe the final invariant mass distribution. Alternatively, when the smooth di-boson invariant mass shape is preserved with selection on angular information, we still need to control this shape for proper background estimate using either a sideband approach or a fit procedure. Therefore, we define a control sample with which we can probe directly the same variable phase space defined by the analysis selection.

The control sample is provided by γ+jets events, which have a yield about 10-20 times higher than Z+jets. In the massless approximation, i.e. when the energy scale of the interaction is such that the mass difference between the electromagnetic and the weak boson can be neglected, the two processes should have similar kinematics. Photons, furthermore, are precisely measured in the electromagnetic calorimeter, just as a leptonically decaying Z boson, therefore we expect a similar a similar behavior in the final di-boson (V+jets) invariant mass spectrum.

In order to select γ+jet events, a stringent photon identification is needed, which will substitute the lepton identification used in the case of the leptonically decaying Z boson. The photon ID we use is taken from [25] and makes use of isolation criteria in the tracker, ECAL and HCAL, plus cluster shape criteria that select ECAL energy deposits which are compatible with the photon hypothesis.

The photon identification criteria are summarized as followed:

- **tracker isolation**: the scalar sum of the transverse momenta of all tracks reconstructed in $\Delta R < 0.35$ around the photon direction must be less than 10% of the photon transverse momentum, and no more than three tracks must be found in that cone;

- **ECAL isolation**: the sum of all ECAL energy deposits found in a cone of $\Delta R = 0.4$ around the photon candidate direction, excluding the rechits belonging to the photon super cluster seed must not exceed 5% of the photon energy or 3 GeV;

- **HCAL isolation**: the sum of all energy deposits in HCAL cells found in a cone of $\Delta R = 0.4$ around the photon candidate direction must not exceed 5% of the photon energy or 2.4 GeV;

- **cluster shapes**: the second moments of the photon basic cluster, computed with respect to the principal axes, are required to be less than 0.3 and 0.35, respectively for the minor and major axes. The cluster minor is further required to be greater than 0.15 in order to suppress calorimetric noise.

The photon candidate is further required to be contained in the central part of the ECAL barrel ($|\eta| < 1.3$).

In order to take into account the effect of the preselection requirements on the boson kinematics, a simple two body decay simulation has been implemented. Firstly, a mass equal to the Z boson mass is granted to the photon. This is done by adding energy to the photon quadrimomentum until its mass is sufficiently large. The mass is generated randomly from a relativistic Breit-Wigner distribution, with mass and width parameters set to the PDG average [19]. The distribution of the photon corrected mass is compared to the reconstructed di-lepton invariant mass in Z+jet events in Figure 80. As can be seen there are visible discrepancies in the tails, which originate from resolution effects which are not taken into account in this simulation. This could be further improved.

Secondly, the mass-corrected photon is forced to 'decay' into two massless pseudoleptons[1]. This is done through a simple simulation. The photon is assumed to have no spin polarization, so the decay is assumed to follow flat angular probability density functions in the boson restframe. The generated pseudoleptons are then boosted to the laboratory frame, and the preselection cuts ($p_T > 40/20$ GeV and $|\eta| < 2.4$) are applied to their boosted quadrimomenta. Figures 81 compares the transverse momentum of leptons in Z+jet events with those of the pseudoleptons generated in this simulated decay. A sufficient level of agreement is found, yet the spectrum of the leading lepton seems significantly harder in Z+jet events.

Once the four objects in the event are defined (two jets and the two pseudoleptons), we can compute the ZZ invariant mass also in γ+jet events, and compare to what is obtained in Z+jet events. This is shown in Fig. 82, for the three b-tag categories. A good level of agreement between the two datasets is observed, which can be regarded

---

[1] An advantage of this method is that, if the decay is correctly simulated, a pseudo-angular likelihood discriminant can in principle be computed also in γ+jet events, therefore the full analysis chain can be applied.
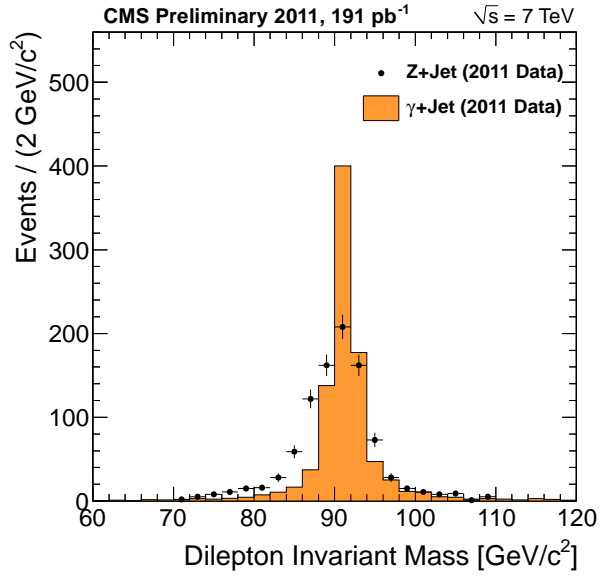
75

Figure 80: Comparison between Z+jets and photon+jets events: the reconstructed di-lepton invariant mass in Z+jet events is compared to the simulated invariant mass assigned to photons in γ+jet events. The γ+jets distribution is normalized to the Z+jets integral.
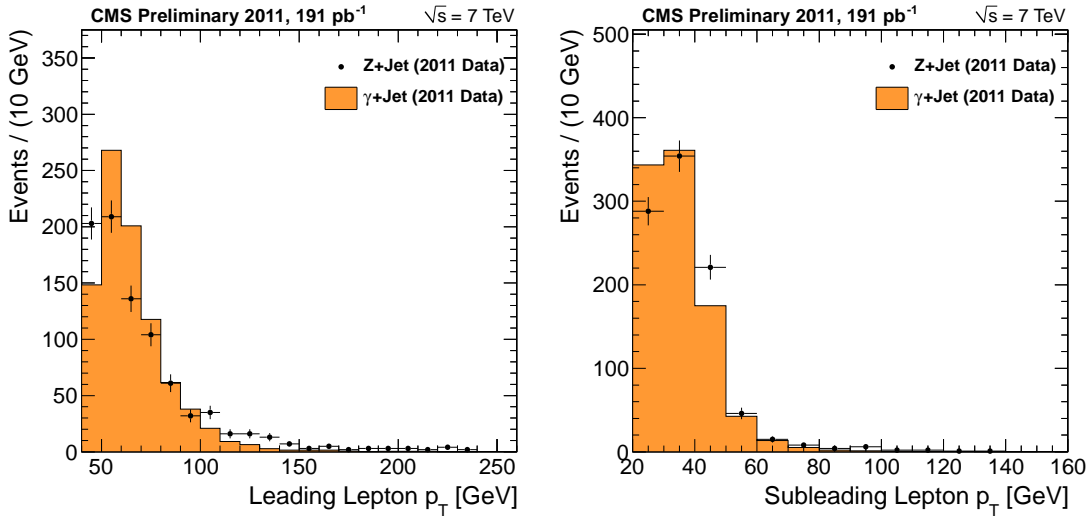

Figure 81: Comparison between Z+jets and photon+jets events: the trasverse momenta of the leading (left) and subleading (right) reconstructed leptons in Z+jet events are compared to the transverse momenta of pseudoleptons coming from the simulated boson decay in γ+jet events. The γ+jets distributions are normalized to the Z+jets integral.

as a small *a posteriori* validation of the procedure. The resulting available statistics, is more than 10 times larger in the 0-btag category, five times larger in the 1-btag category, but (unexpectedly) of the same order of magnitude in the 2-btag category. It must be noted that the ZZ invariant mass spectrum in the 0-btag category seems slightly, yet significantly, harder in Z+jet events compared to γ+jet events. This is under further investigation.
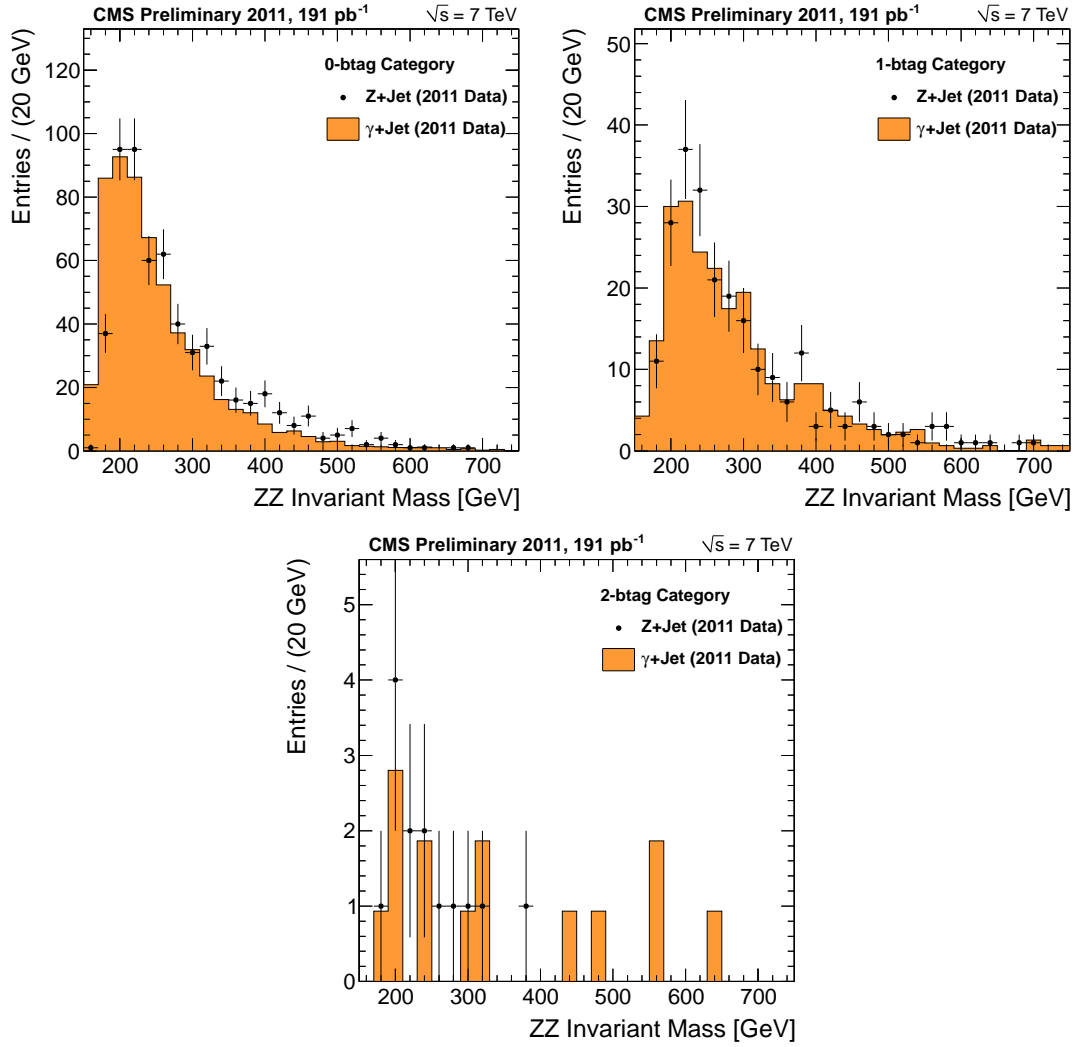
Figure 82: Comparison between Z+jets and photon+jets events with 2011 data: boson+dijet invariant mass spectra in the 0-btag (left), 1-btag (right) and 2-btag (bottom) categories. The γ+jets distributions are normalized to the Z+jets integral.

References

[1] The LEP Electroweak Working Group and the Tevatron Electroweak Working Group, http://lepewwg.web.cern.ch/LEPEWWG/

[2] A. Bonato, A.V. Gritsan, Z.J. Guo, N.V. Tran, A. Whitbeck, "Angular Analysis of Resonances $pp \rightarrow X \rightarrow ZZ$," CMS-AN-2010-351.

[3] CMS Collaboration Higgs Review Workshop, December 2010, https://indico.cern.ch/conferenceDisplay.py?confId=114679.

[4] S. Bolognesi *et al.*, "Search for a SM Higgs or BSM Boson $H \rightarrow ZZ \rightarrow 2\ell 2q$," CMS-AN-2011-100.

[5] L. Borrello *et al.*, "Search for the Standard Model Higgs Boson in the Decay Channel $H \rightarrow ZZ \rightarrow 2l2b$," CMS-AN-2011-399.

[6] For generator documentation, see documentation at http://www.pha.jhu.edu/spin/ and Ref. [7].

[7] Y.Y. Gao *et al.*, "Spin determination of single-produced resonances at hadron colliders," Phys. Rev. D **81**, 075022 (2010).

[8] A. De Rujula, J. Lykken, M. Pierini, C. Rogan and M. Spiropulu, "Higgs look-alikes at the LHC," Phys. Rev. D **82** (2010) 013003 [arXiv:1001.5300 [hep-ph]].

[9] Pythia generator package, http://home.thep.lu.se/~torbjorn/Pythia.html.

[10] "Physics Analysis Toolkit (PAT)," https://twiki.cern.ch/twiki/bin/view/CMS/SWGuidePAT.

[11] CMS Collaboration, "Electron reconstruction and identification at $\sqrt{s}$=7 TeV", CMS Physics Analysis Summary EGM-10-004.

[12] CMS Collaboration, "Performance of muon identification in pp collisions at $\sqrt{s}$=7 TeV", CMS Physics Analysis Summary MUO-10-002.

[13] CMS Collaboration, "Jet Performance in pp Collisions at $\sqrt{s}$=7 TeV", CMS Physics Analysis Summary JME-10-003.

[14] CMS Collaboration, "Commissioning of the Particle-Flow Reconstruction in Minimum-Bias and Jet Events from pp Collisions at 7 TeV", CMS Physics Analysis Summary PFT-10-002.

[15] The CMS Collaboration, "Trigger strategies for Higgs searches in 2011," CMS-AN-2011/065.

[16] For Vector Boson Task Force (VBTF) prescriptions, see https://twiki.cern.ch/twiki/bin/view/CMS/SimpleCutBasedEleID#Isolations_Calculation, https://twiki.cern.ch/twiki/bin/viewauth/CMS/VbtfEleID2011, and https://twiki.cern.ch/twiki/bin/view/CMS/ConversionBackgroundRejection.

[17] M. Cacciari, G. P. Salam,, G. Soyez, "The anti-kt jet clustering algorithm" JHEP 0804 (2008) 063 [arXiv:0802.1189].

[18] CMS Collaboration, "Jet Energy Corrections determination at 7 TeV" CMS-PAS-JME-10-010.

[19] Particle Data Group, "Review of particle physics," J. Phys. G **37**, 075021 (2010).

[20] N. Amapane et al., "Search for a Standard Model Higgs boson produced in the decay channel $H \rightarrow ZZ^{(*)} \rightarrow 4l$", CMS-AN-2011/123.

[21] J. Bochenec et al., "Search for a Standard Model Higgs boson using the $H \rightarrow ZZ \rightarrow 2l2\nu$ decay mode in pp-collisions at $\sqrt{(s)}$=7 TeV", CMS-AN-2011/119.

[22] CMS Collaboration, "Commissioning of b-jet identification with pp collisions at $\sqrt{s} = 7$ TeV," CMS-PAS-BTV-10-001.

[23] A. Marini, F. Pandolfi, D. del Re, M. Voutilainen, "Quark-Gluon Jet Discrimination through Particle Flow Jet Structure," CMS AN-2011/215.

78

[24] Toolkit for Multivariate Data Analysis with ROOT, http://tmva.sourceforge.net/.

[25] F. Pandolfi, D. del Re, M. Voutilainen, "Jet Response and Resolution Measurement with Photon+Jet Events Recorded in 2010 at $\sqrt{s} = 7$ TeV," CMS-AN-2011/002.

[26] M. Voutilainen *et al.*, "Absolute jet energy correction uncertainty," CMS-AN-2010/304.

[27] CMS Collaboration, "Jet Energy Resolution in CMS at $\sqrt{s} = 7$ TeV," CMS-PAS-JME-10-014.

[28] Missing ET Uncertainty Prescription, https://twiki.cern.ch/twiki/bin/viewauth/CMS/MissingETUncertaintyPrescription.

[29] H. L. Lai, M. Guzzi, J. Huston, Z. Li, P. M. Nadolsky, J. Pumplin and C. P. Yuan, "New parton distributions for collider physics," Phys. Rev. D **82** (2010) 074024 [arXiv:1007.2241 [hep-ph]].

[30] A. D. Martin, W. J. Stirling, R. S. Thorne and G. Watt, "Parton distributions for the LHC," Eur. Phys. J. C **63** (2009) 189 [arXiv:0901.0002 [hep-ph]].

[31] R. D. Ball *et al.*, "Impact of Heavy Quark Masses on Parton Distributions and LHC Phenomenology," Nucl. Phys. B **849** (2011) 296 [arXiv:1101.1300 [hep-ph]].

[32] T. Gleisberg *et al.*, "Event generation with Sherpa 1.1," JHEP 0902 (2009) 007 [arXiv:0811.4622 [hep-ph]].

[33] The CMS Collaboration, "Trigger strategies for Higgs searches in 2011," CMS-AN-2011/065.

[34] CMS collaboration, "CMS Higgs Combination," CMS-HIG-11-032.

[35] A. L. Read "Presentation of search results: the CLs technique," J. Phys. G: Nucl. Part. Phys. 28, 2693 (2002).

[36] A. O'Hagan and J.J. Forster, "Bayesian Inference", Kendall's Advanced Theory of Statistics, Arnold, London, volume 2B (2004).

[37] L .Moneta, K. Belasco, K. Cranmer, A. Lazzaro, D. Piparo *et al.*, "The RooStats Project", PoS, ACAT2010, 057 (2010), arxiv:1009.1003.

[38] M. Chen and A. Korytov, "Limits and Signifcance", https://mschen.web.cern.ch/mschen/LandS/

[39] V. Barger *et al.*, "Higgs bosons: Intermediate mass range at e+e- colliders," Phys. Rev D. 49, 79 (1994).